UNIVERSITY OF CALIFORNIA
RIVERSIDE

Material Genomics for Device Applications: Atoms to High-Throughput Ab-Initio Calculations

A Dissertation submitted in partial satisfaction
of the requirements for the degree of

Doctor of Philosophy

in

Electrical Engineering

by

Protik Das

December 2018

Dissertation Committee:

Dr. Roger K. Lake, Chairperson
Dr. Alexander Balandin
Dr. Jianlin Liu

The Dissertation of Protik Das is approved:

Committee Chairperson

University of California, Riverside

Acknowledgments

First I thank my advisor, Professor Roger K. Lake for accepting me as a student, and guiding me during my research. Without his unparalleled patience with me, I would not be here. I also acknowledge support from Prof. Jianlin Liu, and Dr. Peng Wei for allowing me to collaborate with their respective groups, valuable discussions and feedback during the collaborative projects. I would also like to thank Prof. Alexander Balandin for his time and feedback as a member of the committee.

I specially thank Dr. Darshana Wickramaratne, and Dr. Mahesh Neupane, past members of our lab, for making me feel welcome as soon as I joined the lab. Our weekly group therapy sessions later on were crucial for my survival. I would also like to thank Dr. Gen Yin, and Dr. Shanshan Su, for continuing the trend of collaborative projects within the lab members. I also acknowledge current members of the lab for their continuing support and help throughout my journey. I thank Dr. Alireza Khanaki, Mr. Hao Tian, Mr. Yanwei He, members of Liu group UCR, for their patience for the theoretical calculations during our collaborative projects. A special thanks to Dr. Timur Bazhirov, CEO of Exabyte Inc. for support and training as an intern.

On the personal side I would like to acknowledge my friends and family for their continuous support over the past few years. I am thankful to my parents for their guidance and support of my education. Last but not least, I would like to thank my wife, Peea Purkayastha, who had to endure the most during my PhD.

The text of this dissertation, in part or in full, is a reprint of the material as it appears in the following journal:

- Nano Letters [159] [2018]. American Chemical Society

This work was supported by FAME, one of six centers of STARnet, a Semiconductor Research Corporation program sponsored by MARCO and DARPA, and also by the NSF (1433395) EFRI 2-DARE: Novel Switching Phenomena in Atomic Heterostructures for Multifunctional Applications. This work used the Extreme Science and Engineering Discovery Environment (XSEDE), which is supported by National Science Foundation Grant No. ACI-1548562 and allocation ID TG-DMR130081. The work presented in Chapter 4 of this thesis was supported by Exabyte Inc., and the computational resources were provided by Microsoft Azure.

To my mom.

ABSTRACT OF THE DISSERTATION

Material Genomics for Device Applications: Atoms to High-Throughput Ab-Initio Calculations

by

Protik Das

Doctor of Philosophy, Graduate Program in Electrical Engineering
University of California, Riverside, December 2018
Dr. Roger K. Lake, Chairperson

The singular density of states and the two Fermi wavevectors resulting from a ring-shaped or "Mexican hat" valence band give rise to unique trends in the charged impurity scattering rates and charged impurity limited mobilities. Ring shaped valence bands are common features of many monolayer and few-layer two-dimensional materials including the III-VI materials GaS, GaSe, InS, and InSe. The wavevector dependence of the screening, calculated within the random phase approximation, is so strong that it is the dominant factor determining the overall trends of the scattering rates and mobilities with respect to temperature and hole density. Charged impurities placed on the substrate and in the 2D channel are considered. The different wavevector dependencies of the bare Coulomb potentials alter the temperature dependence of the mobilities. Moving the charged impurities 5 Å from the center of the channel to the substrate increases the mobility by an order of magnitude by suppressing the large wavevector backscattering within the outer Fermi ring.

Using first-principles calculations, we investigate the cobalt (111) surface as an alternative substrate for the growth of hexagonal boron nitride (h-BN). We find the adsorp-

tion energies of B and N to be larger on the Co(111) surface compared to the commonly used Cu(111) surface. Trace concentrations of carbon within the Co(111) substrate are found to lower the adsorption energies of B and N on Co(111). The most favorable binding sites and the migration barriers between these sites are also elucidated using nudged elastic band calculations.

Despite multiple successful applications of high-throughput computational materials design from first principles, there are a number of factors that inhibit its future adoption. Of particular importance are the limited ability to provide high fidelity in a reliable manner and the limited accessibility to non-expert users. We present example applications of a novel approach, where high-fidelity first-principles simulation techniques, density functional theory with hybrid screened exchange (HSE) and the GW approximation, are standardized and made available online in an accessible and repeatable setting. We apply this approach to extract electronic band gaps and band structures for a diverse set of 847 materials ranging from pure elements to III-V and II-VI compounds, ternary oxides and alloys. We find that for HSE and G_0W_0, the average relative error fits within 20%, whereas for conventional generalized gradient approximation the error is 55%. For HSE we find the average calculation time on an up-to-date server centrally available from a public cloud provider fits within a 48 hours window. This work provides a cost-effective, accessible and repeatable practical recipe for performing high-fidelity first-principles calculations of electronic materials in a high-throughput manner.

Contents

List of Figures

List of Tables

Chapter 1

Rationale

1.1 Introduction

Since the advent of the integrated circuit, the semiconductor industry has been driven by the exponential down-scaling of the silicon transistor. This exponential shrinking of the transistor with time, known as Moore's law, has continued for 50 years, and it is now reaching its physical limits. Down-scaling of silicon below the 10 nm technology node has yet to be achieved. Hence, there is a continuous search for materials and material classes that can replace or supplement silicon. One of the new material classes are the layered two-dimensional (2D) materials. This class of materials can be thinned down to one atomic layer. A field effect transistor (FET) built using one atomic layer of material has the potential for considerable improvement in power density and scaling. Also, new materials may enable new types of transistors and devices that are not subject to the same fundamental limitations as the traditional FET. A good understanding of the new material

growth, material properties, and transport properties is needed before this class of materials can be considered as a replacement of or supplement to silicon based technology.

Due to improvements in high performance computing, machine learning is being applied to many different fields. In the field of material science it is being applied to find materials with desired properties. While machine learning in fields like image processing is considered trivial because of the availability of image data, machine learning in material science is non-trivial. This is due to the fact that even though there are a huge number of publications available related to material science, the data is not in a tabulated or structured format which is a requirement for machine learning. Not only that, the material properties resulting from a computation may depend strongly on the level of theory used for the computation. The canonical example is the bandgap, which can have a strong dependence on the level of theory used in a density functional theory calculation. Hence it is quite difficult to tabulate the existing data from the literature for the application of machine learning. While some effort has been given to collect and tabulate the existing data [2], another alternative is to produce new data using high throughput computing. Within high-throughput computing, a common framework is needed so that calculations on a large number of materials can be done with minimal effort. In this process, all the input parameters must to be stored in a database for future use.

1.1.1 Objective

The two-dimensional (2D) metal monochalcogenides are relatively new members of the 2D family. The majority of the semiconducting materials are semiconducting in their bulk form and remain semiconducting when thinned down to one monolayer. Along with non

zero band gap in their monolayer, some of the materials have a ring shaped valance band. This ring shaped band results in a singular density of states (DOS) at their band edges. The effect of this singular DOS on the screening and ionized impurity scattering has not yet been investigated. Hence, I provide a detailed analysis of ionized impurity scattering and ionized impurity limited mobility with wavevector dependent screening calculated within a random phase approximation.

Another member of the 2D family is hexagonal boron nitride (h-BN). Due it's large band gap ($\sim$ 6 eV) it is considered as an alternative oxide layer for FETs. Even though growth of h-BN is explored using chemical vapor deposition (CVD) method, controlled growth of monolayer h-BN in an MBE chamber is yet to be achieved. For this project, I will be using density functional theory calculations to identify mechanisms that aid in the initial nucleation of monolayer h-BN growth.

The starting point for applying machine learning in material science is to do high-throughput computing. One way this can be achieved is to do high-throughput calculations using ab-initio density functional theory (DFT). Performing DFT calculations for any material requires careful consideration of the physics of the material. When applying to a large set of materials, an appropriate framework must be designed. For this project I design workflows that enable high-throughput band structure and band gap calculations using density functional theory.

1.2 Organization

The rest of the dissertation is organized as follows. Chapter 2 presents the theoretical methods and models to calculate and understand charged impurity scattering in 2D materials with ring shaped valance bands. Chapter 3 presents density functional theory calculations exploring nucleation conditions to achieve controlled growth of monolayer h-BN. The chapter also explores intercaleted growth of thin h-BN. Chapter 4 presents a framework for employing high-throughput calculations using density functional theory along with band gap calculations done in a high-throughput manner for 775 materials. Descriptions of useful scripts and code are provided in the appendices along with a basic description of administrative tasks related to the labs computational cluster.

Chapter 2

Charged impurity scattering in two-dimensional materials with ring-shaped valence bands: GaS, GaSe, InS, and InSe

2.1 Introduction

Atomically thin two-dimensional (2D) materials are being investigated for a range of applications including emerging beyond-CMOS electronic devices, thermoelectrics, and optoelectronics. A number of these materials have "ring shaped" valence bands. These materials include the semiconducting III-VI monochalcogenides, GaS, GaSe, InS, and InSe [176, 189, 188, 65, 186, 30, 178, 53], bilayer graphene when subject to a vertical electric field

[154, 167, 118], monolayers of Bi_2Se_3[176] and Bi_2Te_3[183, 111, 140], few-layers of Bi_2Se_3 intercalated with 3d transition metals[107], monolayer SnO[143, 63], 2D hexagonal lattices of group-VA elements [144], and hexagonal group-V binary compounds[123].

A ring shaped valence band results in a $1/\sqrt{E}$ singularity in the 2D density of states and a step function turn on of the density of modes at the valence band edge [111, 176, 102, 103, 113]. At low temperatures, density functional theory calculations show that the singularity in the density of states leads to a ferromagnetic phase transition at sufficient hole doping [30, 178]. More recent calculations find that such a transition is a general property of the Mexican hat dispersion [143].

The ring shaped dispersion affects ionized impurity scattering through the density of states, the momentum transfer required to scatter around the ring, and the momentum dependence of the screening. The question we address is what is the influence of the "ring-shaped" dispersion on the temperature, density, and Fermi energy dependence of the ionized impurity scattering rates and ionized impurity limited mobility.

Prior studies have theoretically investigated the role of ionized impurity scattering in two–dimensional materials with a parabolic dispersion. Ionized impurity scattering can severely limit the mobility in the transition metal dichalcogenides such as MoS_2 [110] and give rise to an unexpected temperature dependence of the mobility [126]. It has been predicted that reducing the doping can enhance the linear screening response within the Thomas-Fermi theory [91]. The role of screening on charged impurity scattering and charged impurity limited moblility in materials with a ring-shaped dispersion has not yet been addressed.

We address this question using an analytical bandstructure model with parameters extracted from first principles calculation. Screening is included within the random phase approximation. Polarization functions and scattering rates are analyzed, and the ionized impurity limited hole mobility of the III-VI materials, GaS, GaSe, InS, and InSe, are compared.

2.2 Theory

The materials and geometry of the problem consist of a monolayer 2D semiconducting material on a insulating substrate encapsulated by an insulating capping layer which could be the same as the substrate. Example insulating materials are BN or SiO_2. The structure is illustrated in Fig. 2.1 with SiO_2 for the substrate and BN for the capping layer. A cylindrical coordinate system is used with $\mathbf{r}$ a vector in the x–y plane. The origin is at the center of the semiconductor. Charged impurities will be considered for two different positions, in the center of the 2D semiconductor, $z = 0$, and on the surface of the substrate, $z = -d$. Accounting for the 5 Å thickness of a monolayer III-VI semiconductor and the 3 Å van der Waals gap,[176] we use $d = 5.5$ Å for the charged impurities on the surface of the substrate. The value of the impurity density used in all calculations is 10^{12} cm^{-2}. All calculated scattering rates are linearly proportional to the impurity density, and all mobilities are inversely proportional to the impurity density, so any calculated values can be scaled for different impurity densities.

The investigation of the effect of the Mexican hat dispersion on screening, scatter-

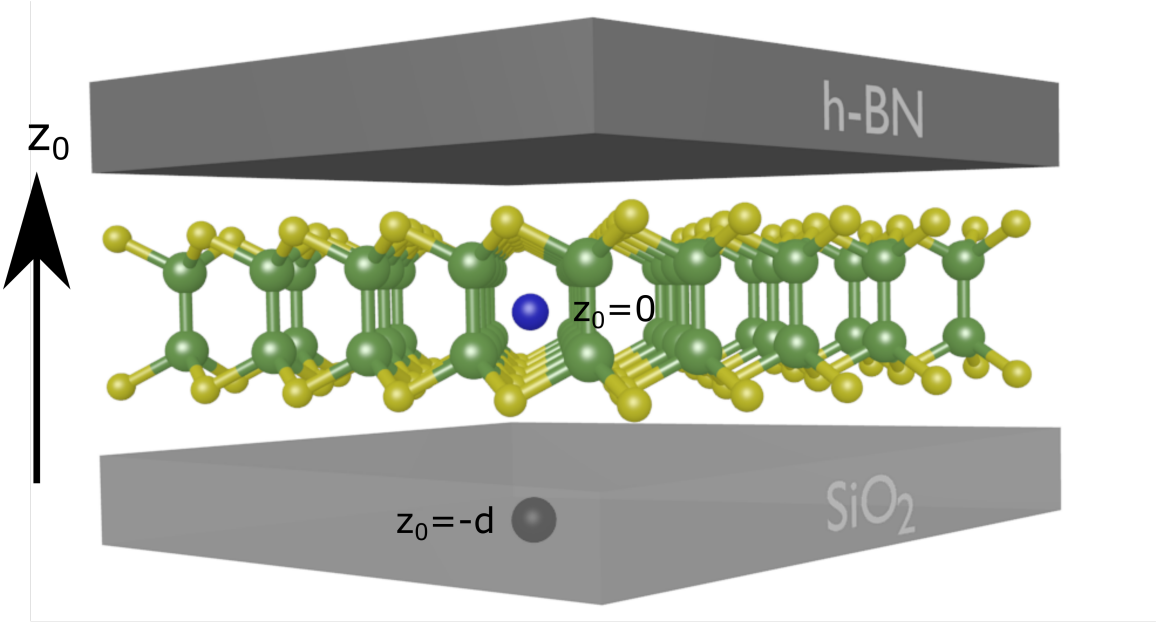

Figure 2.1: Monolayer GaS between SiO_2 substrate and BN capping layer. The black atom depicts an ionized impurity inside the capping layer 5.5Å from the channel. And the blue atom depicts a ionized impurity inside the monolayer GaS.

ing, and mobility, begins with the model quartic dispersion

$$E(k) = \epsilon_h - \frac{\hbar^2 k^2}{2m^*} + \frac{1}{4\epsilon_h}\left(\frac{\hbar^2 k^2}{2m^*}\right)^2. \tag{2.1}$$

Quartic models have been previously used to investigate interactions in biased bilayer graphene [154], multiferroic 2D materials [143], and electronic and thermoelectric properties of group III-VI and group VA 2D materials [176, 144]. We define our momentum-energy relation such that the hole kinetic energy is positive, the valence band edge is at $E = 0$, and negative energies correspond to energies in the band gap. The term ϵ_h in Eq. (2.1) is the height of the 'hat' at $k = 0$ and m^* is the magnitude of the effective mass at $k = 0$ (the top of the hat). The addition of the constant term ϵ_h in Eq. (2.1), shifts the dispersion so that the minimum energy, corresponding to the band edge, occurs at $E = 0$. For energies $0 < E < \epsilon_h$ the Mexican hat dispersion has two Fermi wave–vectors corresponding to the two branches

of the dispersion. In this energy region, the Fermi surface consists of two concentric circles shown in Fig. 2.2(a). The radii of the two circles are $k_1 = \frac{\sqrt{2m^*\epsilon_h}}{\hbar}\sqrt{1-\sqrt{E/\epsilon_h}}$ and $k_2 = \frac{\sqrt{2m^*\epsilon_h}}{\hbar}\sqrt{1+\sqrt{E/\epsilon_h}}$. At the band edge, $E = 0$, the two circles merge into a single circle with a radius of $k_0 = 2\sqrt{m^*\epsilon_h}/\hbar$. The effective mass at the band edge determined from $\frac{1}{m^*(k_0)} = \frac{\partial^2 E}{\hbar^2 \partial k^2}\Big|_{k=k_0}$ is $m^*/2$. The single–spin densities of states for each individual k-space ring are identical and equal to

$$D_1(E) = D_2(E) = \frac{m^*}{2\pi\hbar^2}\sqrt{\frac{\epsilon_h}{E}} \qquad (0 \le E \le \epsilon_h) \tag{2.2}$$

The total single-spin density of states is given by the sum and is equal to

$$D(E) = \begin{cases} \frac{m^*}{\pi\hbar^2}\sqrt{\frac{\epsilon_h}{E}} & (0 \le E \le \epsilon_h) \\ \frac{m^*}{2\pi\hbar^2}\sqrt{\frac{\epsilon_h}{E}} & (\epsilon_h < E)\ . \end{cases} \tag{2.3}$$

The density of states is plotted in Fig. 2.2(b) using $m^* = 0.409$ m$_0$ and $\epsilon_h = 0.11$ eV, which are similar to the values for monolayer GaS [176]. The density of states diverges as $1/\sqrt{E}$ at the band edge, and it is equal to the single–spin parabolic density of states, $\frac{m^*}{2\pi\hbar^2}$, at the top of the hat.

A parabolic dispersion $E(k) = \frac{\hbar^2 k^2}{2m^*}$ will be used as a reference and for comparison. The parabolic and Mexican hat dispersions and density of states are plotted together in Fig. 2.2. An effective mass of $m^* = 0.409 m_0$ is used for both dispersions.

The two–dimensional Fourier transform of the bare Coulomb potential for a point charge at position $x = y = 0$, $z = z_0$ is

$$v(q) = \frac{e^2 e^{-q|z-z_0|}}{2\epsilon q} \tag{2.4}$$

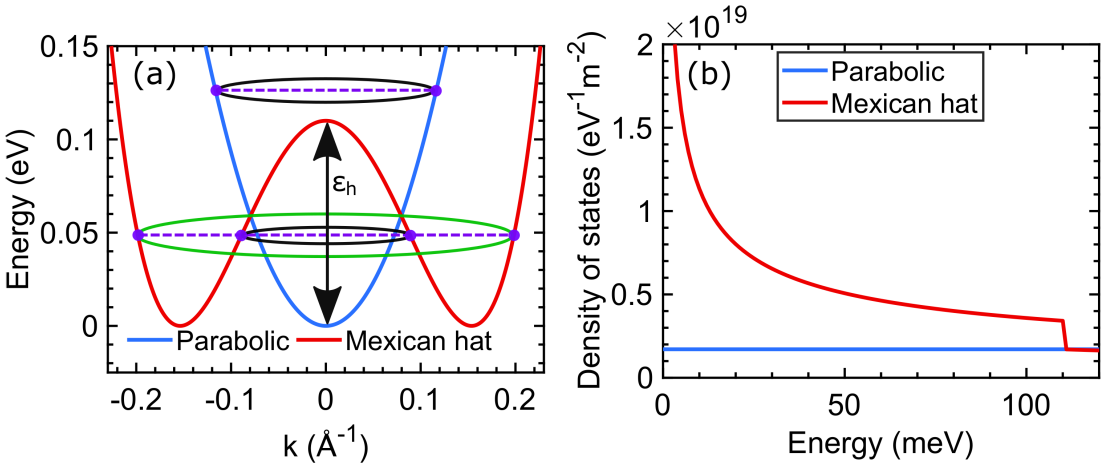

Figure 2.2: (a) Comparison of a paraoblic (blue) and Mexican hat dispersion (blue). The height of the Mexican hat band at $k = 0$ is $\epsilon_h = 0.11$ eV. (b) Density of states of the parabolic band (blue) and Mexican hat dispersion (red). The parabolic and Mexican hat dispersion both have an effective mass of 0.409 m_0.

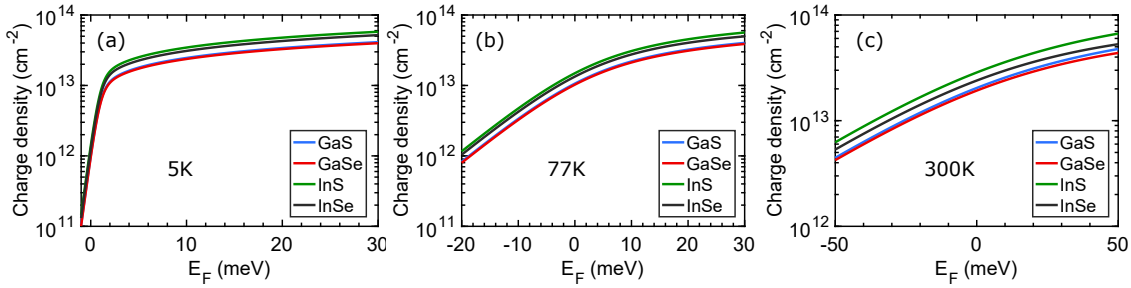

Figure 2.3: Carrier concentration of GaS, GaSe, InS and InSe as a function of Fermi level E_F for (a) 5 K, (b) 77 K and (c) 300 K. Parameters used for materials are tabulated in Table 2.1.

where e is the charge of electron, ϵ is the average static dielectric constant and q is the momentum transfer. Since all of the III-VI materials have relative dielectric constants in the range of $3-4$, we will use the dielectric constant of the semiconductor. Within the random phase approximation, the screened Coulomb potential is

$$V(q,z) = \frac{v(q)}{1-\Pi(q)v(q)}. \tag{2.5}$$

Substituting Eq. (2.4) into Eq. (2.5) gives the 2D RPA screened potential,

$$\begin{aligned} V(q) &= \frac{e^2}{2\epsilon(qe^{q|z-z_0|} - \frac{e^2}{2\epsilon}\Pi(q))} \\ &= \frac{e^2}{2\epsilon(qe^{q|z-z_0|} + q_\lambda(q))} \end{aligned} \tag{2.6}$$

where $q_\lambda(q) \equiv -\frac{e^2}{2\epsilon}\Pi(q)$ is the wavevector dependent inverse screening length. In the static limit, the polarization function is [114]

$$\Pi(q) = \frac{2}{A}\sum_{\mathbf{k}} \frac{f(E_{\mathbf{k}+\mathbf{q}}) - f(E_{\mathbf{k}})}{E_{\mathbf{k}+\mathbf{q}} - E_{\mathbf{k}}} \tag{2.7}$$

where A is the area, $E_{\mathbf{k}}$ is the eigenenergy at wavevector $\mathbf{k}$, and $f(E)$ is the Fermi-Dirac function. The factor of 2 is for spin degeneracy, since the Mexican hat bands in the III-VI materials are spin degenerate. For both the Mexican hat and parabolic dispersions, $E_{\mathbf{k}}$ is only a function of the magnitude of k. Therefore, we define the variable,

$$k_+ = |\mathbf{k}+\mathbf{q}| = \sqrt{k^2+q^2+2kq\cos\theta}, \tag{2.8}$$

and calculate the polarization from Eq. 2.7,

$$\Pi(q) = \frac{1}{2\pi^2}\int_0^\infty dk k \int_0^{2\pi} d\theta \frac{f(E(k_+)) - f(E(k))}{E(k_+) - E(k)}. \tag{2.9}$$

In the limit $\mathbf{q} \to 0$, the polarization function becomes the negative of the thermally averaged density of states at the Fermi level,

$$\Pi(q=0) = \int_0^\infty dE D(E) \frac{\partial f}{\partial E}, \tag{2.10}$$

where $D(E)$ is the density of states. Using the $\mathbf{q} \to 0$ limit for $\Pi(\mathbf{q})$ in Eq. (2.6), gives the Thomas-Fermi form of the 2D screened Coulomb potential with an inverse screening length of $\frac{e^2}{2\epsilon} D(E_F)$. For the Mexican hat dispersion this is problematic, since the density of states diverges near the band edge. Note that in defining the polarization function in Eq. (2.7), $\Pi < 0$.

To calculate the momentum relaxation time, we need the matrix elements of the RPA Coulomb potential. We assume separable wavefunctions of the form $\langle \mathbf{r}|\mathbf{k}\rangle = \frac{1}{\sqrt{A}} e^{i\mathbf{k}\cdot\mathbf{r}} \sqrt{\delta(z)}$ and take the matrix elements of $\tilde{V}(\mathbf{r}) = \int \frac{d^2q}{4\pi^2} V(q) e^{i\mathbf{q}\cdot\mathbf{r}}$ to obtain $\langle \mathbf{k}|\tilde{V}|\mathbf{k}'\rangle \equiv V_{\mathbf{k},\mathbf{k}'} = \frac{1}{A} V(|\mathbf{k}-\mathbf{k}'|)$. The Fermi's golden rule expression for the inverse momentum relaxation time is given by

$$\frac{1}{\tau(k)} = \frac{N_I 2\pi}{\hbar} \sum_{\mathbf{k}'} |V_{\mathbf{k}',\mathbf{k}}|^2 \delta(E_{\mathbf{k}'} - E_{\mathbf{k}}) \left(1 - \frac{\mathbf{v}(\mathbf{k}) \cdot \mathbf{v}(\mathbf{k}')}{|\mathbf{v}(\mathbf{k})|^2}\right) \tag{2.11}$$

where N_I is the number of charged impurities. For the Mexican hat dispersion, the group velocity $\mathbf{v}$ is opposite to the direction of $\mathbf{k}$ on the inner ring and parallel to $\mathbf{k}$ on the outer ring. On a given branch of the Mexican hat dispersion, $E(\mathbf{k})$ is only a function of the magnitude of $\mathbf{k}$. Therefore, by converting the sum over $\mathbf{k}'$ into an integral and explicitly keeping track of the two branches of the dispersion, Eq. (2.11) becomes

$$\frac{1}{\tau(k)} = \frac{n_I e^4}{4\epsilon^2 \hbar} \sum_{\nu=1}^{2} D_\nu(E) \int_0^{2\pi} d\theta \, \frac{\left(1 - \frac{\mathbf{v}(\mathbf{k}'_\nu)\cdot\mathbf{v}(\mathbf{k})}{v^2(k)}\right)}{\left(q\, e^{qz_0} + q_\lambda(q)\right)^2} \tag{2.12}$$

where the sum is over the two Fermi rings, $q = |\mathbf{k}'_\nu - \mathbf{k}| = \sqrt{{k'_\nu}^2 + k^2 - 2k'_\nu k\cos\theta}$, k and k'_ν correspond to the radii of the concentric iso-energy rings in Fig. 2.2, $D_\nu(E)$ is the final single–spin density of states corresponding to ring ν, $\mathbf{v}(\mathbf{k}'_\nu)$ is the final group velocity of ring ν, and n_I is the impurity density per unit area. The value of z_0 is either zero for impurities placed at the center of the semiconducting monolayer or 5.5 Å for impurities placed on the substrate.

The last term on the right of Eq. (2.11) is $1 - \frac{v'}{v}\cos(\theta_{\mathbf{v},\mathbf{v}'})$ where $\theta_{\mathbf{v},\mathbf{v}'}$ is the angle between the group velocity of state $\mathbf{k}$ and the group velocity of state $\mathbf{k}'$. This term is the relative change in the component of the velocity that is parallel to the initial velocity v. When the final velocity v' is in the same direction and greater than the initial velocity v, then scattering from v to v' causes the carrier to speed up and gives a negative contribution to the momentum relaxation time [8]. This situation occurs for carriers that are initially near the top of the hat in Fig. 2.2(a) and then scatter to the outer ring. However, the negative values are restricted to a range of angles centered around 180°, and the integral over θ in Eq. (2.12) is always positive.

The carrier mobility is determined from the average group velocity driven by an external electric field oriented in the x–direction. To linear order, this is

$$\langle v_x \rangle = \frac{\sum_{\mathbf{k}} v_x(\mathbf{k}) f_A(\mathbf{k})}{\sum_{\mathbf{k}} f_0(\mathbf{k})} \tag{2.13}$$

where $f_A(\mathbf{k})$ is the asymmetric component of the non-equilibrium distribution function. Within the relaxation time approximation, the asymmetric distribution function can be written as,

$$f_A(\mathbf{k}) = -\tau(k)\frac{e\mathcal{E}_x}{\hbar}\frac{\partial f_0(\mathbf{k})}{\partial k}\cos\theta \tag{2.14}$$

where $f_0(\mathbf{k})$ is the equilibrium Fermi function, $\mathcal{E}_x$ is the electric field along the transport direction and θ is the direction of $\mathbf{k}$ with respect to the k_x axis. The mobility is directly evaluated from its definition, $\mu = \langle v_x \rangle / \mathcal{E}_x$. Substituting (2.14) into (2.13), the final expression for carrier mobility is

$$\mu = -\frac{e}{2\pi\hbar^2 p} \int_0^\infty dk\, k\, \tau(k)\, \frac{\partial f_0}{\partial \epsilon} \left(\frac{\partial \epsilon}{\partial k} \right)^2 \tag{2.15}$$

where the spin–degenerate 2D hole density $p = \frac{2}{A} \sum_{\mathbf{k}} f_0(\mathbf{k})$.

2.3 Results

The polarization function $\Pi(q)$ gives wave–vector dependent screening. In a two dimensional material with parabolic dispersion, the density of states is constant which results in a constant polarization function for $q < 2k_F$ at low temperature. In a Mexican hat dispersion, the singular density of states gives a strong wave–vector dependence to the polarization function at low temperature. It also increases the overall magnitude of the polarization function. The wavevector dependent inverse screening length $q_\lambda(q)$ is added to the momentum transfer q in the denominator of Eq. (2.6), and the sum determines the magnitude and wavevector dependence of the screened Coulomb interaction. Therefore, we begin by analyzing q_λ as a function of q for the Mexican hat dispersion.

To provide a point of reference, we first show in Fig. 2.4(a) the well–known wavevector dependent inverse screening length q_λ resulting from a parabolic dispersion with the Fermi level fixed at 40 meV above the band edge. At low temperature and for wave–vectors smaller than $2k_F$, the magnitude of q_λ is simply $\frac{e^2}{2\epsilon} \frac{m^*}{\pi\hbar^2}$, i.e. $\frac{e^2}{2\epsilon}$ times the density of states at the Fermi level. This is equal to 3.78 $m_r/\epsilon_r = 0.499$ Å^{-1} where $m_r = 0.409$ is the

relative effective mass and $\epsilon_r = 3.1$ is the relative dielectric constant. Since the density of states is constant, the resulting inverse screening length is constant up until the momentum transfer is greater than $2k_F$. At higher temperatures, the polarization function can be written as a convolution of the zero–temperature polarization and a thermal broadening function [114]. The result is that the sharp q-dependent features become smeared out at finite temperatures.

Unlike the parabolic dispersion where scattering occurs within a single Fermi ring, Coulomb scattering in a Mexican hat dispersion occurs within and between two concentric rings for energies up to ϵ_h, which defines the height of the Mexican hat dispersion. Furthermore, the density of states is singular at the band edge. To understand the implications of these features, the inverse screening length is plotted, as a function of the momentum transfer, q, for different values of the Fermi energy in Fig. 2.4(b-c) and for a fixed carrier density in Fig. 2.4(d).

Fig. 2.4(b) shows the inverse screening length of the Mexican hat dispersion at 3 different temperatures with the Fermi level fixed at 5 meV above the bandedge. The low–temperature ($T = 5$ K) curve has a strong q dependence that arises from the bandstructure. There are two Fermi wave–vectors for $0 < E_F < \epsilon_0$ denoted as k_{F_1} and k_{F_2} and illustrated in the inset of Fig. 2.4(c). The two Fermi wave–vectors result in three features for $\Pi(q)$ at $T = 5$ K. These features correspond to momentum transfers of $q = 2k_{F_1}$, $q = 2k_{F_2}$, and $q = k_{F_2} - k_{F_1}$. Just as with the parabolic dispersion, there is a sharp change in the derivative of $\Pi(q)$ when q is twice the Fermi wave–vector, except now there are two Fermi wave–vectors. The third and largest peak occurs when $q = k_{F_2} - k_{F_1}$, which is the minimum

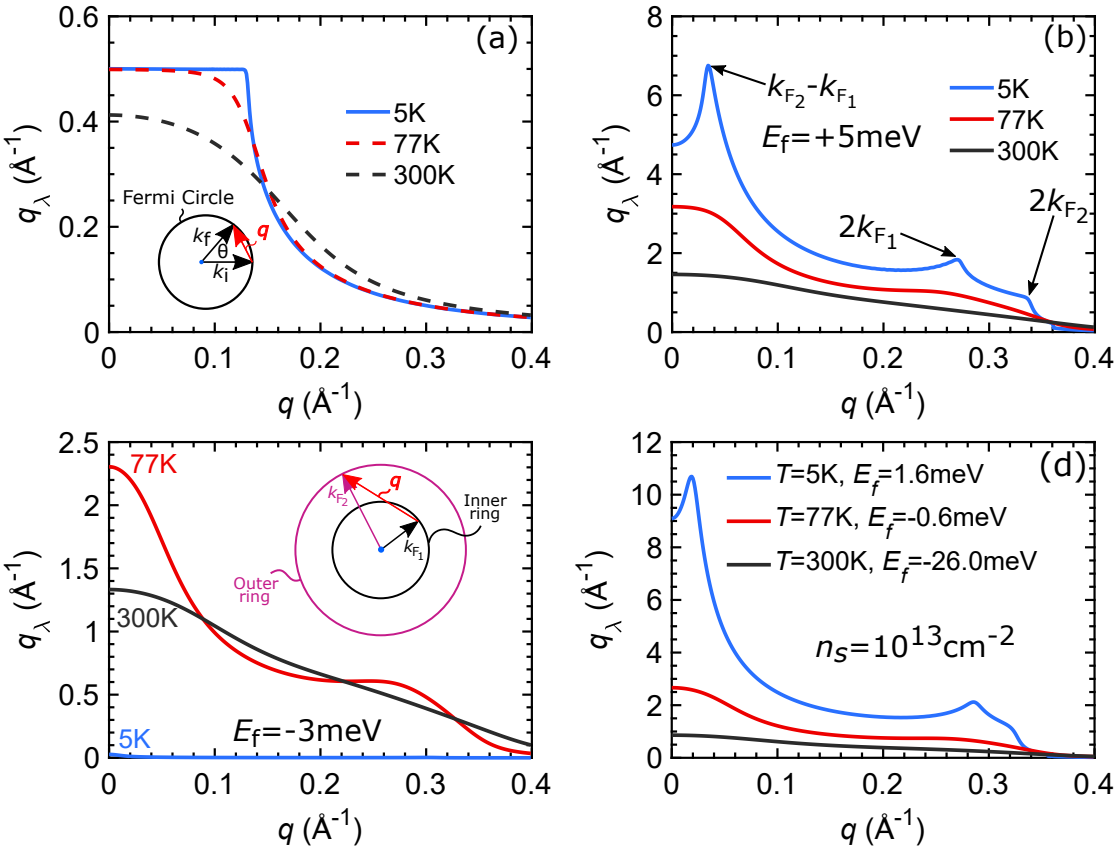

Figure 2.4: (a)–(c) $q_\lambda(q) \equiv -\frac{e^2}{2\epsilon}\Pi(q)$ at three different temperatures: 5 K, 77 K and 300 K. (a) $q_\lambda(q)$ for a parabolic dispersion with $E_F = 40$ meV. (b) $q_\lambda(q)$ for a Mexican hat dispersion with $E_F = +5$ meV. (c) $q_\lambda(q)$ for a Mexican hat dispersion with $E_F = -3$ meV. The inset shows the two iso-energy rings in momentum space of the Mexican hat dispersion. The momentum transfer q between two rings is shown. (d) $q_\lambda(q)$ for a Mexican hat dispersion for a fixed charged density of 10^{13} cm^{-2}. The corresponding Fermi energies at each temperature are shown on the graph. For both the parabolic and Mexican hat dispersions, the band structure parameters are the same as those used in Fig. 2.2, and the dielectric constant is $\epsilon = 3.1\epsilon_0$.

momentum required to transfer between the two Fermi rings. This can be viewed as a type of Fermi surface nesting. Increasing the temperature smooths out these sharp features, and at $T = 300$ K, $\Pi(q)$ smoothly decreases with increasing q. When the Fermi level is 3 meV below the band edge as in Fig. 2.4(c), the screening at $T = 5$ K is essentially zero since there are no carriers, and the qualitative features of the polarization functions at 77 K and and 300 K are the same as those in Fig. 2.4(b) with a small reduction in the overall magnitude resulting from the reduced carrier density.

Fig. 2.4(d) shows the inverse screening lengths at a fixed carrier density of 10^{13} cm^{-2} for different temperatures. Now, the Fermi level moves with temperature as shown in the legend. At 5 K, the Fermi level is 1.6 meV above the band edge, and the small q peak becomes very large as the Fermi level approaches the $1/\sqrt{E}$ singularity in the density of states. At 77 K and 300 K, the Fermi levels are in the band gap, and the polarization functions are similar to those in Fig. 2.4(c).

Now, we consider the magnitude and angle dependence of the matrix elements $\langle \mathbf{k}|\tilde{V}|\mathbf{k}'\rangle$ of the screened Coulomb potential, given by Eq. (2.6) with $q = |\mathbf{k} - \mathbf{k}'|$ and $z = z_0$. Fig. 2.5 shows polar plots of the screened Coulomb potential with $n_s = 10^{13}$ cm^{-2} at two different temperatures and energies. The polar angle θ is the angle between $\mathbf{k}$ and $\mathbf{k}'$. The relevant q_λ plots are shown in Fig. 2.4(d). For a fixed energy, scattering can occur within the inner ring ($\mathbf{k}$ and $\mathbf{k}'$ both lie on the inner ring), within the outer ring ($\mathbf{k}$ and $\mathbf{k}'$ both lie on the outer ring), or between the inner ring and the outer ring ($\mathbf{k}$ and $\mathbf{k}'$ lie on different rings). These 3 different matrix elements are denoted 'Inner,' 'Outer,' and 'Inter,' respectively, in Fig. 2.5.

We first consider the low-temperature $T = 5$ K matrix elements at an energy of 2.5 meV above the band edge shown in Fig. 2.5(a). At the carrier density of $n_s = 10^{13}$ cm^{-2}, $E_F = 1.6$ meV, The wave–vector dependent screening q_λ corresponds to the upper curve in Fig. 2.4(d), and a more detailed view is shown in Fig. 2.5(c). At $E = 2.5$ meV, the radius of the inner ring $k_1 = 0.142\,\text{Å}^{-1}$, the radius of the outer ring $k_2 = 0.165\,\text{Å}^{-1}$, and $k_2 - k_1 = 0.023\,\text{Å}^{-1}$. At $\theta = 0°$, $q = 0$ for the inner and outer ring matrix elements and $q = k_2 - k_1 = 0.023\,\text{Å}^{-1}$ for the inter ring matrix element. At $q = 0$, $q_\lambda = 9.1\,\text{Å}^{-1}$, and at $q = 0.023\,\text{Å}^{-1}$, $q_\lambda = 9.9\,\text{Å}^{-1}$. Thus, at $\theta = 0°$, all three scattering mechanisms are strongly suppressed by the screening. The $\theta = 0°$ inter ring scattering is a backscattering process, since the two rings have opposite velocities. Thus, the small q inter ring backscattering is strongly suppressed by the screening. The values of q, q_λ and $q + q_\lambda$ are plotted in Fig. 2.5(c). The value of q_λ in the range of $0 \leq q \leq 2k_{F_2}$ is much larger than q. This means that for $q \leq 2k_{F_2}$, the q dependence of $V(q)$ is determined solely by the q dependence of the polarization, and the bare momentum transfer q is negligible in comparison.

Since q_λ falls rapidly as q increases, the RPA screened Coulomb potential in a Mexican hat bandstructure favors large angle scattering. This is opposite to the trend resulting from the bare $1/q$ Coulomb interaction. The large outer-ring matrix elements for θ between 150° and 210° arise because the momentum transfer around the outer ring becomes larger than $2k_{F_2}$. The kink at 120° corresponds to the peak in q_λ at $2k_{F_1}$. At low temperature, the polarization strongly suppresses the magnitude of the matrix elements at the Fermi level. Only for those energies several k_BT above the Fermi level can the momentum transfer become large enough that the polarization becomes negligible, and $V(q)$

returns to a $1/q$ dependence. This large momentum transfer corresponds to backscattering across the outer ring.

Fig. 2.5(b) shows the $T = 300$ K matrix elements at an energy of 25 meV above the band edge. As the temperature increases to 300 K, both the magnitude and the angular dependence of the matrix elements change considerably compared to those at $T = 5$ K. This is a result of the large change in the polarization function as shown in Fig. 2.4(d). An enlarged view of the $T = 300$ K q_λ curve is shown in Fig. 2.5(d). The Fermi level now lies below the band edge at $E_F = -26$ meV. Compared to the $T = 5$ K polarization, the magnitude of the polarization decreases by an order of magnitude at the bandedge, the sharp features disappear, and q_λ monotonically decreases as q increases. However, the overall decrease of $q + q_\lambda$ over the range of relavant q values is relatively small. At $E = 25$ meV, $k_1 = 0.11$ Å^{-1} and $k_2 = 0.187$ Å^{-1}. At $q = 0$, $q + q_\lambda = 0.861$ Å^{-1}, and at $q = 2k_2 = 0.374$ Å^{-1}, $q + q_\lambda = 0.462$ Å^{-1}. Thus, the maximum increase in the matrix element going from $\theta = 0$ to $\theta = 180°$ is a factor of 1.8, which is shown for the matrix elements of the outer ring in Fig. 2.5(b). Over the entire range of relevent momentum transfer q, the $T = 300$ K polarization is much less than the $T = 5$ K polarization, so that the matrix elements are uniformly larger at $T = 300$ K compared to those at $T = 5$ K. Since the scattering rate is proportional to $|V(q)|^2$, the scattering rates will be significantly larger at room temperature compared to those at low temperature.

The integrand that determines the momentum scattering rates at a given energy E, given by Eq. (2.12), contains not only $|V(q)|^2$, but also the final density of states and the relative change in the velocity which can be positive or negative. The $[1 - \frac{v'}{v}\cos(\theta_{\mathbf{v},\mathbf{v}'})]$

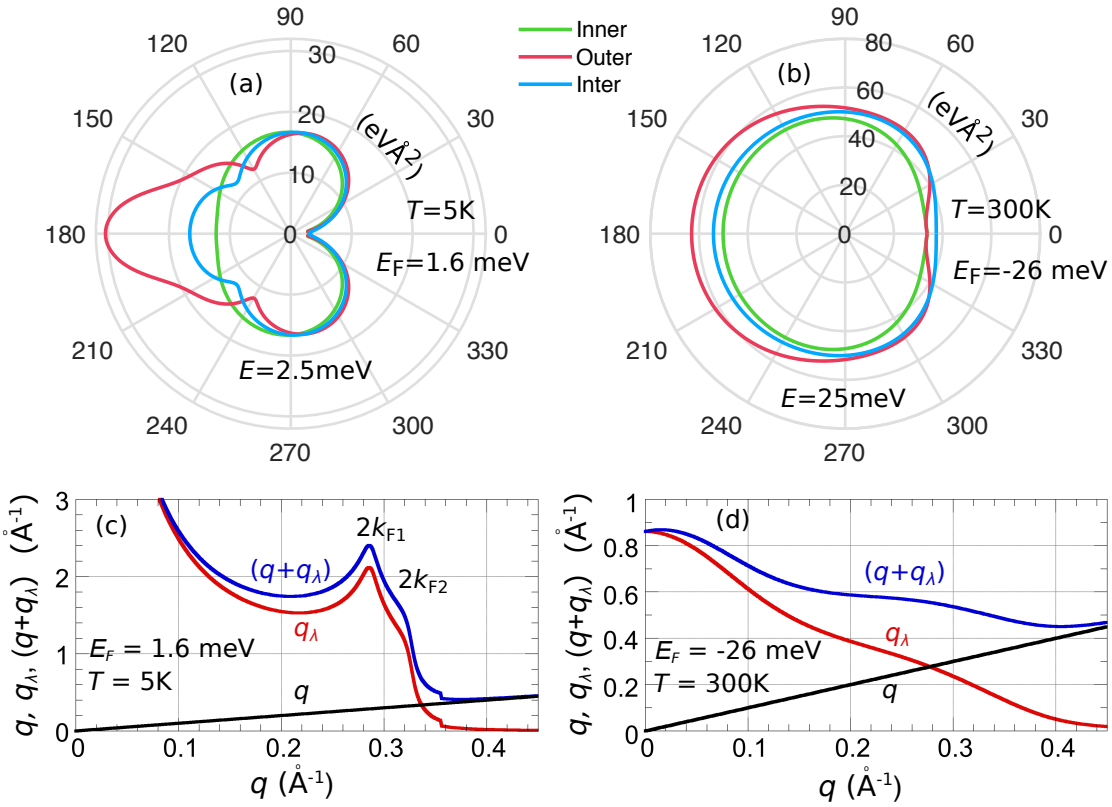

Figure 2.5: Polar plots of the matrix elements of the RPA screened Coulomb potential as a function of scattering angle at (a) $T = 5$ K and $E = 2.5$ meV and (b) $T = 300$ K and $E = 25$ meV. The polar angle θ is the angle between $\mathbf{k}$ and $\mathbf{k}'$. The legend refers to the 3 curves in each polar plot. "Inner" denotes matrix elements with $\mathbf{k}$ and $\mathbf{k}'$ both on the inner ring, "Outer" denotes matrix elements with $\mathbf{k}$ and $\mathbf{k}'$ both on the outer ring, and "Inter" denotes matrix elements with $\mathbf{k}$ on the inner ring and $\mathbf{k}'$ on the outer ring. (c) q, q_λ, and $q + q_\lambda$ as a function of q corresponding to (a). (d) q, q_λ, and $q + q_\lambda$ as a function of q corresponding to (b). The carrier density is fixed at 10^{13} cm^{-2} for all figures.

term further reduces the small angle intra-ring matrix elements, which are already small due to the large polarization at small q. The integrand of Eq. (2.12) is plotted in Fig. 2.6 at $T = 300$ K, $E_F = -26$ meV, and $E = 100$ meV. Fig. 2.6(a) shows the angle-dependent scattering rate for the initial k on the inner ring, and Fig. 2.6(b) shows the angle-dependent scattering rate for the initial k on the outer ring. Note that the energy $E = 100$ meV is 10 meV below the top of the hat in Fig. 2.2(a). At this energy, the magnitude of the group velocity of a state on the inner ring is much less that of a state on the outer ring. For inter ring scattering from the inner ring to the outer ring, $v' > v$, and a forward scattering process with $\theta_{\mathbf{v},\mathbf{v}'} = 0$ causes the $[1 - \frac{v'}{v}\cos(\theta_{\mathbf{v},\mathbf{v}'})]$ term in the integrand to become negative. The forward scattering process with $\theta_{v,v'} = 0^\circ$ corresponds to backscattering in k-space with $\theta = 180^\circ$, where θ is the angle between the initial state k on the inner ring and the final state k' on the outer ring. Thus, in Fig. 2.6(a), the negative values of $1/\tau(\theta)$, shown by the blue curve, are centered around $\theta = 180^\circ$. Backscattering with $\theta_{v,v'} = 180^\circ$ corresponds to forward scattering in k-space with $\theta = 0^\circ$, and the corresponding positive values of $1/\tau(\theta)$ are shown by the red curve centered around $\theta = 0^\circ$. When scattering from the outer ring to the inner ring, $v'/v < 1$, so that $1/\tau(\theta)$ is positive for all angles as shown in Fig. 2.6(b).

Fig. 2.6(c) shows the 4 components of the total scattering rate as a function of energy at $T = 300$ K. The energy 100 meV corresponds to the polar plots shown in (a) and (b). As the energy approaches the top of the hat, 110 meV, the radius k_1 of the inner ring goes to zero, so that $q = |\mathbf{k}_2 - \mathbf{k}_1|$ becomes independent of θ. The denominator in Eq. (2.6) is then independent of θ, the $\cos(\theta_{v,v})$ term integrates to zero, and the integral over θ gives 2π. Thus, in the limit E approaches ϵ_h from below, the integral in Eq. (2.12) can

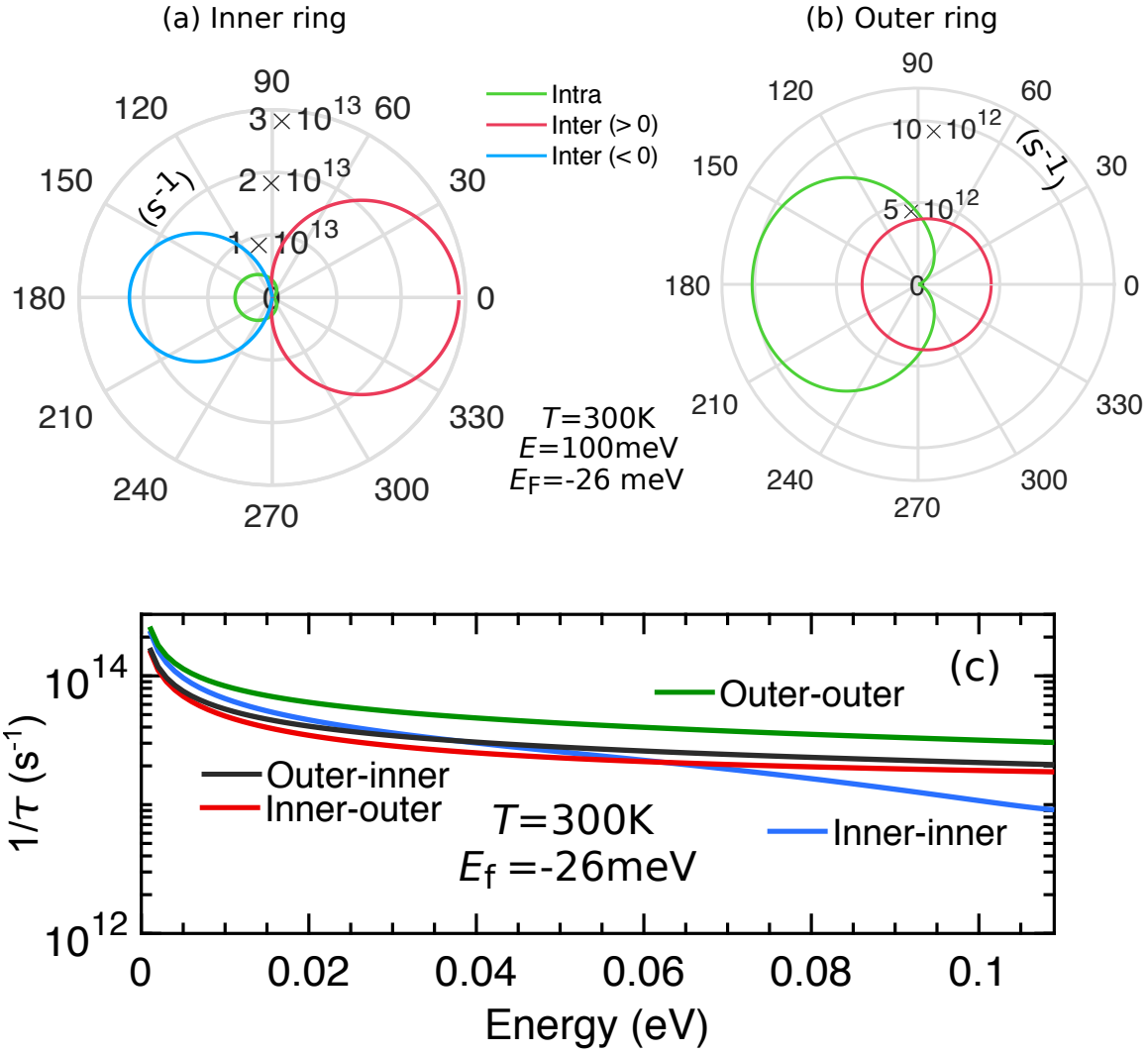

Figure 2.6: Polar plots of $1/\tau(\theta)$ given by the integrand of Eq. (2.12) for (a) k on the inner ring and (b) k on the outer ring. Inter-ring and intra-ring rates are indicated by the legend. Inter-ring contributions can be either positive or negative. (c) Four components of the total scattering rate as a function of energy. The components are indicated by the legends where, for example, "Inner-outer" denotes the initial state on the inner ring and the final state on the outer ring.

be performed analytically for both inter-ring scattering and intra-ring scattering within the inner ring. At $E = \epsilon_h$, the single-spin density of states of both the inner ring and the outer ring are equal to $\frac{m^*}{2\pi\hbar^2}$. For inter-ring scattering, $q = k_2$, and the inter-ring scattering rate is

$$\begin{aligned}\frac{1}{\tau_{\text{inter}}} &= \frac{n_I e^4}{4\epsilon^2\hbar}\frac{m^*}{2\pi\hbar^2}\frac{2\pi}{\left(k_2 + q_\lambda(k_2)\right)^2} \\ &= 4\pi^2\alpha^2\frac{m_0c^2}{\hbar}\frac{m_r}{\epsilon_r^2}\frac{n_I}{\left(k_2 + q_\lambda(k_2)\right)^2} \\ &= 2.06 \times 10^{13}\ \text{s}^{-1}\end{aligned} \tag{2.16}$$

where $k_2 = 2\sqrt{2m^*\epsilon_h}/\hbar = 0.217\ \text{Å}^{-1}$ and $q_\lambda(k_2) = 0.364\ \text{Å}^{-1}$. In the second line of Eq. (2.16), α is the fine structure constant, m_0 is the bare electron mass, c is the speed of light, $m_r = 0.409$ is the relative mass, and $\epsilon_r = 3.1$ is the relative dielectric constant. For intra-ring scattering within the inner ring, $q \to 0$, and the intra-ring scattering rate becomes

$$\frac{1}{\tau_{\text{intra}}} = 4\pi^2\alpha^2\frac{m_0c^2}{\hbar}\frac{m_r}{\epsilon_r^2}\frac{n_I}{q_\lambda^2(0)} = 9.38 \times 10^{12}\ \text{s}^{-1} \tag{2.17}$$

where $q_\lambda(0) = 0.861\ \text{Å}^{-1}$. The reduction of $1/\tau_{\text{intra}}$ with respect to $1/\tau_{inter}$ is solely the result of the increased value of q_λ as $q \to 0$. The largest component to the total scattering rate is from scattering within the outer ring. Scattering within the outer ring allows for the largest momentum transfer q and thus the smallest values of q_λ.

The total scattering rates for an initial state on the inner or the outer ring are shown in Fig. 2.7 for the same charge density ($10^{13}\ \text{cm}^{-2}$) and termperatures as in Fig. 2.4(d). The parameters are also the same as the ones used in the calculation of the screened Coulomb matrix elements in Figs. 2.5 and 2.6. At $T = 5$ K, as a result of the extremely large polarization, the scattering rate is suppressed for energies below 14 meV. At $E = 14$

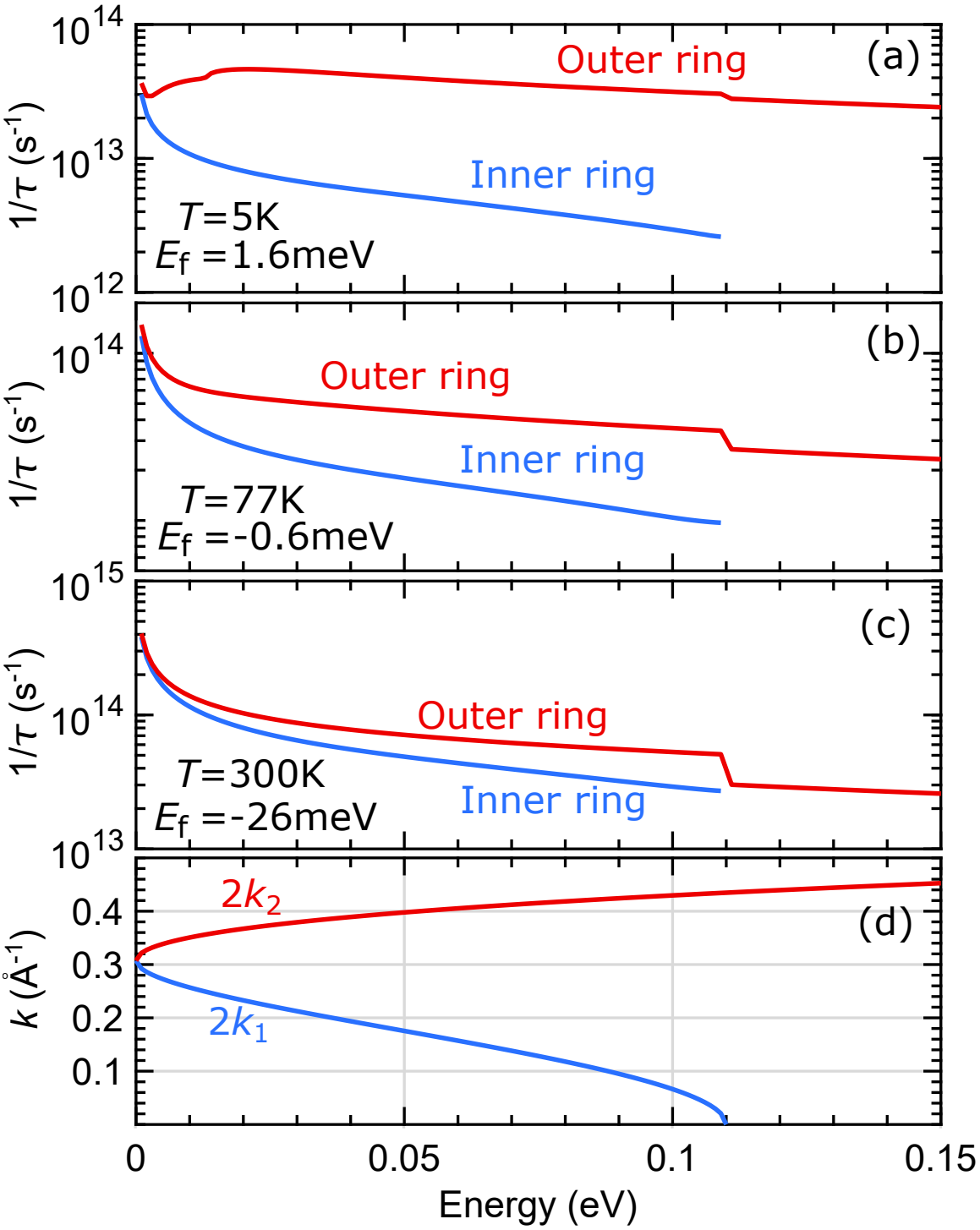

Figure 2.7: Momentum scattering rates for a charge density of 10^{13}cm^{-2} at (a) 5 K, (b) 77 K and (c) 300 K. The band parameters correspond to the ones used in Fig. 2.2, and the polarization functions are shown in Fig. 2.4(d). (d) Maximum values of q for scattering from the outer ring ($2k_2$) or within the inner ring ($2k_1$) as a function of energy.

meV, $2k_2 = 0.36$ Å^{-1}. At energies below 14 meV, the polarization is large for all possible momentum transfer q, the matrix elements of the screened Coulomb potential are reduced, and the scattering rate is reduced. The low-energy minimum occurs at $E = 2.5$ meV, when the minimum inter-ring scattering momentum $q = 0.023$ Å^{-1} is where the polarization function has its maximum value. As the energy decreases below 2.5 meV towards the bandedge, the $1/\sqrt{E}$ density of states term in Eq. (2.12) takes over, and the rate increases as $E \to 0$. For momentum transfer $q \gtrsim 0.36$ Å^{-1}, the polarization is negligible, and the RPA screened potential reverts to the bare unscreened potential as shown in Fig. 2.5(c). As the energy increases above 14 meV, unscreened backscattering takes place within the outer ring. The energy dependence for higher energies is governed by the energy dependence of the density of states and the $1/q^2 \approx 1/4k_2^2$ dependence of the matrix element squared.

The radius k_1 of the inner ring is maximum at $E = 0$ and decreases with increasing energy. Thus, the polarization relevant to the inner ring matrix elements increases with energy, causing the matrix elements to decrease. The density of states monotonically decreases and the scattering rate for states on the inner ring monotonically decreases with energy. The total rate is dominated by the intra-ring scattering of the outer ring.

At $T = 77$ K, the polarization loses its sharp features and its magnitude is everywhere reduced causing an overall increase of the scattering rates and a monotonic decrease with energy. This trend is more pronounced at $T = 300$ K where there is relatively little change in the sum $q + q_\lambda$ over the range of relevant energies, and the energy dependencies of the rates are determined by the $1/\sqrt{E}$ dependence of the density of states.

The total scattering rates for GaS and InSe are shown in Fig. 2.8 for temperatures of 5 K, 77 K and 300 K. The temperature dependence of the overall magnitudes of the scattering rates are determined by the magnitudes of the matrix elements squared of the screened Coulomb potential, which, in turn, are determined by the temperature dependence of the polarization functions as shown in Figs. 2.4(d) and 2.5. When the energy is equal to the height of the hat, the contribution from the inner-ring scattering disappears giving an abrupt decrease in the total scattering rate at $T = 77$ K and 300 K. At $T = 5$ K, the scattering rate from the inner ring is always small compared to that of the outer ring (except right at the bandedge), so that the small discontinuity at $E = \epsilon_h$ is primarily the result of the disappearance of the inter-ring scattering from the outer ring to the inner ring. For energies above the top of the hat, the rates become almost identical differing by at most a factor of 1.2 for InSe. The fine differences result from the details of the different Fermi levels combined with the different thermal broadening for each different temperature. The large decrease in the $T = 5$ K, low-energy scattering rate for InSe compared to GaS is the result of the larger polarization in InSe due to its larger mass and larger density of states.

The temperature and charge density dependence of the mobility are plotted in Fig. 2.9. Both the temperature dependence and the density dependence of the mobiliy are primarily governed by the temerature and density dependence of the polarization. The initial decrease in mobility with temperature results from the decrease in polarization with temperature as shown in Fig. 2.4(d). The decrease in screening, increases the matrix element squared which increases the scattering rate and decreases the mobility. At $T = 300$ K, there is a significant contribution to the integrand ($\mu(E)$) of Eq. (2.15) from energies

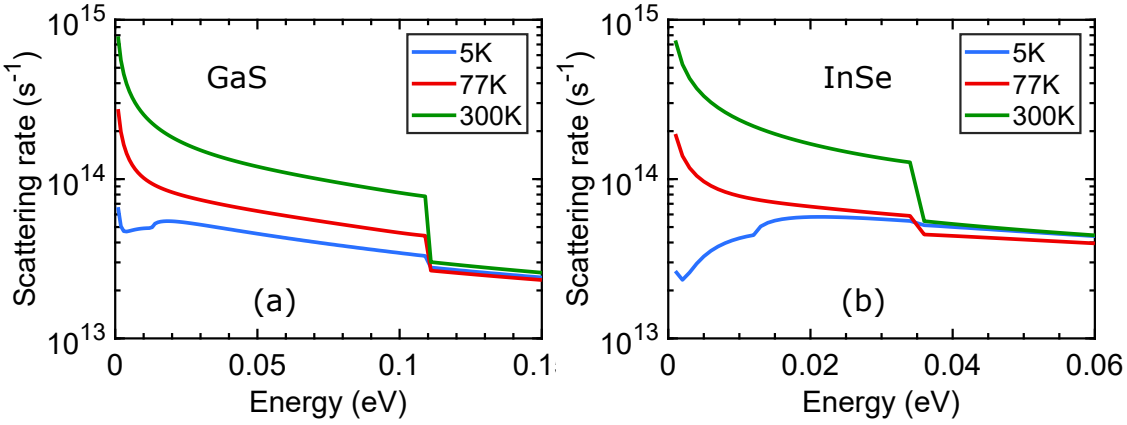

Figure 2.8: Energy dependence of the total momentum relaxation rates for (a) GaS and (b) InSe for 3 different temperatures. The charge density is fixed at 10^{13}cm^{-2}. Parameters used for GaS and InSe are tabulated in Table 2.1.

above ϵ_h. Once $E = \epsilon_h$ starts to fall inside the thermal window defined by $-\partial f_0/\partial E$ in Eq. (2.15), the sudden decrease in $1/\tau(E)$ shown in Fig. 2.8, gives rise to a corresponding increase in $\mu(E)$, so that the integral begins to increase with temperature. The 'turn-on' or 'thermal activation' of the mobility starts to be seen at lower temperatures for lower carrier densities as shown in Fig. 2.9(a). For lower carrier densities, screening is less, the matrix elements and scattering rates are larger at lower energies, the low-energy values of $\mu(E)$ are reduced, and the discontinuity at $E = \epsilon_h$ is larger so that the higher energies give a disproportionally larger contribution to the mobility.

For a fixed temperature, as the charge density increases, the screening increases, which reduces the matrix element squared and the scattering rates and increases the mobility as seen in Fig. 2.9(b). At a charge density of 5×10^{13} cm^{-2}, the mobility is between $100-200$ cm^2/V·s for the 3 temperatures, 5 K, 77 K, and 300 K.

Material	Effective mass m* (m_0)	Height of the hat (ϵ_h) (meV)	Relative permittivity
GaS	0.409	111.2	3.10
GaSe	0.600	58.7	3.55
InS	0.746	100.6	3.08
InSe	0.926	34.9	3.38

Table 2.1: Effective mass and height of the hat for III-VI materials with Mexican hat [176].

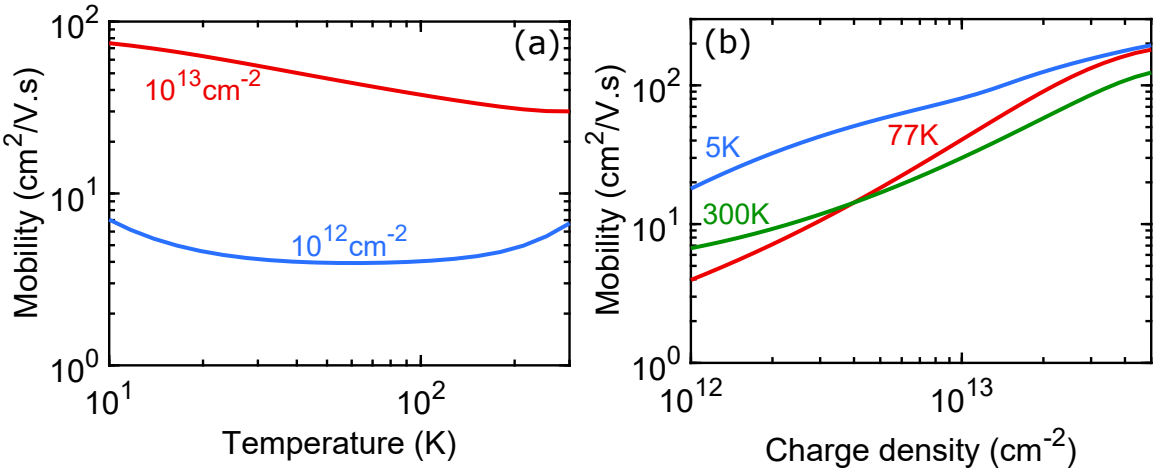

Figure 2.9: Charged impurity limited hole mobility of GaS (a) as a function of temperature for a carrier density of 10^{12} cm^{-2} (blue) and 10^{13} cm^{-2} (red) and (b) as a function of carrier density at 5 K (blue), 77 K (red) and 300 K (green) for a fixed charge density of 10^{13} cm^{-2}. The impurity density n_I is fixed at 10^{12} cm^{-2}.

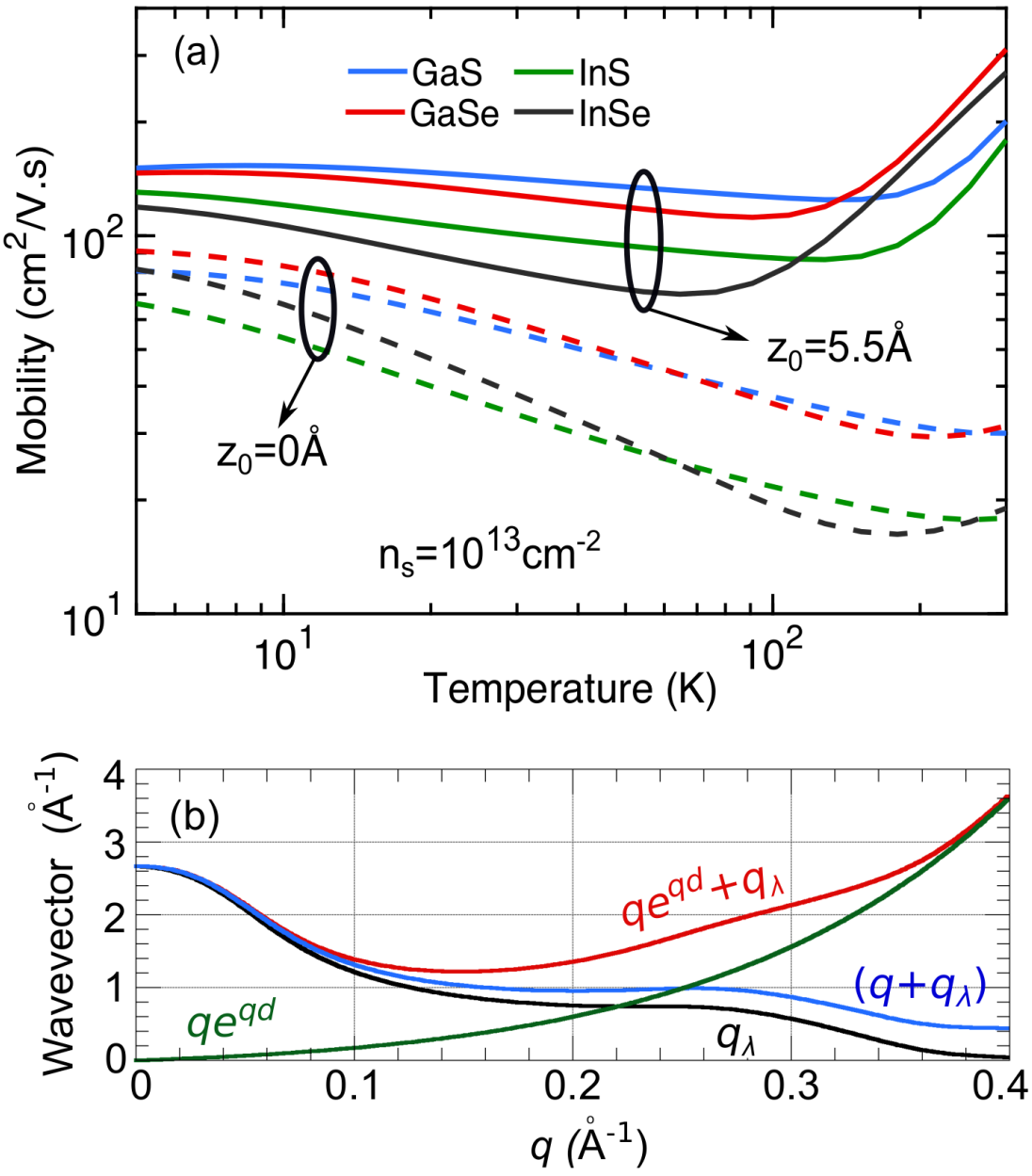

Figure 2.10: (a) Charged impurity limited monolayer hole mobility as a function of temperature of GaS, GaSe, InS and InSe with the charged impurities in the middle of the channel ($d = 0$, dashed line) and on the substrate ($d = 5.5$ Å, solid line). (b) qe^{qd}, q_λ, $q + q_\lambda$, and $qe^{qd} + q_\lambda$ for GaS at $T = 77$ K where $d = 5.5$ Å. The hole density $n_s = 10^{13}$ cm^{-2}, and the charged impurity density n_I is fixed at 10^{12} cm^{-2}.

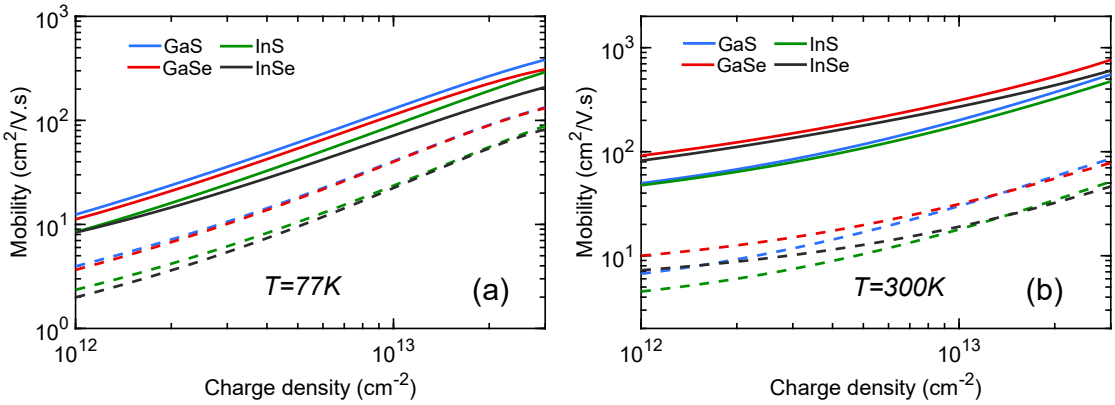

Figure 2.11: Charged impurity limited monolayer hole mobilities as a function of carrier density at (a) $T = 77$ K and (b) $T = 300$ K for the 4 III-VI materials as indicated by the legends. Solid lines result from charged impuriies on the substrate ($z_0 = 5$ Å), and the dashed lines result from charged impurities in the middle of the channel ($z_0 = 0$). The impurity density n_I is fixed at 10^{12} cm^{-2}.

The temperature dependence of the 4 III-VI p-type materials are shown in Fig. (2.10) for a fixed hole density of 10^{13} cm^{-2} and two different positions of the charged impurities, in the middle of the channel ($z_0 = 0$Å) and on the substrate ($z_0 = 5.5$ Å). The relevant material parameters are given in Table 2.1. The general trends of the temperature dependence follow those seen in Fig. 2.9. The low temperature mobilities order according to the effective masses with the lower masses correlating with the higher mobilities. However, the dependence is weaker than a $1/m^*$ dependence. The minimum and maximum effective mass differ by a factor of 2.3, and at $T = 5$ K, the mobilities differ by a factor of 1.4. The difference in mobilites increases to a maximum of 2 near the beginning of the high-temperature crossover where the mobilities start to increase. The cross-over begins at a lower temperatures for the materials with a smaller value of ϵ_h, since lower temperatures can thermally excite carriers above the top of the hat.

Moving the charged impurities from the middle of the channel to the substrate increases the mobility, as would be expected, since the charged impurities are further away from the carriers. However, it also lowers the temperature of the high-temperature crossover, which is not an obvious consequence. The reason lies in the large enhancement of the bare, large-wavevector screening as shown in Fig. 2.10(b) for GaS at $T = 77$ K. For GaS, the bare term qe^{qd} in the denominator becomes larger than q_λ at $q = 0.22$ Å^{-1}. The minimum value of $2k_2$ is 0.31 Å^{-1} at the bandedge, and at the top of the hat, $2k_2 = 0.43$ Å^{-1}. At that value of q, the denominator $qe^{qd} + q_\lambda$ is larger than at $q = 0$, so that backscattering across the outer ring is strongly suppressed giving a large enhancement to $\mu(E)$ for energies $E = \epsilon_h$.

The hole density dependence of the charged impurity limited mobility at $T = 77$ K and $T = 300$ K is shown in Fig. (2.11). The mobility monotonically increases with hole density p_s for a fixed charged impurity density n_I. This trend would be expected due to increased screening resulting from the higher hole density. At the highest hole densities considered of 3×10^{13} cm^{-2}, with the charged impurities on the substrate, the $T = 300$ K mobilities lie between 500 and 800 cm^2/V·s for all 4 materials. With the impurities at the center of the channel, the mobilities decrease one order of magnitude and lie in the range of 50 to 80 cm^2/V·s. All mobilites are calculated for a charged impurity density of $n_I = 10^{12}$ cm^{-2}, and the mobilities are inversely proportional to n_I, so that all mobility values shown can be easily scaled for arbitrary values of n_I.

2.4 Conclusions

The Mexican hat type bandstructure that occurs in the valence band of monolayer and few layer III-VI materials and other 2D materials gives rise to unique screening properties. The singular density of states at the bandedge and the two Fermi wavevectors up to the height of the hat, lead to large screening and strong wavevector dependence of the screening. The wavevector dependence of the screened Coulomb interaction is so strong, that the temperature and density dependence of the matrix element squared is the dominant factor determining the overall trends with respect to temperature and density. The reduction of polarization with temperature causes an initial increase in scattering and decrease in mobility with increasing temperature. Short wavevector inter-ring backscattering and scattering within the smaller ring is always suppressed by the large polarization at small q. When the the charged impurities lie in the middle of the 2D channel, the wavevector dependence of the polarization favors large wavevector backscattering across the outer ring. When the charged impurities lie on the substrate, the bare screening increases rapidly at larger wavevectors suppressing the backscattering within the outer ring. For charged impuities on the substrate, the polarization suppresses the small wavevector scattering and the exponential wavevector dependence of the bare Coulomb interaction suppresses the large wavevector scattering across the outer ring leading to an overall increase in mobility. The suppression of the large wavevector scattering also reduces the temperature at which the mobility starts to increase when the charged impurities are on the substrate. The mobility monotonically increases with hole density up to the maximum value considered of 3×10^{13} cm^{-2} where it reaches a maximum value of 800 cm^2/Vs for GaSe with the charged impuri-

ties located on the substrate. Placing the impurities in the center of the channel reduces the maximum value by an order of magnitude. All mobility values are calculated for a charged impurity density of $n_I = 10^{12}$ cm^{-2} and scale inversely proportionally to n_I.

Chapter 3

Carbon Assisted Growth of Monolayer h-BN on Co (111)

3.1 Introduction

Layered hexagonal boron nitride (h-BN) is of great interest due to the wide range of applications which includes encapsulation of 2D material devices [170, 56, 35], to its use as a dielectric [105, 84, 24] or as an active layer in ultraviolet optoelectronic devices [96, 173, 172]. Achieving controlled growth of large area h-BN is crucial to enable use of h-BN in potential applications. Transition metal substrates based on Cu[85, 157], Ni[146, 72], Fe[86, 29], Pt[45, 83] have been used for chemical vapor deposition (CVD) growth of h-BN. One of the current limitations for controlled growth is the lack of substrates that result in low binding energies for B and N incorporation. Recent experimental efforts have demonstrated success in achieving large area growth of h-BN using Co(111) substrates [185]. Motivated

by this, we explore the mechanisms by which B and N can be incorporated in a stable manner on a Co(111) substrate.

The (111) surface of transition metal substrates is often used as a catalytic substrate for the growth of two-dimensional materials such as graphene and h-BN. The Cu(111) surface is a prime example of a substrate that has been widely used to achieve large area growth of graphene [44, 64, 122, 124]. Motivated by the experimental observation from Liu group, UCR we have calculated and compared absorption energies and migration barriers for different scenarios which explains the initial nucleation and adlayer growth of h-BN on Co (111) substrate.

3.2 Methodology

Our calculations are based on first-principles density functional theory (DFT) using the projector augmented wave method and the Perdew-Burke-Ernzerhof (PBE) type generalized gradient approximation [127, 41] as implemented in VASP [93]. Spin polarization is included self-consistantly in all calculations. A Monkhorst-Pack scheme was adopted to integrate over the Brillouin zone with a k-mesh of 9×9×1. A plane-wave basis cutoff of 550eV was used for all the calculations. All structures are optimized until the largest force on the atoms is less than 0.01 eV/Å. To model the adsorption energies of B and N atoms on a Co(111) surface, the adsorption is modeled using a single B or N atom on a four layers of 3×3 Co(111) surface. A vacuum of 15Å was introduced to avoid interactions between the periodically repeated surfaces. We have identified three stable sites on Co(111) where B and N adsorption can happen. These sites are illustrated in Fig. 3.1. The minimum energy

path for different reactions is identified by using the nudged elastic band method (NEB) which we use to obtain migration energies for the different adsorbates between the different sites of the Co(111) surface. The spring force between adjacent images is set to 5.0eVÅ^{-1}.

The surface energy of the substrate σ is defined as,

$$\sigma = \frac{E_{slab} - \sum N_i \mu_i}{2A} \tag{3.1}$$

where E_{slab} is the total energy of the substrate calculated from first principles, μ_i is the chemical potential of species i in the slab structure, N_i is the number of particles of the i-th element in the slab, and A is the area of the slab.

The adsorption energy of a B or N atom on the Co substrate is calculated from the difference in total energies,

$$E_b = E_{B/N\ on\ surface} - E_{B/N} - E_{surface} \tag{3.2}$$

where $E_{B/N\ on\ surface}$ is the total energy of a B or N atom on the surface of a

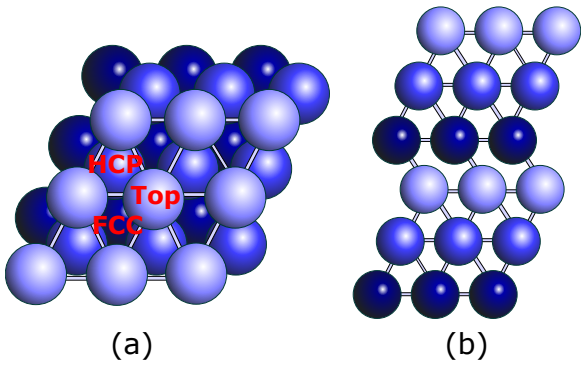

Figure 3.1: Schematic presentation of a Co(111) surface showing (a) top view and (b) side view. Cu(111) has the same structure as Co(111).

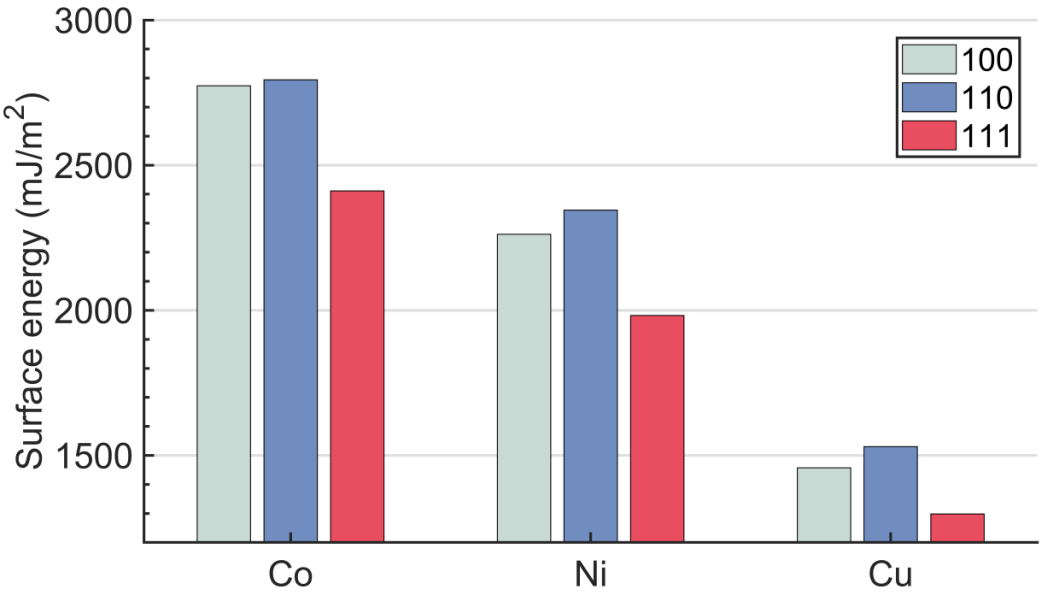

Figure 3.2: Surface energy of the different surfaces of Co, Ni and Cu.

supercell consisting of four layers of 4×4 Co atoms aligned in the (111) plane, $E_{B/N}$ is the chemical potential of the adsorbed B or N atom and $E_{surface}$ is the total energy of the isolated four layer 4×4 Co(111) supercell. We define our binding energy such that a negative value corresponds to a stable adsorption.

3.3 Results

We first report on surface energies for different surfaces of Co, Ni and Cu. As can be seen from Fig. 3.2, within three metals, Co has the largest of surface energy. From Bauer's thermodynamic criterion for the growth mode, larger surface energy of Co surfaces indicate higher probability of layer-by-layer growth of the h-BN. Within the (111) surface,

our calculated surface energy for Co(111) is 2037.87 mJ/m^{-2} compared to that of Cu(111) which is 1231.08 mJ/m^{-2}. Higher surface energy of Co(111) suggests higher wettability of Co(111) as substrate.

First, we determine the most favorable position of interstitial carbon within the substrate. It has been argued that when trace amount of carbon atoms, the interstitial atoms prefer sub-surface adsorption sites [4]. We consider octahedral and tetragonal site as adsorption sites and calculate adsorption energies for these adsorption sites. We find that the octahedral site is the most favorable site for the carbon atoms. To determine the epitaxial relationship of h-Bn to the Co(111) surface we calculate the adsorption energy of h-BN on different sites of the Co(111) surface and find that $B_{fcc}N_{top}$, has the lowest adsorption energy which is consistent with calculation performed on Ni(111) surface.58

As shown in Table 3.1, on Cu(111) surface the adsorption energy of B and N are positive for all three sites. B and N have have the lowest adsorption energy in HCP and FCC sites, respectively. The large positive binding energies for B and N on a Cu(111) indicates an additional mechanism is required by which h-BN growth can nucleate on such surfaces. This can be explained by the presence of defects, either in the form of extended defects such as grain boundaries or point defects which are commonly found on such transition metal substrates [106, 77, 58]. On Co(111) surface, the adsorption energies are lower for both B and N compared to Cu(111) surface. B and N both have lowest adsorption energy at HCP site of Co(111) surface. Adsorption energy for B on Co(111) surface is positive, while the same for N becomes negative. Which means N is more likely to nucleate on Co(111) compared to B. To explore what enables nucleation of B on Co(111) we consider a Co(111)

Adsorption Energy eV/atom	Boron			Nitrogen		
	FCC	HCP	On top	FCC	HCP	On top
Cu(111)	1.74	1.71	3.26	1.11	1.19	3.22
Co(111)	0.80	0.69	2.23	-0.26	-0.50	1.80
Co(111) With interstitial carbon	0.522	0.081	Not stable	-0.298	-1.062	Not stable

Table 3.1: Adsorption energies of boron and nitrogen on different surface configuration of Cu(111) and Co(111).

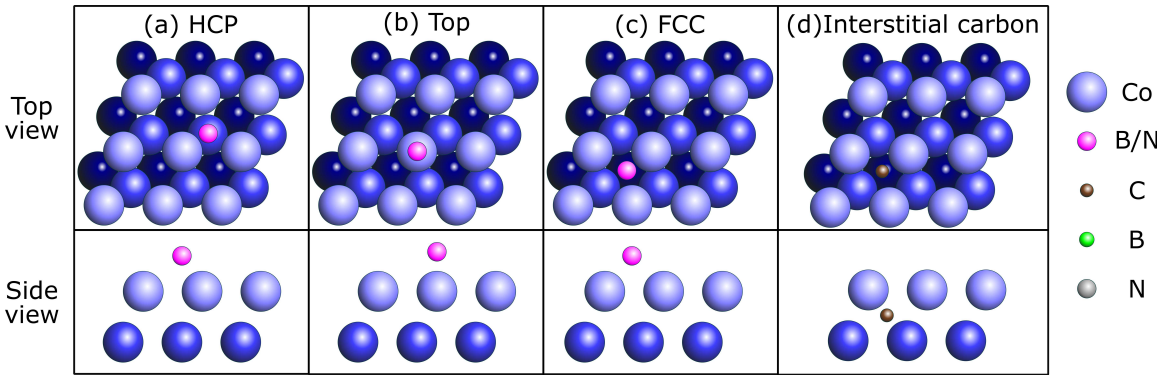

Figure 3.3: Top-view and side-view schematic of B/N atoms on (a) HCP, (b) Top, (c) FCC, and (d) interstitial carbon on an octahedral site of the substrate.

substrate with defects. In one case we consider a Co(111) surface with an interstitial Co atom on top of it.

For the both cases The adsorption energies are reduced when compared to a clean Co(111) surface. Which means a non perfect surface aids to the nucleation of B and N. Now we consider an interstitial carbon at the octahedral site which is 0.6Å below surface and calculate the adsorption energies of different sites for B and N. The adsorption energies for this case are further reduced for HCP and FCC sites. For the Top site both B and N are pushed away from the surface and hence can be considered unstable on Top site. The re-

duced adsorption energy with presence of interstitial carbon indicates that small percentage of interstitial carbon will help nucleation of h-BN to the Co(111) surface. When the interstitial carbon is present, both B and N have the lowest adsorption energy at the HCP site. To identify nucleation site for both, we calculated adsorption energy of a B-N dimer on FCC and HCP sites. The B_{FCC}-N_{HCP} dimer have a adsorption energy of -0.817eV/atom which is 0.147eV/atom lower than the B_{HCP}-N_{FCC} dimer which suggests the FCC and HCP sites are the most favorable sites for B and N, respectively when interstitial carbon is present.

The migration energies for B and N between the FCC and HCP site of Co(111) surface is shown in Fig. 3.4 and 3.5, respectively. For B the migration barrier from FCC to HCP site is 46meV and from HCP to FCC site the barrier is 297meV. This smaller migration barrier can enable the boron to migrate between the FCC and HCP site. Presence of interstitial carbon increases the barrier to 137meV (FCC to HCP) and 589meV (HCP to FCC). So the presence of interstitial carbon stabilizes the boron atom on the HCP site of Co(111) surface and aids to start nucleation. For N the barrier from FCC to HCP site remains the same with or without the presence of C atom. However, barrier from HCP to FCC site is increased to 1.169eV with presence of C atom from 0.662eV which is for clean Co(111) surface. Hence presence of carbon also stabilizes the N atom at the HCP site and aids in the nucleation.

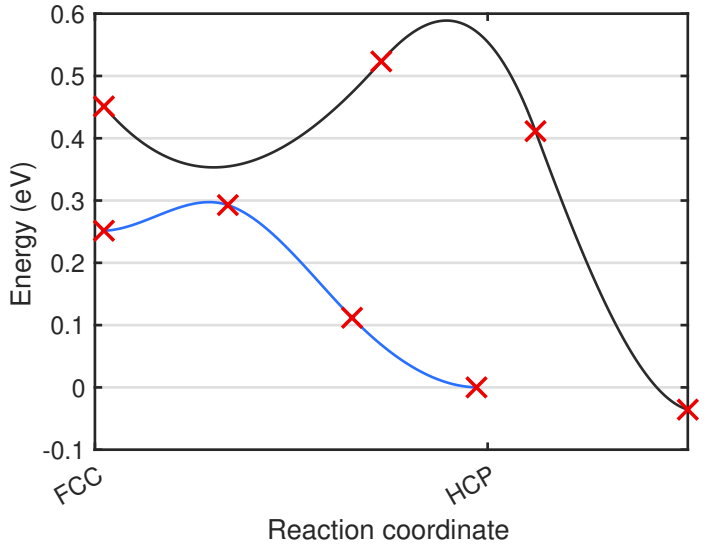

Figure 3.4: Minimum energy path calculated using NEB for boron. The blue and black line corresponds to clean Co(111) and Co(111) surface with interstitial carbon, respectively.

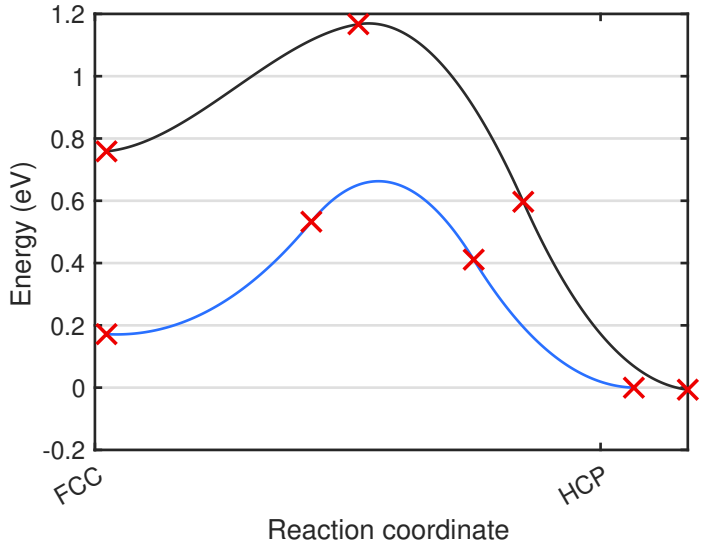

Figure 3.5: Minimum energy path calculated using NEB for nitrogen. The blue and black line corresponds to clean Co(111) and Co(111) surface with interstitial carbon, respectively.

3.4 Conclusions

In summary, we investigated Co as substrate for large area growth of h-BN. We find that interstitial atoms aid in the nucleation process of h-BN. Small amount of interstitial carbon also improves the adsorption of source elements and also stabilizes the boron and nitrogen atoms on the Co(111) surface. Overall Co(111) shows promise as a better substrate compared to commonly used Cu(111) substrate for MBE growth.

Chapter 4

Accessible computational materials design with high fidelity and high throughput

4.1 Introduction

Materials design and discovery based on first-principles modeling is an interdisciplinary research area that recently received much attention with multiple success stories reported in the field of catalysis, hydrogen storage materials, Li-ion batteries, photovoltaics, topological insulators, carbon capture, piezoelectrics, and thermoelectrics [74, 38, 139, 129, 6]. These efforts enabled the integration of computational materials science with information technology (e.g., web-based dissemination, databases and data-mining), expanded access to properties computed by first-principles modeling approaches to new communi-

ties and promoted new collaborative work. Nevertheless, when compared with the more established computer-aided design and engineering sector, there is still much room for improvement in the way first-principles modeling is performed with respect to the accessibility and repeatability of high fidelity calculations.

High-throughput virtual screening produced large repositories of data for its further consumption by other scientists, notably the Materials Project [74], AFLOW[38], and the open quantum materials database[139]. Other initiatives, like AIIDA[129], also provided a set of building blocks for the construction of the simulation workflows. Recently, other approaches like NOMAD[6], emerged with the idea of an open access data repository aimed to allow for advanced data analytics and the creation of machine learning models. Other notable example includes the Computational 2D Materials Database[54, 135] targeted at the applications in semiconductor area. The efforts above include a significant computer science aspect and created software tools that facilitate the execution of simulations in a high-throughput way, such as Pymatgen[125], Atomic Simulations Environment[100], AIIDA stack[129] and similar. These tools facilitate the adoption of the original techniques by other computational materials scientists and help organize and standardize the community efforts. Naturally, the data-centric approaches to the development of new materials followed after[2, 7, 169, 70, 171]. Additionally, the area of cloud computing as applied to the first-principles materials modeling emerged in the last few years[179, 18].

We present the approach conceived and implemented by Exabyte Inc. inside its web-based modeling platform since 2014. The approach is focused on the accessibility and repeatability of modeling workflows, is designed to support creation and execution of

multiscale models online, and is reminiscent to NanoHUB.org[89]. Compared to standalone software tools, such an approach allows users to focus on the physical essence of the problem and removes any obstacles related to the computational complexity, such as installation and parallelization concerns. Our approach enables access for (eg. experimental) scientists without direct knowledge of modeling techniques, promotes the exchange of ideas, and extends creative breadth of the resulting research. By relying on centrally-available cloud-based high performance computing the platform yields the computational power to facilitate high fidelity in a reproducible way[120], and its data-centric nature eliminates unnecessary repetition, facilitates collaboration, and embraces traceability, version control and other computer science paradigms[129].

In this manuscript we report the example application of the above platform[5] to the electronic structural properties of semiconducting materials. We use Density Functional Theory in the plane-wave pseudopotential approximation[62, 69] and obtain the electronic band structures and band gaps for a diverse set of 847 compounds ranging from pure elements to ternary oxides and further referred to as ESC-847. We provide the results for the Generalized Gradient Approximation [128], the Hybrid Screened Exchange[60] and the GW approximation[68]. We compare the results with the available experimental data and present the assessment of the accuracy levels for each model. For the first time ever this work presents all the following combined together: the results, the tools that generated the results, the simulations with all associated data, and an easy-to-access way to reproduce, improve and contribute results for other materials into a centralized ever-growing repository.[3].

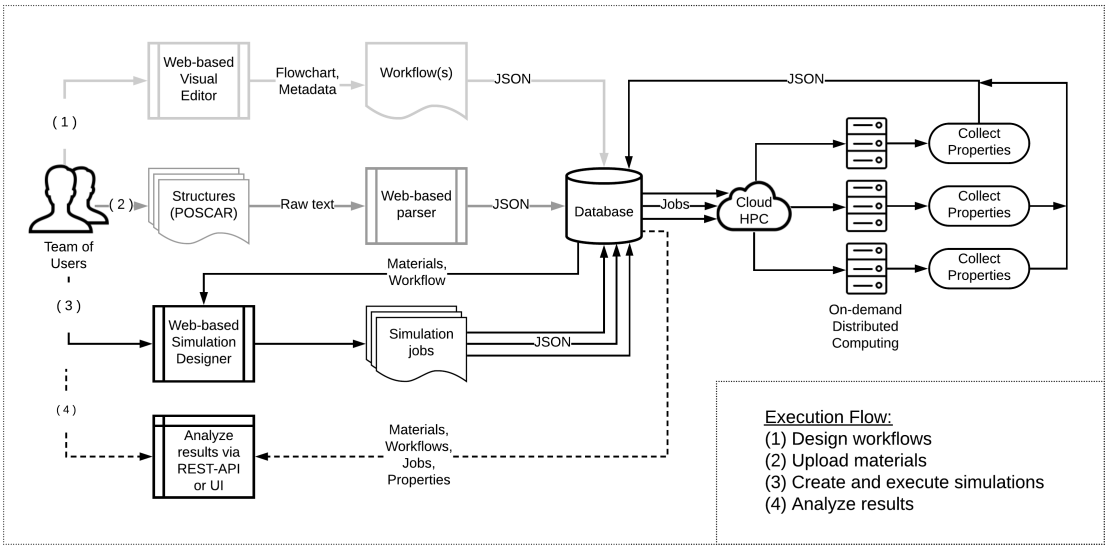

Figure 4.1: Flowchart with the execution logic of the simulations. Branch (1), shown in light gray, represents the initial design of the simulation workflow with its subsequent storage as JSON object in database. Branch (2), dark gray, illustrates the upload and conversion to database entries of the structural materials information. (3), in black, demonstrates the main execution logic for the creation and execution of simulation jobs. Finally, (4) denotes further analysis and is show using dashed black lines.

4.2 Methodology

4.2.1 General logic

Execution flow

We demonstrate the general execution flow employed in this work in Fig. 4.1. We start from the design of the simulation workflows (designated by (1) in the figure). We represent the logic of the workflows through a data structure encoded using a JavaScript Object Notation (JSON) using a data convention further referred to as Exabyte Data Convention (EDC). Next, we upload the initial structures for the materials to be studied (branch (2) in the figure). After that, we create and execute the simulation jobs using the cloud-based high-performance computing infrastructure assembled on-demand by our software (corre-

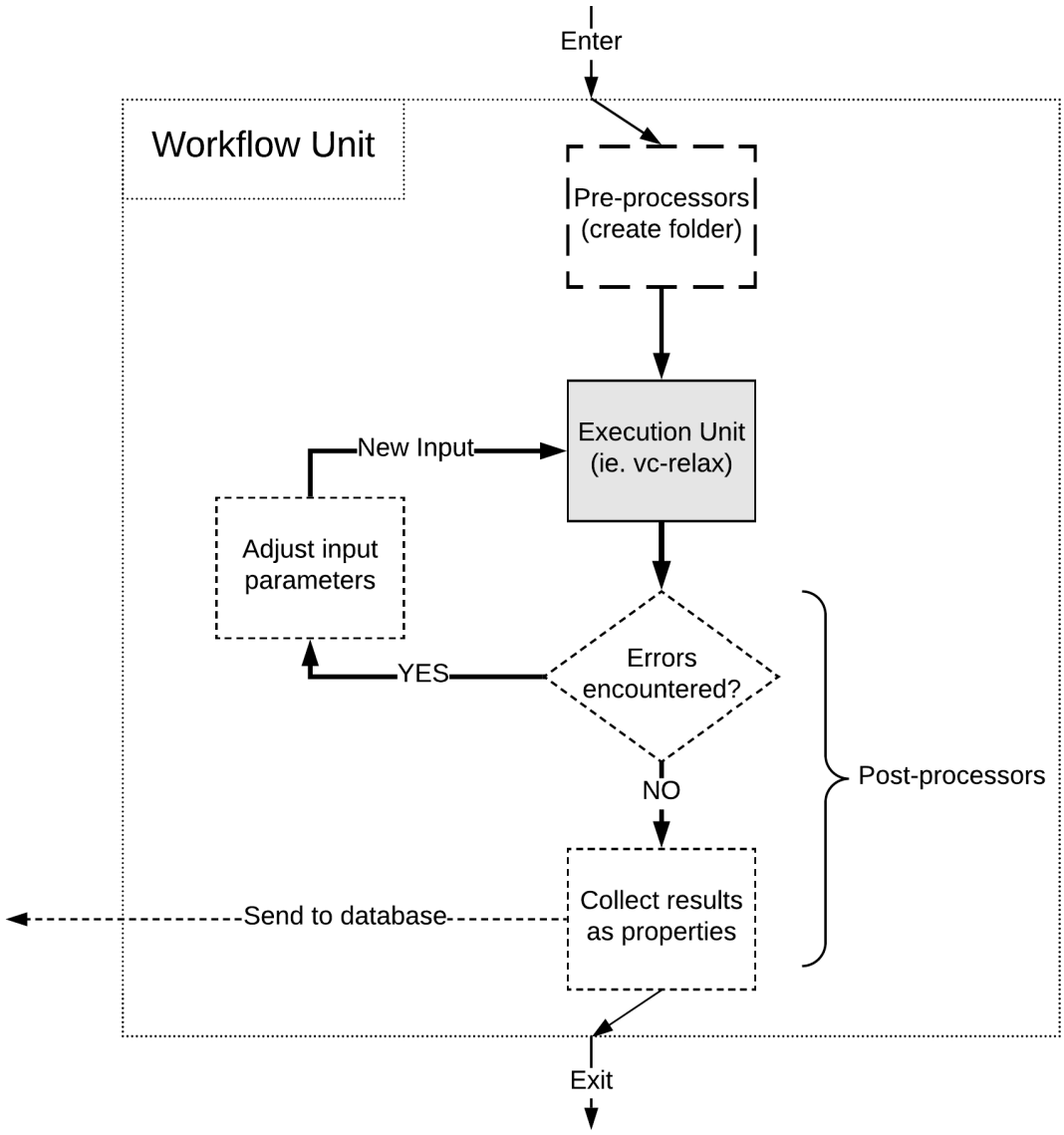

Figure 4.2: Example unit of a simulation workflow with a pre-processor, main execution part, and post-processors.

sponding to branch (3) in the figure), and collect the resulting properties in a database. Finally, we analyze the results either through a graphical user interface or by means of the

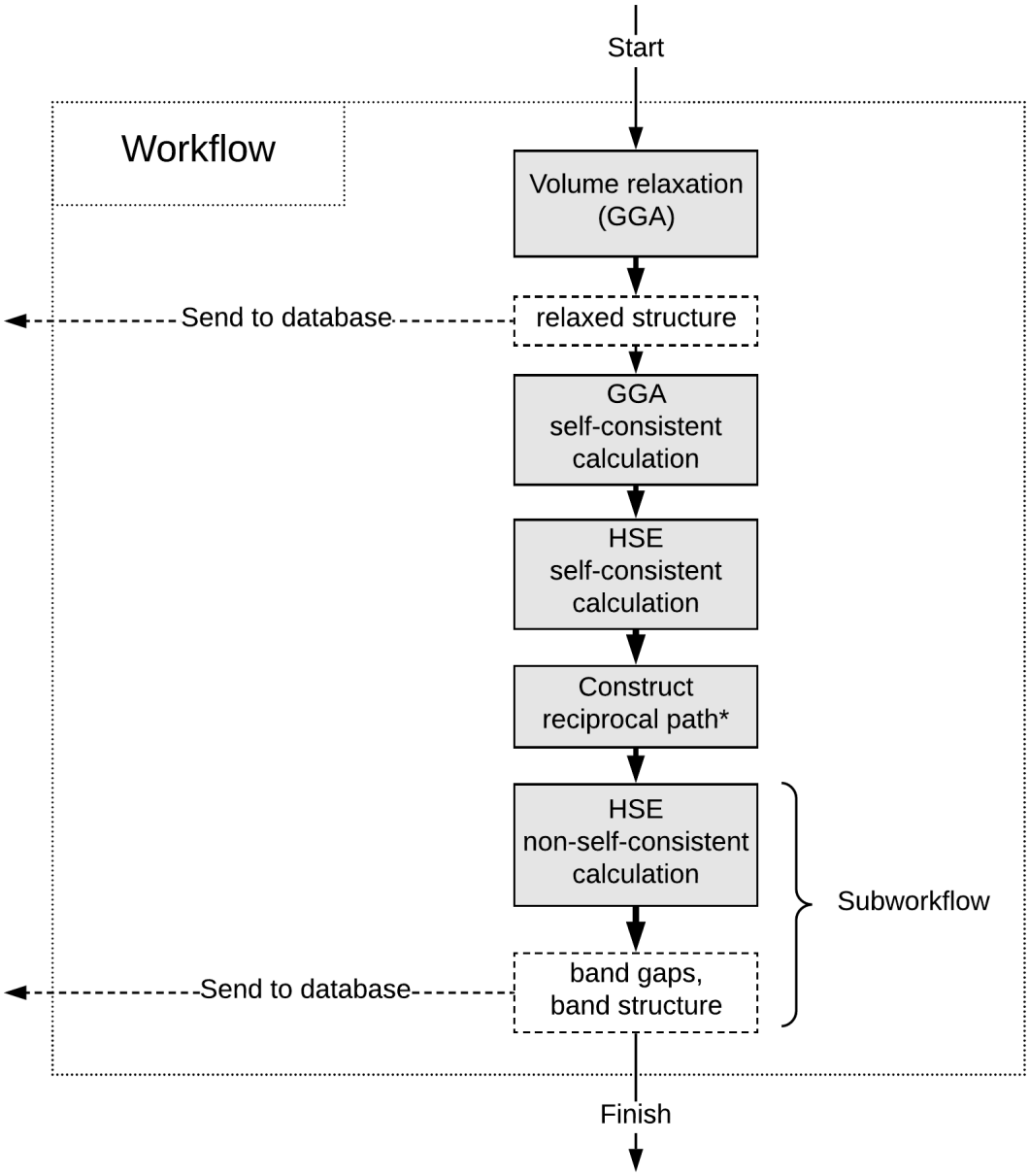

Figure 4.3: Simulation workflow for an HSE calculation. Post-processors (dashed) used to extract materials properties. (*) denotes an auxiliary intermediate step.

RESTful application programming interface (API). The general execution flow, including all the above components and the associated entities are freely available online. The users of

Exabyte platform can clone the associated entities (eg. materials, workflows) - and re-create our calculations in order to reproduce or further improve the results.

Workflow units

Within the EDC each workflow contains multiple units and each unit contains the corresponding input parameters for the simulation engine(s) used within. We logically separate each individual unit into pre-processors, main execution, and post-processors parts as demonstrated in Fig. 4.1. The pre-processors are ran before the main part and are used for auxiliary tasks, such as creating the required system folders for data on disk. The main execution part is where the main simulation is done. Post-processors are used to assert the completion of the simulation or attempt the main simulation again with a set of adjusted parameters. For the work described in this manuscript we used the error correction logic implemented in [74]. After asserting the validity of the simulation a set of material properties is extracted, organized into JSON data structures, and stored in the database.

Workflows

An example workflow for HSE calculations utilized in this work in shown in Fig. 4.1. We start with obtaining the relaxed structures, and then self-consistently pre-calculate the electronic wavefunctions and charge density. These steps are done within the GGA. Next, we repeat the self-consistent calculation, this time including the exchange interaction within HSE. Next, we run an auxiliary step to assist with the construction of the reciprocal path for the final part of the calculation - the non-self-consistent HSE calculation. The latter produces the resulting band gap and band structure properties.

4.2.2 Materials

All materials studied in this work constitute the E-847set and are divided in 7 categories according to their stoichiometric composition. The categories together with their shorthand names are listed in Table 4.1. We attempted to cover a diverse set of semiconductor stoichiometries accessible to the modeling from first principles. We prioritized compounds with smaller number of atoms within the crystal unit cell, however did not impose a hard limit on the unit cell size. Most of the structures studied have 4 or less atoms inside the unit cell, the largest unit cell has 32 atoms. We further sub-categorized materials into groups by the associated difficulty levels for the simulation workflows involved, as explained below. The details about the materials studied, including the corresponding categories and the results are given in Table 4.3. Our approach is similar to that of [59], with an attempt to improve the range of compounds studied and include materials with potential industrial applications.

4.2.3 Workflows

In order to organize the information about the simulation workflows we employ the categorization illustrated in Table 4.2. The categorization depends on: (a) whether the semi-core electronic states are included in the pseudopotentials, (b) whether the treatment of spin-orbit coupling is considered within the calculation, and (c) whether the treatment of magnetic interactions is included. Larger numbers, as included in Table 4.2 do not necessarily correspond to the higher computational difficulty (see Fig.4.17, for example). Difficulty 1 (D1) workflows are GGA calculations with default set of pseudopotentials, as

Material category	Symbol	Count	N_{at}^{min}	N_{at}^{max}
Elemental	EL	10	2	12
III-V	35	10	2	4
II-VI	26	11	2	4
Binary oxides	BO	15	2	12
Ternary oxides	TO	10	5	32
Dichalcogenides	DC	5	3	6
Alloys	AL	10	2	8

Table 4.1: Summary of the material categorization employed in this work with counts. N_{at} - number of sites (atoms) in the crystal unit cell.

implemented in VASP 5.4.4[92]. In terms of theory, the even difficulty numbers, (eg. 2) workflows are similar to the nearest odd (eg. 1), except for the inclusion of semi-core states in the pseudopotential for the following elements: Ga, Ge, In, Sn, Ti, Pb, Bi, Li, Na, Ca, K, Rb, Sr, Cs, Ba. Readers may consult the data online for further detailed information about the types of semi-core states included[3]. We prioritize the most comprehensive set whenever available, such that if a pseudopotential with only p and both p and s states are present, we use the latter.

The difficulty 3 and 4 workflows incorporate spin-orbit coupling (SOC). We treated all materials that contain elements with atomic number Z $>$ 45 (Rh) as the ones that require spin-orbit coupling to be included in the calculations. This is, notably, a somewhat "loose" approach, as there exists a well known spin-orbit splitting effect for GaAs, for example[156]. We argue, however, that since the latter effect is of the order of 100 meV it would not

be critical to the results of this study. This statement is further supported by the band gap value for GaAs found in this work. For the difficulty levels 5 and 6 we incorporate collinear magnetism as follows: we switch on the magnetic interactions and set the initial magnetic moments to a pre-defined value for all ferromagnetic atoms (V, Cr, Mn, Fe, Co, Ni). When more than one atom is present in the unit cell, we alternate the signs for the magnetic moment effectively creating an anti-ferromagnetic arrangement in this case. Lastly, the difficulty 7 workflows have all three, and, due to the nature of the computational implementation, resolve the non-collinear magnetic interactions.

Difficulty level	Semi-core	SOC	Magnetism	materials
1	no	no	no	23
2	yes	no	no	16
3	no	yes	no	8
4	yes	yes	no	9
5	no	no	yes	4
6	no	no	yes	5
7	yes	yes	yes	6

Table 4.2: Summary of the simulation workflows categorization employed in this work. "Semi-core" indicates that the pseudopotentials with semi-core states were used, "SOC" stands for the inclusion of the spin-orbit coupling, and "Magnetism" is used to denote the inclusion of collinear magnetic moments, except for the difficulty 7 when spin-orbit coupling and magnetism are included both, which lead to the treatment of non-collinear magnetic interactions.

4.2.4 Computational setup

Software/Theory

All Density Functional Theory[95, 90] calculations were performed within the pseudopotential projector augmented wave (PAW)[23] formalism using the Vienna Ab initio Simulation Package (VASP)[92, 55]. Within the generalized gradient approximation the exchange-correlation effects were modeled using the Perdew-Berke-Ernzerhof (PBE)[128] functional. All calculations were performed with the largest default plane wave cutoff energy of the pseudopotentials involved. The energies of all calculations were converged to within 10^{-4} eV. The Gaussian method was chosen as the smearing algorithm, the blocked Davidson iteration scheme[79] was chosen as the electron minimization algorithm, and ions were updated using the conjugated gradient algorithm. A smearing value of 50 meV was chosen for all the calculations. The semi-empirical Grimme-D2 correction to the Kohn-Sham energies were incorporated in all of our calculations[50]. The Heyd-Scuseria-Ernzerhof (HSE) calculations incorporate a 25% short-range Hartree-Fock exchange[60]. The screening parameter μ is set to 0.2 Å^{-1}. GW calculations were performed at the non-self-consistent G_0W_0 level. The number of unoccupied bands for the band gap calculation step was set to the total number of plane waves in the SCF step.

We implemented sampling in the reciprocal cell based on k-points per reciprocal atom (KPPRA) with a uniform unshifted grid. In our calculations, KPPRA of 2,000 were used unless specified otherwise. The density of states (DOS) calculations were performed within a denser grid with KPPRA of 16,000 using tetrahedron interpolation as implemented in VASP[92]. We ran most of the calculations within a single compute node described in the

next subsection. For some G_0W_0 calculations in particular, the memory requirements were larger than the resources available on a single node, however and efficient parallelization scheme for memory distribution is yet to be implemented for GW calculations in VASP at the moment of this writing. To accommodate the calculations within the available memory, we reduced the precision in a controlled way as follows: we limited the number of bands to 1000 at most, instead of using all available, then we reduced the KPPRA value to reduce memory requirements. The details about the cases with reduced precision are summarized in the footnotes of Table4.3.

Hardware

All calculations were performed using the hardware available from Microsoft Azure cloud computing service[1]. We utilized the "H16r" and "H16mr" instances specifically designed to handle high performance computing workloads. The instances are based on the Intel Xeon E5-2667 v3 Haswell 3.2 GHz (3.6 GHz with turbo) with 16 cores per node, and 112 and 224 GB of memory respectively. The instances carry a low latency, high-throughput network interface optimized and tuned for remote direct memory access. Computational resources were provisioned and assembled on-demand by software implemented and available within the Exabyte platform[5]. Most of the calculations were executed within a two-week period with a few requiring further work beyond that time frame. The peak size of the computational infrastructure used during this work was administratively limited to 125 nodes or 2000 total computing cores.

4.2.5 Data extraction

The relevant data for each workflow unit is extracted from the calculation output, parsed and stored in the database in the JSON format according to EDC. For instance, the forces on each atom after the volume relaxation are extracted and shown in the results page for each material. The band structure and the density of states (DOS) are also extracted from the band structure and density of states calculations, respectively. Thus, results for each material can be viewed online on Exabyte platform [3]. The platform also support a programmatic way of extraction of the data associated with materials and simulations through a RESTful application programming interface[4], partly used in this work as well.

4.2.6 Repeatability

The materials, workflows, batch jobs for each material with the associated properties, and files for each step of the simulation workflows are all made readily available online[3]. The Exabyte platform now contains all materials and workflows mentioned in this work, so readers may create an account, copy one or more materials to their account collection, copy a workflow similarly, and use the simulations designer as mentioned in Fig. 4.1 to recreate the simulation for this material. Furthermore, users can introduce modifications to our workflow and further improve the results.

Formula	Diff.	Calculated			Experiments			Band gaps (eV)						References			
		a	b	c	a	b	c	GGA	HSE	G_0W_0	HSE′	G_0W_0'	Expt.	Lat.	Gap	HSE′	G_0W_0'
Elemental																	
Si	1	3.75	3.75	3.75	3.82	3.82	3.82	0.56	1.14	1.09	1.28	1.12	1.17	[78]	[87]	[59]	[147]
Ge	2	3.98	3.98	3.98	4.00	4.00	4.00	0.16	0.86	0.84	0.56	0.66	0.75	[112]		[59]	[166]
Te	3	4.32	4.32	6.02	4.45	4.45	4.45	0.00	0.42	0.00	0.32	-	0.32	[82]	[11]	[180]	
B	1	4.85	4.85	5.00	5.06	5.06	5.06	1.20	1.70	1.58	-	-	1.49	[39]	[112]		
Bi	4	4.50	4.50	4.50	4.54	4.54	4.54	0.06	0.00	0.00	-	-	0.00	[37]	[112]		
P	1	3.33	4.37	5.45	3.31	5.92	4.38	0.14	0.14	0.16	0.39	0.30	0.35	[27]	[13]	[48]	[162]
As	1	3.79	3.79	3.99	3.65	3.65	4.47	0.03	0.29	0.15	0.00	-	0.30	[150]	[112]	[81]	
Sb	3	4.31	4.31	4.46	4.30	4.30	4.30	0.00	0.00	0.00	-	-	0.00	[16]	[112]		
Se	1	4.21	4.21	5.10	4.37	4.37	4.96	0.64	1.34	1.38	-	-	1.85	[82]	[112]		
grey-Sn	3	4.59	4.59	4.59	4.57	4.57	4.57	0.00	0.00	0.00	0.00	-	0.00	[28]	[112]	[66]	
III-V semiconductors																	
BN	1	2.50	2.50	6.61	2.50	2.50	6.66	3.15	4.20	4.32	5.98	5.4	5.95	[22]	[32]	[59]	[161]
BP	1	3.19	3.19	3.19	3.20	3.20	3.20	1.21	1.93	1.95	2.16	-	2.1	[112]	[112]	[59]	
GaP	2	3.82	3.82	3.82	3.85	3.85	3.85	1.56	2.25	2.22	2.47	2.48	2.35	[112]	[112]	[59]	[101]
BAs	1	3.36	3.36	5.57	3.37	3.37	3.37	1.12	1.77	1.73	1.92	1.93	-	[117]		[59]	[101]
BSb	3	3.71	3.71	3.71	3.62	3.62	3.62	0.64	1.16	1.04	1.37	1.28	-	[112]		[59]	[101]
AlN	1	3.10	3.10	4.98	3.11	3.11	4.97	4.29	5.69	6.03	6.45	5.83	6.19	[112]	[112]	[59]	[166]
AlAs	1	3.99	3.99	3.99	3.96	3.96	3.96	1.42	2.08	2.09	2.24	2.59	2.23	[112]	[112]	[59]	[101]
GaAs	2	3.98	3.98	3.98	4.00	4.00	4.00	0.63	1.52	1.74	1.21	1.30	1.51	[112]	[112]	[59]	[166]
GaN	4	3.19	3.19	3.19	3.20	3.20	3.20	1.71	2.98	2.98	3.03	2.80	3.17	[131]	[112]	[59]	[166]
YN	1	3.43	3.43	3.43	3.44	3.44	3.44	0.16	1.04	0.75	-	0.97	-	[141]			[141]
II-VI semiconductors																	
ZnS	1	3.79	3.79	3.79	3.82	3.82	3.82	2.22	3.48	3.51	3.42	3.29	3.54	[112]	[112]	[59]	[166]
BeS	1	3.42	3.42	3.42	3.44	3.44	3.44	3.1	4.05	4.47	4.14	4.92	5.5	[112]	[112]	[99]	[101]
BeSe	1	3.64	3.64	3.64	3.64	3.64	3.64	2.62	3.49	3.81	3.54	4.19	4.00	[112]	[112]	[99]	[101]
BeTe	3	3.98	3.98	3.98	3.98	3.98	3.98	1.67	2.34	2.65	2.68	3.17	2.80	[112]	[112]	[99]	[101]
MgS	1	3.65	3.65	3.65	3.67	3.67	3.67	2.84	3.84	4.46	4.78	4.044	4.50		[112]	[59]	[121]
BaSe	4	4.49	4.49	4.49	4.66	4.66	4.66	1.48	2.21	3.09	2.87	2.99	3.60	[51]	[112]	[59]	[121]
BaTe	4	4.90	4.90	4.90	4.95	4.95	4.95	1.18	1.82	2.56	2.50	2.33	3.40	[52]	[112]	[59]	[121]
CaSe	2	4.13	4.13	4.13	4.18	4.18	4.18	1.93	2.64	3.5	3.02	3.94	-	[109]		[59]	
Na_2S	2	4.56	4.56	4.56	4.62	4.62	4.62	2.63	3.71	4.67	-	4.77	5.00	[187]			
MgSe	1	4.20	4.20	6.80	4.15	4.15	6.72	2.71	3.71	4.26	2.62	4.58	4.05	[119]	[112]	[59]	
MgTe	3	4.56	4.56	7.41	4.53	4.53	7.40	2.26	3.00	3.54	3.74	4.19	3.49	[112]	[112]	[59]	[101]
Dichalcogenides																	
MoS_2	1	3.17	3.17	12.37	3.16	1.16	12.29	0.95	1.45	1.37	1.06	1.28	1.29	[25]		[175]	[34]
$HfSe_2$	3	3.71	3.71	6.04	3.67	3.67	6.00	0.07	0.63	0.77	1.07	1.08	1.10	[61]		[59]	[9]
TiS_2	2	3.36	3.36	6.62	3.41	3.41	5.69	0.00	0.38	0.09	0.40	-	0.30	[177]		[155]	
CrS_2	5	3.04	3.04	6.77		-		0.00	0.00	0.34	-	-	-				
MnS_2	5	3.28	3.28	6.57		-		0.00	0.00	0.00	-	-	0.00		[40]		

Table 4.3: Data for materials studied in this work. "Diff." - difficulty level. "Calc." and "Expt." have lattice constants of the relaxed structure and the experimental values, respectively. Lattice constants of the primitive unit cell are given, unless otherwise noted. A linear relationship between the two materials is assumed to determine the experimental lattice constant for alloys. The HSE and G_0W_0 values are compared with references when available.

Formula	Diff.	Calculated			Experiment			Band gaps (eV)							References		
		a	b	c	a	b	c	GGA	HSE	G_0W_0	HSE′	G_0W_0'	Expt.	Lat.	Gap	HSE′	G_0W_0'
Binary oxides																	
Li_2O	2	3.15	3.15	3.15		-		5.18	6.85	8.07	-	8.10	8.00		[71]		[152]
MgO	1	2.95	2.95	2.95	2.98	2.98	2.98	5.05	6.89	8.01	6.50	7.25	7.67	[163]	[112]	[59]	
BeO	1	2.68	2.68	2.68	2.70	2.70	2.70	6.92	8.71	9.62	10.09	10.29	10.59	[112]	[112]	[145]	
B_2O_3	1	4.12	4.49	4.49	4.13	4.61	4.61	9.97	11.00	12.04	-	-	-	[132]			
SnO_2	4	3.23	4.74	4.75	3.19	4.74	4.74	1.00	2.84	2.74	3.50	2.88	3.60	[115]	[112]	[75]	[19]
Al_2O_3	1	4.75	4.75	5.11	4.76	4.76	4.76	6.28	8.22	9.29	8.82	-	8.80	[43]	[137]	[75]	
α-SiO_2	1	4.84	4.84	4.97	4.96	4.96	4.96	6.07	8.12	9.48	8.72	10.10	9.30	[130]	[174]	[168]	[94]
BaO_2	4	3.72	3.72	4.15	3.78	3.78	4.30	2.02	3.60	3.73	-	-	4.29	[21]	[134]		
NaO_3	2	3.17	4.21	4.21	2.94	4.12	4.12	0.00	0.00	0.00	-	-	-	[88]			
VO_2	5	2.80	4.52	4.52	2.85	4.55	4.55	0.00	0.18	0.00	-	-	-	[97]			
TiO_2	2	12.19	3.72	6.55	12.16	3.74	6.51	2.78	4.28	4.66	3.13	3.10	-	[15]		[75]	[20]
NiO	5	2.93	2.93	2.93	2.95	2.95	2.95	0.00	2.98	4.07	4.10	3.60	4.30	[142]		[47]	[160]
CaO	2	3.94	3.94	4.73		-		3.30	4.72	4.97	4.23	4.40	6.93		[112]	[136]	[136]
ZnO-cub	1	3.04	3.04	3.04	3.02	3.02	3.02	0.83	2.42	2.42	2.49	2.12	3.44	[17]	[112]	[59]	
SrO	2	3.60	3.60	3.60	3.64	3.64	3.64	3.25	4.75	5.10	4.70	5.57	5.22	[133]	[112]	[14]	
Ternary oxides																	
NdClO	3	3.85	3.85	6.77	4.03	4.03	6.76	0.00	0.00	0.00	-	-	-	[182]			
$SmNiO_3$	7	5.31	5.33	7.41	5.33	5.44	7.57	0.00	0.00	0.00	-	-	-	[98]			
$NaOsO_3$	4	5.25	5.25	5.25		-		0.00	1.34	0.12	-	-	-				
$GdTiO_3$	4	5.38	5.46	7.60	5.41	5.67	7.69	0.00	0.00	0.00	-	-	-	[116]			
$SrTiO_3$	2	5.50	5.50	5.51	5.51	5.51	5.51	1.94	3.24	2.90	3.20	3.57	3.25	[76, 108]	[165]		
$LaCoO_3$	7	5.30	5.30	5.30	5.34	5.34	5.34	0.00	2.52	0.24	2.52	-	0.60	[158]	[33]	[184]	
$LaNiO_3$	7	5.32	5.32	5.32	5.45	5.45	5.45	0.00	0.00	0.00	-	-	0.0001	[46]	[138]		
$LaMnO_3$	7	3.84	3.84	3.84	3.88	3.88	3.88	0.00	0.00	0.00	-	-	-	[164]			
$GdMn_2O_5$	7	5.63	7.23	8.5	5.68	7.35	8.54	0.62	2.29	2.27	-	-	-	[80]			
$GdCoO_3$	7	3.72	3.72	3.74	3.80	3.80	3.80	0.00	0.00	0.00	-	-	-	[31]			
Semiconductor Alloys																	
SiGe	2	3.84	3.84	6.33	3.85	3.85	3.85	0.36	0.78	0.94	-	-	0.91	[42]			
SiSn	6	4.15	4.15	4.15	4.21	4.21	4.21	0.49	0.95	1.00	-	-	1.11	[153]	[67]		
AlGaAs	2	5.59	5.59	5.59	5.66	5.66	5.66	1.21	1.95	2.20	-	-	2.02	[10]	[10]		
InGaAs	6	5.84	5.84	5.85	5.84	5.84	5.84	0.00	0.82	1.19	-	-	0.77	[10]	[10]		
InGaP	6	5.60	5.60	5.65	5.66	5.66	5.66	1.10	1.95	1.89	-	-	1.90				
AlInAs	6	5.79	5.79	5.80	5.86	5.86	5.86	0.97	1.86	2.16	-	-	1.50				
AlInSb	6	6.19	6.19	6.21	6.30	6.30	6.30	0.78	1.31	1.35	-	-	1.13				
GaAsP	2	5.51	5.51	5.51	5.55	5.55	5.55	1.20	1.77	1.96	-	-	2.03				
GaAsSb	4	5.84	5.84	5.83	5.87	5.87	5.87	0.08	0.53	0.54	-	-	0.72				
AlGaN	2	4.46	4.46	4.46	4.45	4.45	4.45	2.36	3.66	3.83	-	-	4.60				

Table 4.4: Table 4.3 continued.

4.3 Results

Fig. 4.4 shows a comparison of the calculated band gaps within GGA, HSE and G_0W_0 with their experimental values for all the materials where the experimental data is available. We also include the results of Materials Project[74] (further referred to as MP) calculated within GGA (or GGA+U approach when specifically noted) for reference. As expected, in can be seen that the GGA underestimates the band gaps, and HSE and G_0W_0 both significantly improve the results. A linear regression model fit to the three different levels of theory is shown in Fig.4.5. From the figure it can be seen that when a simple linear fit $y = kx + b$ to the data is used, the resulting values for the model-wise errors based on the coefficient of proportionality k are as follows: GGA - 35%, HSE - 17%, G_0W_0 - 7%.

4.3.1 Elements

Fig. 4.6 shows band gaps of elemental materials compared with experimental values. The gap for Te was measured to be 0.3 eV in [12], however our GGA band structure does not have a gap. The lattice parameter a of our relaxed structure is underestimated by 2.23%. MP-GGA value is 0.186 eV, however in their case the lattice parameter is overestimated by 1.37% [82]. The reduction in lattice parameter in our case can be attributed to the vdW correction. In another study the meta-GGA-SCAN functional is seen to predict

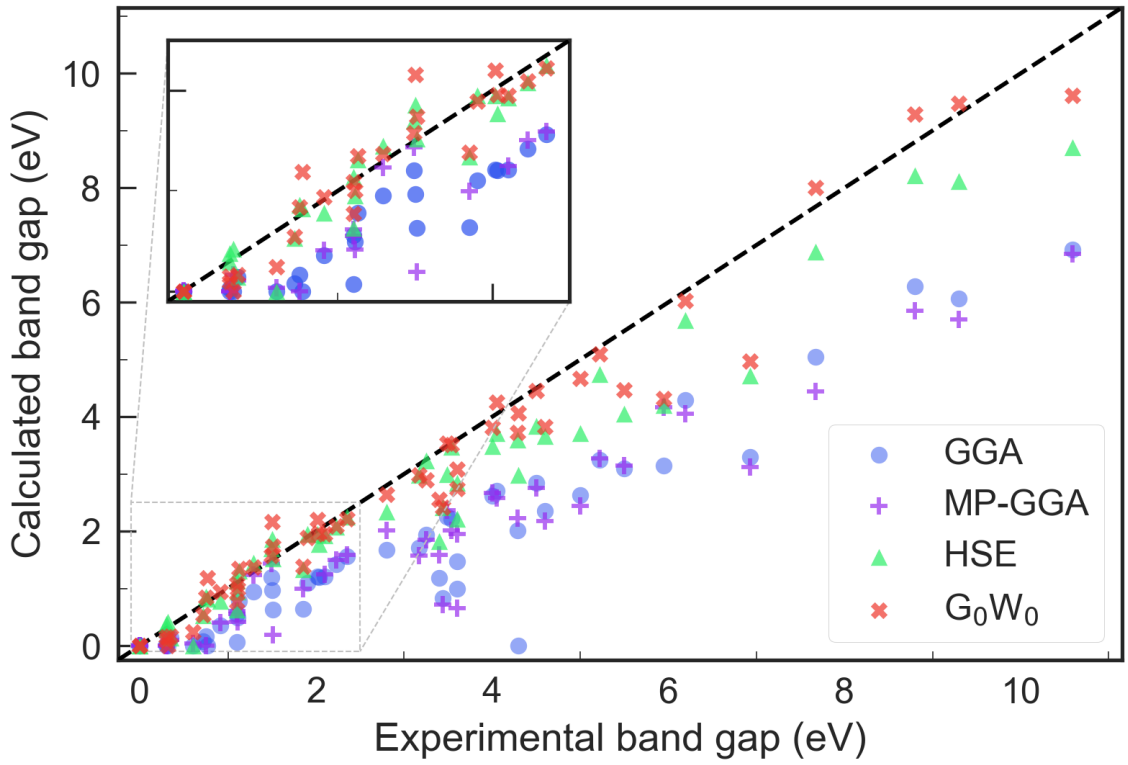

Figure 4.4: Comparative plot of the calculated and experimentally available values for all the electronic band gaps obtained in the current work. Legend: GGA, HSE, and G_0W_0 denote the results of this work for the corresponding level of theory. MP-GGA denote the results of Materials Project[74] available at the moment of this writing.

the lattice parameters well [181], however the calculated HSE band gap is larger than the experimental value by 40%. An exact-exchange mixing parameter of 0.125 was needed to reproduce the correct experimental gap for Te in [181]. Our G_0W_0 calculation predicts Te to be metallic.

Ge has the experimental band gap of 0.75 eV[112]. We find the lattice parameter of the relaxed configuration within 0.5% of the experimental value[112]. Both HSE and G_0W_0 overestimate the band gap by 16.21% and 13.51% correspondingly. While MP predicts Ge

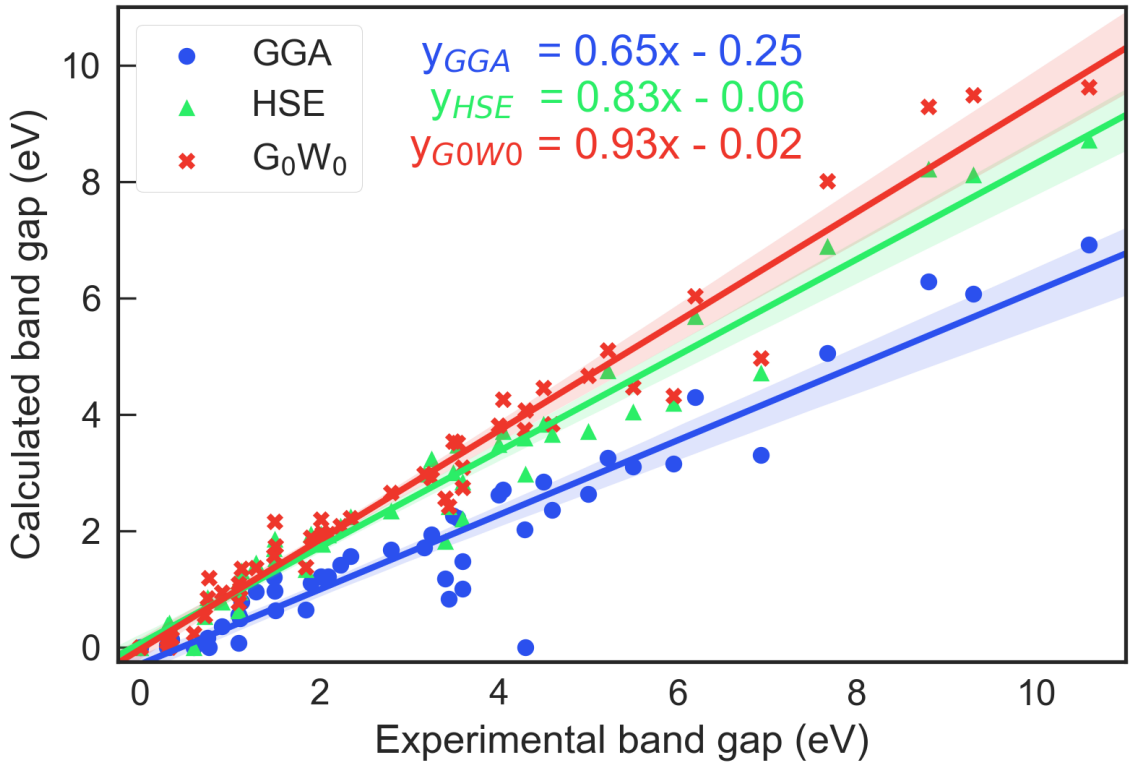

Figure 4.5: Comparative plot for all the band gaps calculated in the current work, including the linear $y = kx + b$ fits to data per each model. The legend is same as in Fig.4.4. The equations for each of the linear fits are shown in the figure.

to be metallic, our calculation predicts a band gap of 0.16 eV within the GGA. We attribute this to the inclusion of semi-core states in our case.

For Si, the GGA band gap is underestimated by 48.7%. Both HSE and G_0W_0 predict band gap of Si very well: within 3.6% and 0.9% correspondingly.

For boron, our GGA band gap is 19.5% less compared to the experimental value[112]. The MP GGA band gap for boron is underestimated by 4%. We attribute this difference to the inclusion of vdW correction in our case. Our lattice parameter a is about 4% smaller compared to that of MP which results in smaller band gap. Similar trend is observed for Se where our lattice parameter is underestimated by 7%.

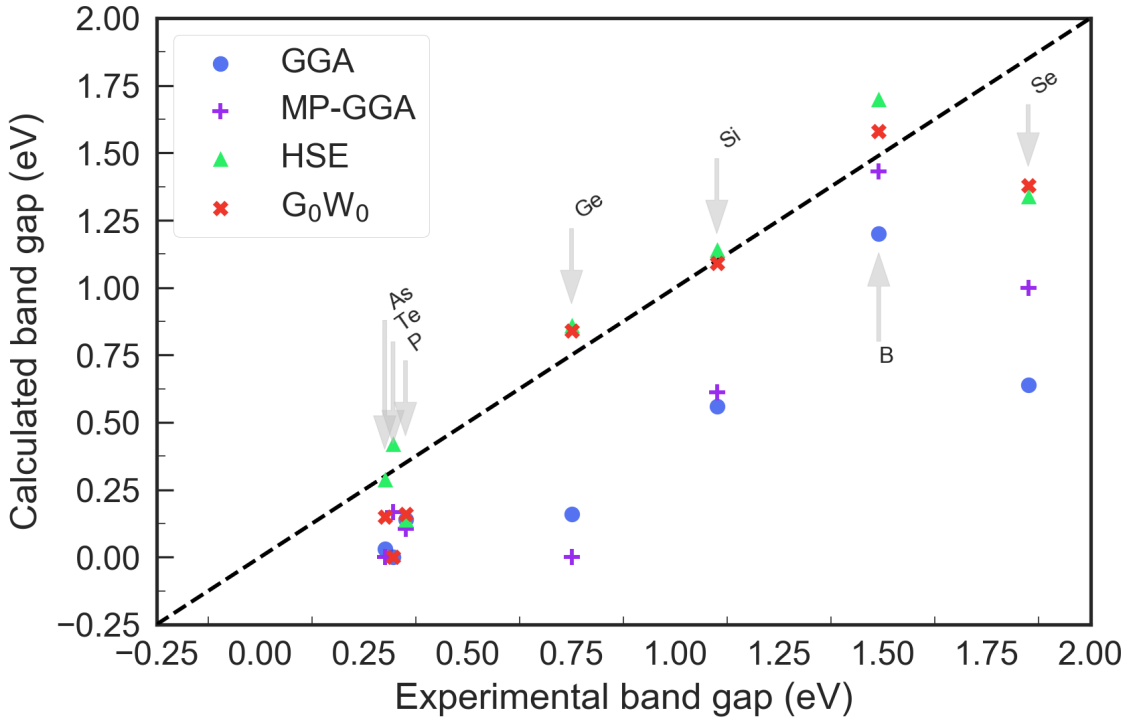

Figure 4.6: Comparative plot of the calculated and experimentally available values for all the electronic band gaps in the elemental (EL) category.

For other materials in this category - P, As and Se we find G_0W_0 to underestimate the gaps by 54%, 50% and 25.5%, respectively. Incorporating partially self-consistent GW_0 corrects the errors to 11.1%, 21% and 10.23%, respectively. Due to the small value of the gaps for P and As, the Gaussian smearing used during the calculation (50meV) can contribute to the error significantly.

4.3.2 III-V semiconductors

Fig. 4.8 has the band gaps for category 35. For BP, AlAs, GaP, GaN and AlN, HSE and G_0W_0 predicts band gap within 8.1% and 7% accuracy, respectively. For GaAs, HSE predicts the band gap within 0.4%. The G_0W_0 overestimates the band gap by 15.4%,

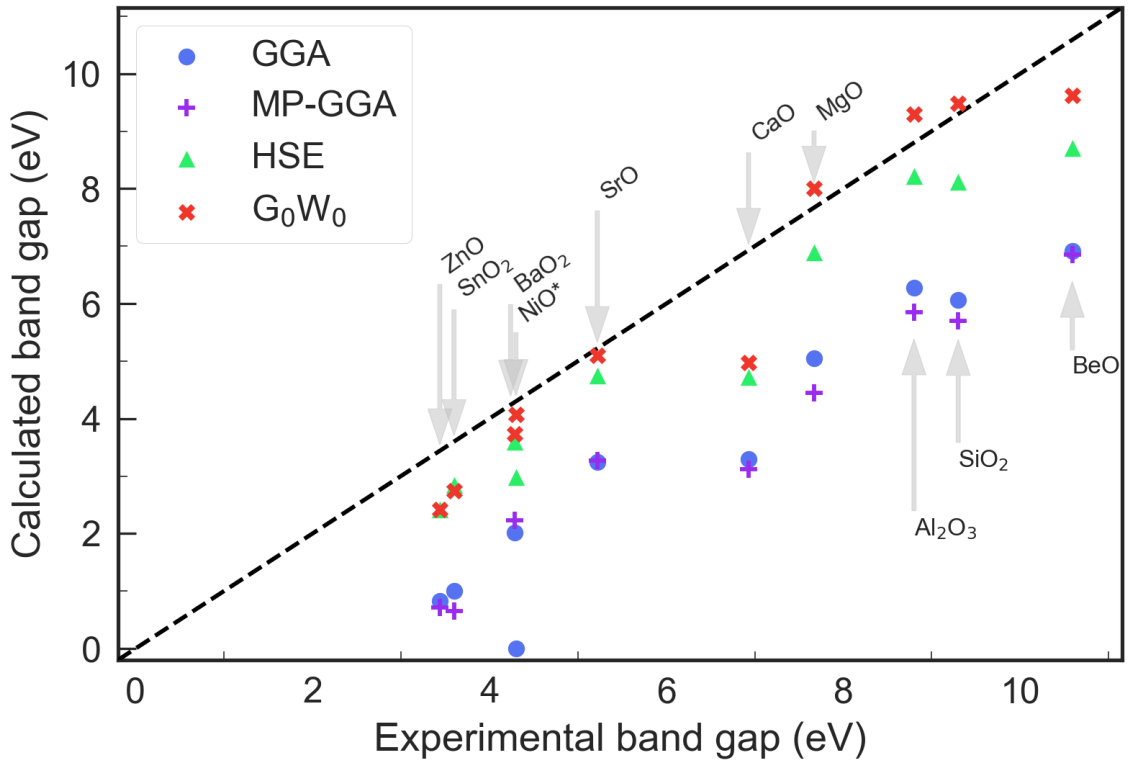

Figure 4.7: Same as Fig. 4.6 for the binary oxides (BO).

which might be due to the fact that the band gap estimate is performed on a grid as explained in sections 4.2 and 4.4. Among the materials considered, BN has smaller GGA band gap compared to MP. Inclusion of vdW in our case reduces the lattice parameter by 2.4% which reduces the GGA band gap.

Our GGA band gap of BN is 26.3% smaller compared to MP value. Also the MP GGA band gap predicts the band gap within 1.7% of HSE band gap of BN. This is due to the absence of vdW interaction within the BN layers in MP calculations. While the lattice parameter a of MP GGA matches within 0.8% [151], lattice parameter c is overestimated by 23% which in turn causes the larger gap value that is close to experiment. We also find

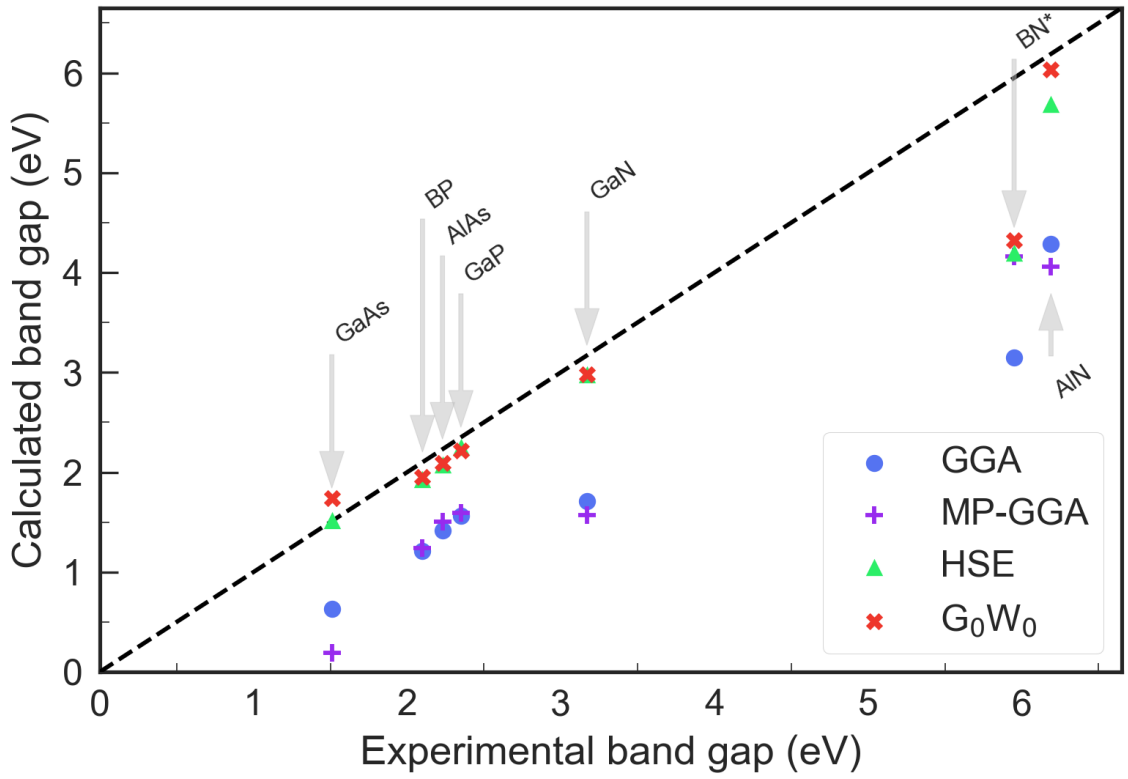

Figure 4.8: Same as Fig. 4.6 for the III-V compounds (35).

that within G_0W_0, the band gap has an error of 27.5%. We employed self-consistent GW calculation to improve the band gap, and find that 4 iterations reduce the band gap error to 11.8%.

4.3.3 II-VI

Fig. 4.10 shows the band gaps for category 26. The bonding nature of the materials in this category is ionic and covalent. As a result, the inclusion of vdW interaction does not affect the lattice parameters much, except for BaSe and BaTe. Due to the inclusion of vdW interaction, our lattice parameters are smaller compared to MP results and hence the gaps

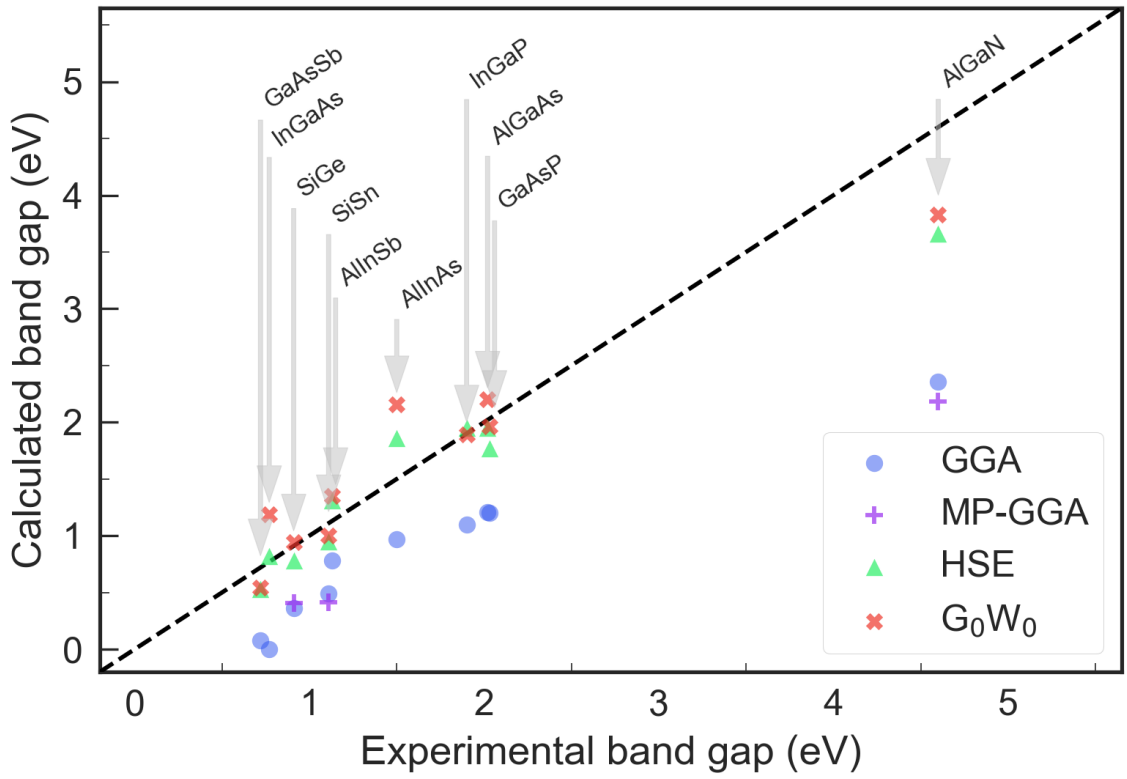

Figure 4.9: Same as Fig. 4.6 for the semiconductor alloys (AL).

are smaller as well. Our HSE band gap of MgS is underestimated by 19.67% compared to [59]. We attribute this difference to the smaller lattice constant due to vdW correction in our case.

4.3.4 Dichalcogenides

Fig. 4.11 has the results for category DC. All the materials within this category are layered two-dimensional structures. For these materials, the inclusion of vdW interaction is critical to get the lattice parameter c correctly. For $HfSe_2$ and MoS_2, our calculated c value is within 1.65%[49] and 0.8%[26] of the experimental value. The MP relaxed structures

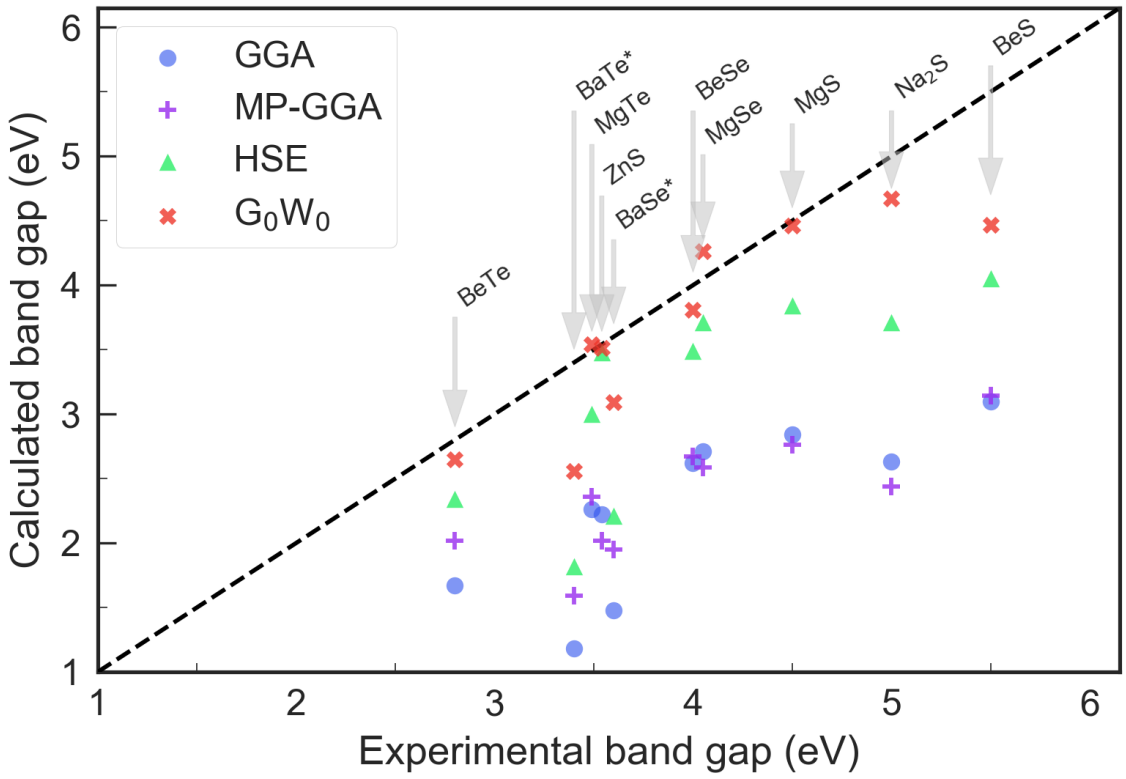

Figure 4.10: Same as Fig. 4.6 for the II-VI compounds (26).

overestimate the values by 21% and 12.7%, respectively. Within GGA, TiS_2 is predicted not to have a band gap, while the HSE and G_0W_0 calculations open it. HSE overestimates the gap by 27.7%.

4.3.5 Binary Oxides

Fig. 4.11 has results for binary oxides. Within this category MP GGA band gaps match closely with our values, except in the case of NiO. While the MP has a gap of 2.498 eV, our calculation predicts material to be metallic. This discrepancy is due to the use Hubbard correction by MP, since a U value of 6.2 eV was employed there. Our HSE and

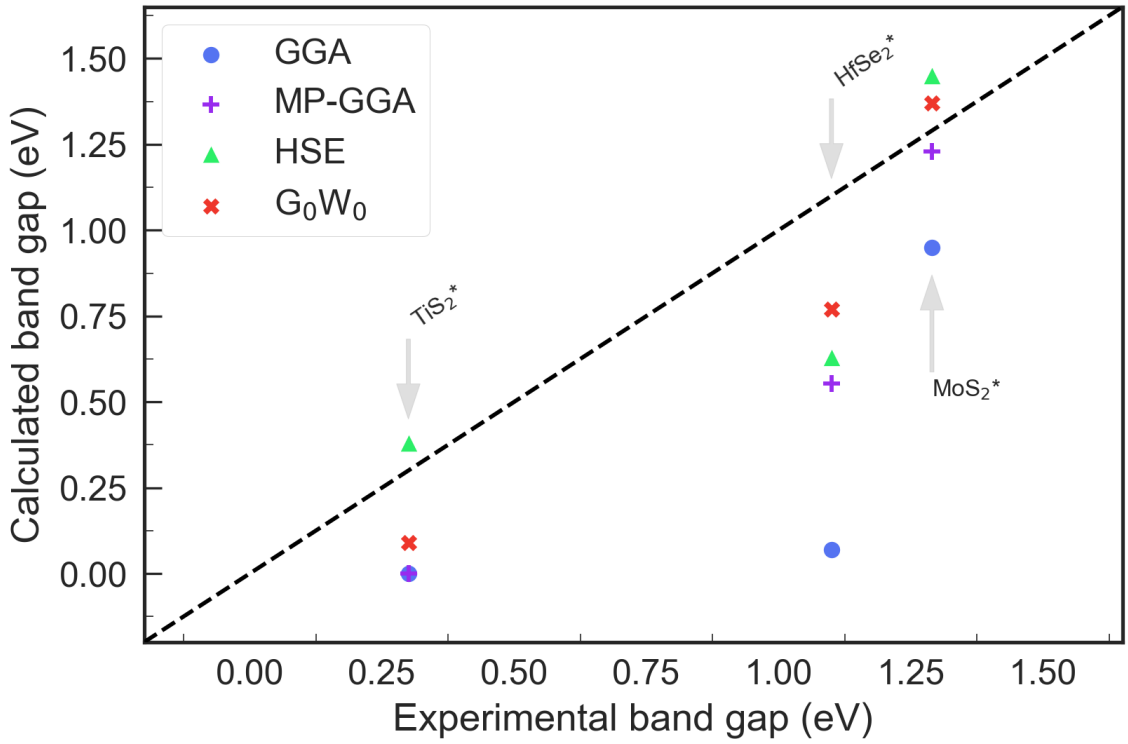

Figure 4.11: Same as Fig. 4.6 for the dichalcogeniges (DC).

G_0W_0 calculations predict the band gaps within 30% and 5.4% of the experimental value, respectively. Further improvement can be obtained using the self-consistent GW approach as demonstrated in Table. 4.5.

4.3.6 Ternary oxides

The calculated band gaps for materials in category TO is compared with experimental band gap in Fig. 4.12. Within this category the experimental band gaps are found only for $LaCoO_3$ and $SrTiO_3$, as shown in Table.4.3. For $LaCoO_3$, both GGA and HSE predict the material to be metallic. In G_0W_0 we get a gap of 0.24 eV for LaCoO3, however,

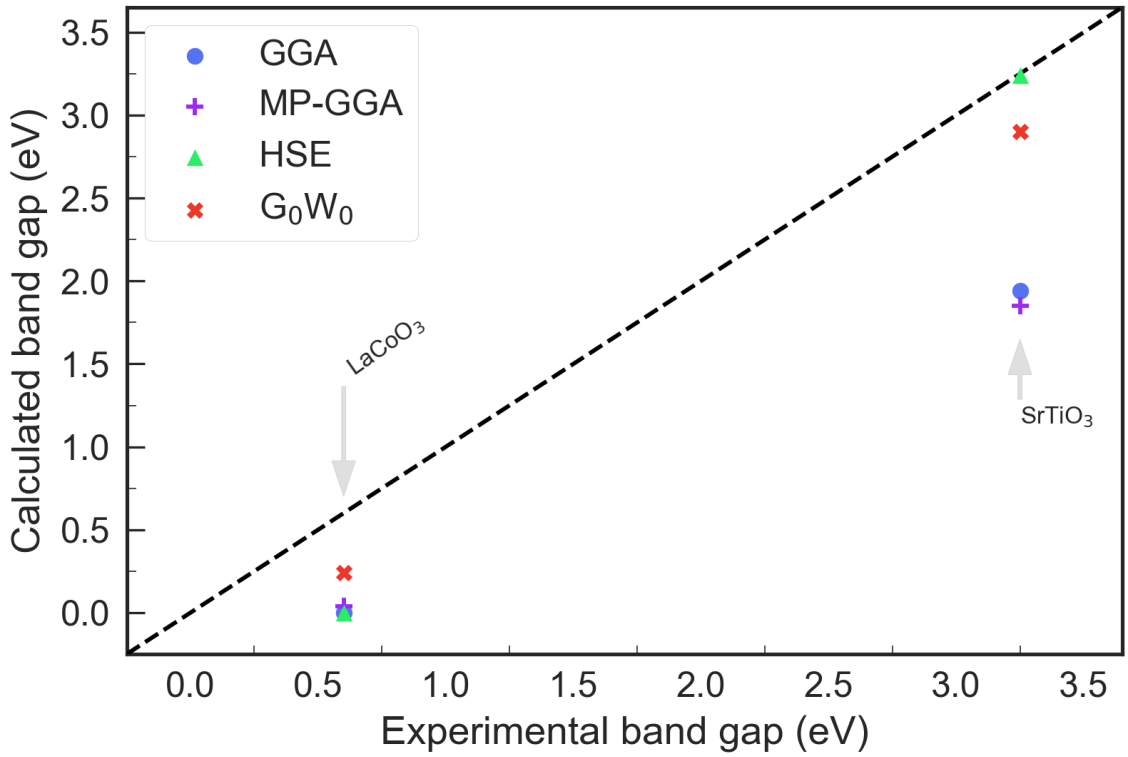

Figure 4.12: Same as Fig. 4.6 for the ternary oxides (TO)..

since we do not calculate the full band structure as explained in section 4.2, a further study might be required to confirm the result. For SrTiO3 HSE predicts the gap very well with a 0.4% error while G_0W_0 has an error of 10.7%.

4.3.7 Semiconductor alloys

Fig. 4.9 has results for AL category. InGaAs has no gap within GGA, while the HSE predicts the gap within 6.1% of the experimental band gap. The G_0W_0 calculation overestimates the band gap by 54.7%, we attribute this to the lack of the full band structure calculation and indirect nature of the gap. In the case of AlInAs G_0W_0 overestimates

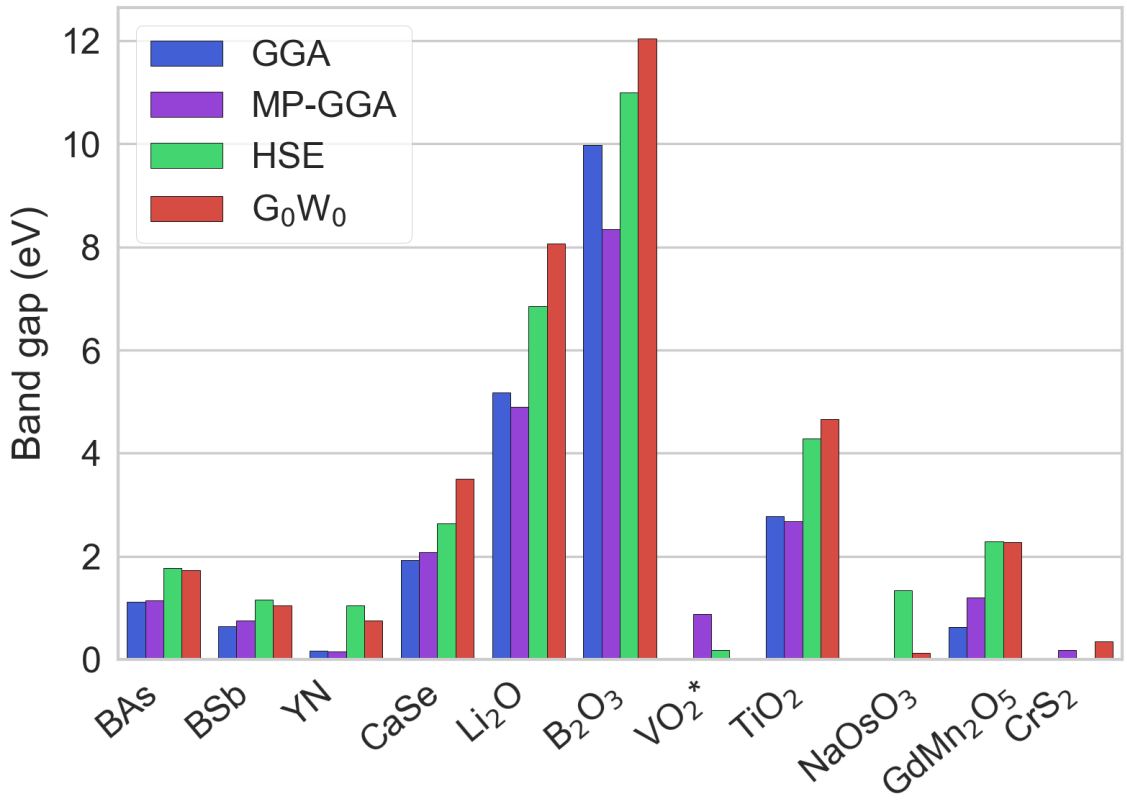

Figure 4.13: Calculated band gap values for different levels of theory for the materials without experimental data. The legend is same as in Fig.4.4 (color-wise). For materials with an asterisk sign, the MP band gaps are calculated using DFT+U.

the band gap by 43.9% for the same reason, while HSE has a 23.7% larger value than experimental.

4.3.8 Other materials

Materials for which experimental data is not found are plotted in Fig. 4.13. Our GGA band gap matches well with MP band gap. HSE and G_0W_0 improves the result. The

Material	G_0W_0	sc-GW		
	Gap (eV)	Gap (eV)	Iterations	Energy cut-off (eV)
P	0.16	0.39	4	330
As	0.15	0.24	4	250
Se	1.38	2.04	3	300
BN	4.32	5.02	4	520
NiO	4.07	5.30	4	415

Table 4.5: Band gaps calculated with partially self-consistent GW calculations. For all the calculations the self-energy of the non-diagonal components were included. The iteration of the quasi-particle (QP) energy shifts and the energy cut-off used are also tabulated.

band gap difference of B_2O_3 within GGA between our calculation and MP can be attributed to the vdW interaction included in our calculations. Due to the localization (DFT+U) effect included in MP, VO_2 is semiconducting while our calculation shows VO_2 as metallic.

Within GGA, $NaOsO_3$ is predicted to be metallic both by us and MP. HSE opens a band gap of 1.34 eV. G_0W_0 predicts a band gap of 0.12 eV. We believe that self-consistent GW may increase the band gap closer to the HSE value. All levels of theory predict $GdMn_2O_5$ to be semiconducting.

4.4 Discussion

We meant this study as a practical "end-to-end" benchmark of the ability of the current generation of pseudopotential density functional theory (DFT) to predict the electronic properties of materials. We also focused our attention on how it can be applied in an

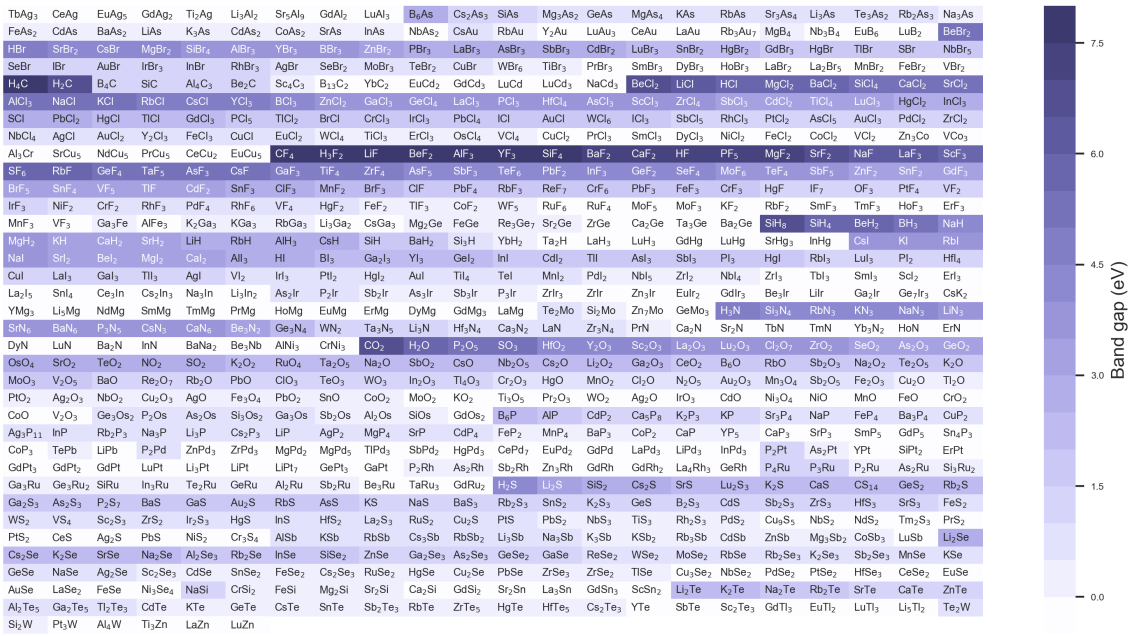

Figure 4.14: Heatmap plot for GGA band gap values calculated within GGA in this work. The formulas use same compounds order sorted by the second element in formula and the gap value starting from the top right corner.

accessible way with minimal additional computational setup (i.e. no specialized hardware or compilation routines). As it was recently demonstrated in a comprehensive overview of the DFT simulation engines in [104], most of them are inter-changeable with respect to the results delivered within the same model approximation. We selected VASP[92] as one of the most used tools in the space. Unlike the previous benchmarks, however, that considered computing aspects exclusively [120, 73], we went further and calculated the properties for a diverse set of material compounds.

4.4.1 Accessibility

The problem of accurate calculations of the electronic band gaps has been around for nearly as long as the computing itself. Although much effort was put into producing a

way to obtain reliable high fidelity results, an accessible and repeatable option is still largely missing[129, 6]. Our work is an attempt to demonstrate how a standardized approach to the creation and execution of the first-principles modeling workflows developed by Exabyte Inc. can resolve the above. We present an accessible, repeatable and cost-effective way to deploy first-principles modeling workflows. Furthermore, we make the data freely available on the web, and provide an intuitive way to reproduce our work. Recently there has been much attention to high-throughput first-principles calculations of materials properties, which lead to the proliferation of the online databases and the development of the associated software tools[74, 38, 129, 6, 139]. Our approach has similar capabilities, as demonstrated by this work, and is accessible to a larger community, in particular, to those without first-hand knowledge of DFT.

Another important recent advancement came from the data-centric approaches where large repositories of data can be used together with machine learning techniques in order to build predictive models[70, 171]. Such models are able to deliver the predictions much faster, as they do not require the solution of physical equations. Our data-centric platform can power the construction of such models, with the potential to achieve improved accuracy of predictions by basing them on more accurate DFT results. Others approached the problem from a more traditional perspective attempting to construct DFT functionals capable of delivering high accuracy for the calculations of the electronic band structures[36]. We will refrain here from discussing transferability from one material class to another for any such functional. Instead, we would like to point out that in practical applications the bottleneck that prevents the adoption of any of the aforementioned techniques is the human

time required to get a prediction with a certain expected level of precision. Surely, reliably delivering high-fidelity results quickly is the best, however, an approach that takes a long time to compute but little to set up and oversee can work just as well.

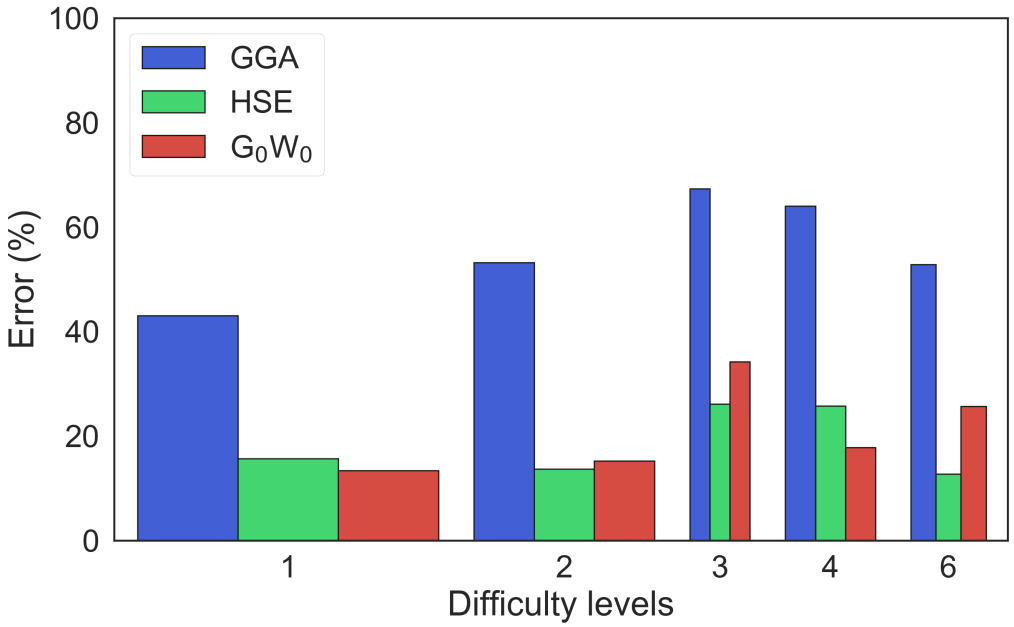

Figure 4.15: Difficulty-wise average errors. The width of the bars are proportional to the number of materials in category. Difficulty 5 and 7 is excluded due to low count (<3).

4.4.2 Fidelity and error analysis

When comparing with the available experimental data we point out some important conditions used within our approach that are known to affect the calculation results. Firstly, we conduct the structural relaxation within the GGA and subsequently use the resulting structure for HSE and GW calculations. GGA is largely believed to work well for the ground-state properties of materials, and thus little change is expected when the

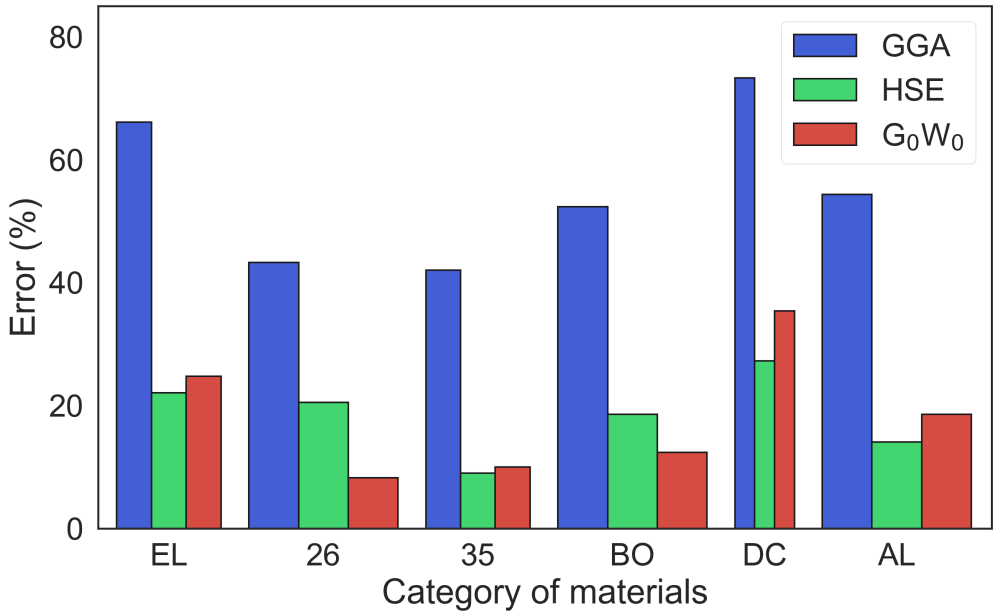

Figure 4.16: The average errors per each stoichiometric category. The width of the bars are proportional to the number of materials in category. Ternary oxides excluded due to low count (<3).

structures are relaxed with HSE, for example[59]. Secondly, in order to improve the treatment of van-der-Waals (vdW) interaction within our models we introduce a correction as implemented in VASP[57, 50]. This improves the results for layered materials especially, where the layered materials are considered. This is due to the fact that layered materials are self–passivated and the inter–layer interaction is dominated by the vdW interaction. Lastly, due to the computational complexity of the current implementation for G_0W_0 within VASP, we calculate the band gaps using the electronic eigenvalues on a grid of points inside the Brillouin zone, instead of using the standard path[38] as we did for GGA and HSE. The latter fact affects the fidelity of results for indirect gap semiconductors especially where the band extrema are located far from high symmetry points sampled by the grid. Due to con-

straints to the availability of memory, we reduced precision for few materials as indicated in Table 4.3. The reduced number of k-points within the irreducible Brillouin zone may have contributed to the error as well.

Figures 4.15 and 4.16 have the data about the average errors per material category. Width of each column are proportional to the number or materials in each difficulty or category. We have omitted categories and difficulties that have experimental band gap available for less than 3 materials. We find that the GGA calculations have the largest error. HSE and G_0W_0 improve the band gap by similar margin. Category D3 has the largest error, although, notably, the sampling per this category is substantially less than for D1 and D2, for example. The dichalcogenides (DC) produced the largest error by material type, although it also has to be noted that the sampling in this category is lowest. We attribute this to the applied vdW correction in the layered materials.

The lattice constants c of layered materials are sensitive to the type of vdW correction applied. Case specific vdW correction to the material can improve error in lattice constants and reduce the error. Even though HSE and G_0W_0 calculations improve the band gap for this category, we suspect correct inter–layer spacing can improve the band gaps further. We also find that for category EL, the G_0W_0 band gaps give larger error compared to HSE calculations. The self–consistent GW calculations improve the band gap for EL materials substantially (discussed in Sec. 4.4.3 in detail). Category 26 and 35 compounds had most accurate predictions within HSE and G_0W_0. Category TO materials are excluded from Fig. 4.16 due to low sample count.

4.4.3 Further improvements to accuracy

There exist multiple ways to further improve the accuracy of the results obtained in this work. For the GW calculations, the self-consistent GW approach can improve the results. Table 4.5 summarizes the band gaps calculated with self-consistent GW. We find the approach where the non-diagonal components of the self-energy are included to provide the best accuracy[148] within a manageable time frame. We believe that executing the self-consistent GW calculations in a high-throughput manner is already possible for the materials studied in this work. In practice, it would presently require using compute nodes with extra large memory. Although such nodes are readily available from public cloud providers, the current computational implementation in VASP is not optimized for this regime and thus we would expect the resulting calculations to be more expensive and less reliable.

Another way to improve the accuracy of the results would be to use a dynamically adjustable value for the HSE mixing parameter similar to how it is done in [149]. This approach would be more computationally intensive as it requires the convergence of the static dielectric constant with respect to the mixing parameter to be achieved during the calculation. Alternatively, a "hybrid" scheme could be considered where initially the improved value for the mixing parameter is calculated "on-the-fly" based on a statistical model, and then a "single-shot" HSE calculation is executed.

Lastly, the precision of the resulting calculations can be improved by addressing the concerns stated in the previous sub-section related to the sampling in the Brillouin zone. We used an approach based on the KPPRA, whereas introducing the logic for explicit

convergence into the resulting workflows could be beneficial. For G_0W_0 calculations in particular a more thorough approach to treating the convergence of the end results with respect to the size of the pseudopotential basis set might be beneficial. We assumed the default recommended value of the cutoff and used all available planewave states (bands) for the summation whenever possible. When memory concerns arised we reduced the fidelity in a controlled way as explained in the section 4.2.

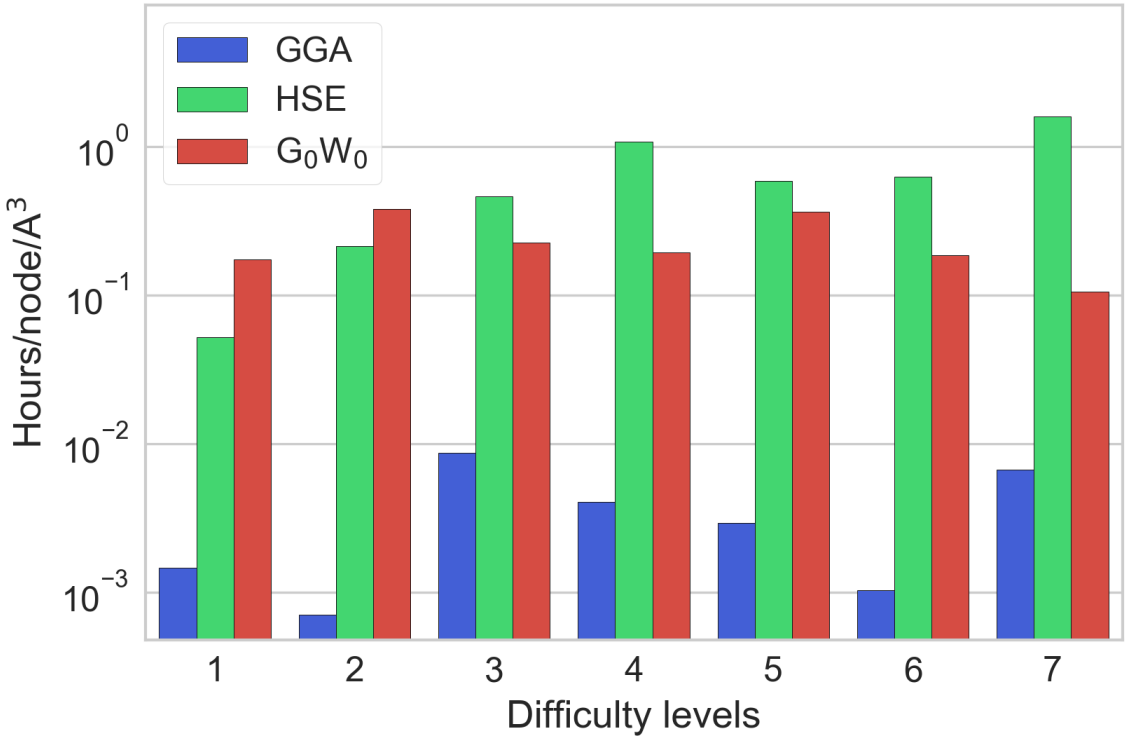

Figure 4.17: Calculation time per each difficulty level (as defined in section 4.2). The time is normalized per one compute node and unit cell volume (Å^3). The electronic band structures are calculated in full for GGA and HSE only.

Model	Avg. err, (%)	Avg. runtime	Cost ($)	Note
Exact	0	30 days	5,000	extrapolated
HSE	20	43 hrs	250	factual
GGA	54	18 min	5	factual
Zero	100	0.1 sec	0	extrapolated

Table 4.6: Average errors and the associated average calculation time for the HSE and GGA cases studied in this work. *Exact* and *Zero* values are constructed through a simple logarithmic fit of the HSE/GGA data for the (hypothetic) models that would produce exact and zero-fidelity results correspondingly.

4.4.4 Computational time and cost

In order to provide insights about the feasibility of further improved approaches and the ability to obtain the ultimate exact accuracy, we construct a simple logarithmic regression using the data obtained for the GGA and the HSE results. We exclude G0W0 because the results for it did not include the full band structure calculations, thus its set of computed properties is different. We assume that the average simulation lifetime increases exponentially as the average error is dropping. This is, of course, an overly simplified treatment and is only meant to produce qualitative results. We base our logic on the fact that the calculation of exchange interaction as employed within the HSE formalism includes the integral sums over the electronic states, and thus increasing the number of individual computations to the square of the number of wavefunctions. As can be seen from Table 4.4.3, within this logic one would need to run a simulation for about 30 days on average in order to produce an exact result. On the opposite side, a simulation with a runtime of less than 0.1 sec would fail to produce a meaningful result.

Our motivation for the above is to provide a metric of the extent to which the physics-based first-principles modeling can augment the trial-and-error experimental approach when compared with respect to the capital and time investments required. We suggest that for the equivalent of one month of calculation time (human time) on a commodity compute server readily available from a cloud provider it is possible to obtain results that are accurate well within 20% and potentially within 1-5% range for the properties that we study in the current work. There are, admittedly, many factors that can adversely affect the result and many ways to optimize and improve upon the setup we used. Nevertheless, it is clear that the high fidelity results are not prohibitively expensive already today, and with the advancements in computing technology will become more and more prevalent. Furthermore, when compared with the capital spends required to manufacture and prototype the materials in experiment, even the "Exact" scenario we considered above appears attractive. Moreover, when data-centric community efforts without repetition are taken into account, the costs are further amortized. We believe that the correct approach to materials development from nanoscale is to use both high-fidelity simulations and experiments in a collaborative "funnel"-like scenario similar to how the computer-aided design and engineering is applied at present.

4.4.5 Future outlook

We believe that the landscape of computational materials design is rapidly evolving toward a data-driven science where the modeling results are aggregated and classified by their precision/accuracy. We believe, however, that the major improvements in way computational materials science is used would be significantly delayed if possible at all

when only performed by means of the selected few. As the volume and variety of data available to community is growing at an accelerated speed, the veracity of this data also becomes increasingly important. The approach described in this work can solve both aforementioned concerns. The improved creative ideation with contributions from people with multiple backgrounds is enabled by modeling workflows accessible in a standardized and repeatable way and the shift away from the "medieval artisan-like" model[129] still prevalent nowadays. On the other hand, this work provides first proof that high precision is also achievable, perhaps only for electronic materials at this moment, using existing first-principles modeling techniques. We believe that a hybrid data-driven approach with roots in high-fidelity modeling is most powerful.

4.5 Conclusions

We report on the application of a novel approach to materials modeling from nanoscale implemented within the Exabyte platform[5] to a diverse representative set of 847 semiconducting materials (ESC-847). The approach makes high-fidelity techniques such as pseudopotential Density Functional Theory with Hybrid Screened Exchange (HSE) and G_0W_0 approximation available in an accessible, repeatable and data-centric manner. We introduce a categorization for the materials according to the level of approximation used and explain the implementation of the corresponding modeling workflows. We present the results for the electronic band gaps obtained within the Generalized Gradient Approximation (GGA), HSE and G_0W_0, analyze the level of fidelity for the prediction delivered by each of the models used, and discuss the corresponding computational costs.

We compare the results with experimental data and prior similar calculation attempts, when available. We find the average relative error to be within 20% for HSE and GW results and within 55% for GGA. We further find the average calculation time on a current up-to-date compute server centrally available from a public cloud provider to fit within 30 min and 48 hours respectively for GGA and HSE. For the first time ever we present not only the results and the associated data, but also an easy-to-access way to reproduce and extend the results by means of Exabyte platform.[3] Our work provides an accessible, repeatable, and extensible practical recipe for performing high-fidelity first-principles calculations in a high-throughput manner.

Bibliography

[1] *Microsoft Azure Cloud Computing platform: web page.*

[2] *Citrine Informatics: Materials Data Platform*, 2018.

[3] *Exabyte platform: project URL with data about simulations*, 2018.

[4] *Exabyte RESTful API client: online URL*, 2018.

[5] *Exabyte.io: materials discovery cloud*, 2018.

[6] *NOMAD laboratory: A European Centre of Excellence*, 2018.

[7] *Tilde Materials Informatics*, 2018.

[8] Dimoulas A. Negative momentum relaxation rate and transport in polar semiconductors. *Physica Status Solidi (b)*, 137(1):319–329, 1986.

[9] Mahmud Abdulsalam and Daniel P Joubert. Optical spectrum and excitons in bulk and monolayer mx2 (m= zr, hf; x= s, se). *physica status solidi (b)*, 253(4):705–711, 2016.

[10] Giovanni Agostini and Carlo Lamberti. *Characterization of semiconductor heterostructures and nanostructures*. Elsevier, 2011.

[11] VB Anzin, MI Eremets, Yu V Kosichkin, AI Nadezhdinskii, and AM Shirokov. Measurement of the energy gap in tellurium under pressure. *physica status solidi (a)*, 42(1):385–390, 1977.

[12] VB Anzin, MI Eremets, Yu V Kosichkin, AI Nadezhdinskii, and AM Shirokov. Measurement of the energy gap in tellurium under pressure. *physica status solidi (a)*, 42(1):385–390, 1977.

[13] Hideo Asahina and Akira Morita. Band structure and optical properties of black phosphorus. *Journal of Physics C: Solid State Physics*, 17(11):1839, 1984.

[14] Michal Bajdich, Jens K Nørskov, and Aleksandra Vojvodic. Surface energetics of alkaline-earth metal oxides: Trends in stability and adsorption of small molecules. *Physical Review B*, 91(15):155401, 2015.

[15] Jillian F Banfield, David R Veblen, and David J Smith. The identification of naturally occurring tio 2 (b) by structure determination using high-resolution electron microscopy, image simulation, and distance-least-squares refinement. *American Mineralogist*, 76(3-4):343–353, 1991.

[16] CS Barrett, P Cucka, and K Haefner. The crystal structure of antimony at 4.2, 78 and 298 k. *Acta Crystallographica*, 16(6):451–453, 1963.

[17] Carl H Bates, William B White, and Rustum Roy. New high-pressure polymorph of zinc oxide. *Science*, 137(3534):993–993, 1962.

[18] T Bazhirov, M Mohammadi, K Ding, and S Barabash. Large-scale high-throughput computer-aided discovery of advanced materials using cloud computing. *Proceedings of the American Physical Society March Meeting 2017*, 2017.

[19] JA Berger, Lucia Reining, and Francesco Sottile. Ab initio calculations of electronic excitations: Collapsing spectral sums. *Physical Review B*, 82(4):041103, 2010.

[20] Robert F Berger and Jeffrey B Neaton. Computational design of low-band-gap double perovskites. *Physical Review B*, 86(16):165211, 2012.

[21] JD Bernal, E Djatlowa, I Kasarnowsky, S Reichstein, and AG Ward. The structure of strontium and barium peroxides sro2 and bao2. *Zeitschrift für Kristallographie-Crystalline Materials*, 92(1-6):344–354, 1935.

[22] Xavier Blase, Angel Rubio, Steven G Louie, and Marvin L Cohen. Quasiparticle band structure of bulk hexagonal boron nitride and related systems. *Physical review B*, 51(11):6868, 1995.

[23] Peter E Blöchl. Projector augmented-wave method. *Physical review B*, 50(24):17953, 1994.

[24] L Britnell, RV Gorbachev, R Jalil, BD Belle, F Schedin, A Mishchenko, T Georgiou, MI Katsnelson, L Eaves, SV Morozov, et al. Field-effect tunneling transistor based on vertical graphene heterostructures. *Science*, 335(6071):947–950, 2012.

[25] KD Bronsema, JL De Boer, and F Jellinek. On the structure of molybdenum diselenide and disulfide. *Zeitschrift für anorganische und allgemeine Chemie*, 540(9-10):15–17, 1986.

[26] KD Bronsema, JL De Boer, and F Jellinek. On the structure of molybdenum diselenide and disulfide. *Zeitschrift für anorganische und allgemeine Chemie*, 540(9-10):15–17, 1986.

[27] Allan Brown and Stig Rundqvist. Refinement of the crystal structure of black phosphorus. *Acta Crystallographica*, 19(4):684–685, 1965.

[28] LD Brownlee. Lattice constant of grey tin. *Nature*, 166(4220):482, 1950.

[29] Sabina Caneva, Robert S Weatherup, Bernhard C Bayer, Raoul Blume, Andrea Cabrero-Vilatela, Philipp Braeuninger-Weimer, Marie-Blandine Martin, Ruizhi Wang, Carsten Baehtz, Robert Schloegl, et al. Controlling catalyst bulk reservoir effects for monolayer hexagonal boron nitride cvd. *Nano letters*, 16(2):1250–1261, 2016.

[30] Ting Cao, Zhenglu Li, and Steven G. Louie. Tunable magnetism and half-metallicity in hole-doped monolayer gase. *Phys. Rev. Lett.*, 114:236602, Jun 2015.

[31] A Casalot, P Dougier, and P Hagenmuller. Sur l'evolution des proprietes physiques de la perovskite gdcoo3 entre 77 et 1200 k. *Journal of Physics and Chemistry of Solids*, 32(2):407–415, 1971.

[32] Guillaume Cassabois, Pierre Valvin, and Bernard Gil. Hexagonal boron nitride is an indirect bandgap semiconductor. *Nature Photonics*, 10(4):nphoton–2015, 2016.

[33] A Chainani, M Mathew, and DD Sarma. Electron-spectroscopy study of the semiconductor-metal transition in la 1- x sr x coo 3. *Physical Review B*, 46(16):9976, 1992.

[34] Tawinan Cheiwchanchamnangij and Walter RL Lambrecht. Quasiparticle band structure calculation of monolayer, bilayer, and bulk mos 2. *Physical Review B*, 85(20):205302, 2012.

[35] Xiaolong Chen, Yingying Wu, Zefei Wu, Yu Han, Shuigang Xu, Lin Wang, Weiguang Ye, Tianyi Han, Yuheng He, Yuan Cai, et al. High-quality sandwiched black phosphorus heterostructure and its quantum oscillations. *Nature communications*, 6:7315, 2015.

[36] Jason M. Crowley, Jamil Tahir-Kheli, and William A. Goddard. Resolution of the band gap prediction problem for materials design. *The Journal of Physical Chemistry Letters*, 7(7):1198–1203, 2016. PMID: 26944092.

[37] P Cucka and CS Barrett. The crystal structure of bi and of solid solutions of pb, sn, sb and te in bi. *Acta Crystallographica*, 15(9):865–872, 1962.

[38] Stefano Curtarolo, Wahyu Setyawan, Shidong Wang, Junkai Xue, Kesong Yang, Richard H Taylor, Lance J Nelson, Gus LW Hart, Stefano Sanvito, Marco Buongiorno-Nardelli, et al. Aflowlib. org: A distributed materials properties repository from high-throughput ab initio calculations. *Computational Materials Science*, 58:227–235, 2012.

[39] BF Decker and JS Kasper. The crystal structure of a simple rhombohedral form of boron. *Acta Crystallographica*, 12(7):503–506, 1959.

[40] A Ennaoui, S Fiechter, Ch Pettenkofer, N Alonso-Vante, K Büker, M Bronold, Ch Höpfner, and H Tributsch. Iron disulfide for solar energy conversion. *Solar Energy Materials and Solar Cells*, 29(4):289–370, 1993.

[41] M. Ernzerhof and G. E. Scuseria. Assessment of the Perdew-Burke-Ernzerhof exchange-correlation functional. *J. Chem. Phys.*, 110:5029–5036, 1999.

[42] Claudio Ferrari and Claudio Bocchi. Strain and composition determination in semiconducting heterostructures by high-resolution x-ray diffraction. In *Characterization of Semiconductor Heterostructures and Nanostructures*, pages 93–132. Elsevier, 2008.

[43] Larry W Finger and Robert M Hazen. Crystal structure and compression of ruby to 46 kbar. *Journal of Applied Physics*, 49(12):5823–5826, 1978.

[44] Li Gao, Jeffrey R Guest, and Nathan P Guisinger. Epitaxial graphene on cu (111). *Nano letters*, 10(9):3512–3516, 2010.

[45] Yang Gao, Wencai Ren, Teng Ma, Zhibo Liu, Yu Zhang, Wen-Bin Liu, Lai-Peng Ma, Xiuliang Ma, and Hui-Ming Cheng. Repeated and controlled growth of monolayer, bilayer and few-layer hexagonal boron nitride on pt foils. *ACS nano*, 7(6):5199–5206, 2013.

[46] JL Garcia-Munoz, J Rodriguez-Carvajal, Ph Lacorre, and JB Torrance. Neutron-diffraction study of r nio 3 (r= la, pr, nd, sm): Electronically induced structural changes across the metal-insulator transition. *Physical review B*, 46(8):4414, 1992.

[47] Roland Gillen and John Robertson. Accurate screened exchange band structures for the transition metal monoxides mno, feo, coo and nio. *Journal of Physics: Condensed Matter*, 25(16):165502, 2013.

[48] Lídia C Gomes and A Carvalho. Phosphorene analogues: Isoelectronic two-dimensional group-iv monochalcogenides with orthorhombic structure. *Physical Review B*, 92(8):085406, 2015.

[49] David L Greenaway and Rudolf Nitsche. Preparation and optical properties of group iv–vi2 chalcogenides having the cdi2 structure. *Journal of Physics and Chemistry of Solids*, 26(9):1445–1458, 1965.

[50] S Grimme. Semiempirical gga-type density functional constructed with a long-range dispersion correction. *Journal of computational chemistry*, 27(15):1787–1799, November 2006.

[51] TA Grzybowski and AL Ruoff. High-pressure phase transition in base. *Physical Review B*, 27(10):6502, 1983.

[52] Thomas A Grzybowski and Arthur L Ruoff. Band-overlap metallization of bate. *Physical review letters*, 53(5):489, 1984.

[53] Yuzheng Guo and John Robertson. Band structure, band offsets, substitutional doping, and schottky barriers of bulk and monolayer inse. *Physical Review Materials*, 1(4):044004, 2017.

[54] Sten Haastrup, Mikkel Strange, Mohnish Pandey, Thorsten Deilmann, Per S Schmidt, Nicki F Hinsche, Morten N Gjerding, Daniele Torelli, Peter M Larsen, Anders C Riis-Jensen, et al. The computational 2d materials database: High-throughput modeling and discovery of atomically thin crystals. *arXiv preprint arXiv:1806.03173*, 2018.

[55] Mohamed Hacene, Ani Anciaux-Sedrakian, Xavier Rozanska, Diego Klahr, Thomas Guignon, and Paul Fleurat-Lessard. Accelerating vasp electronic structure calculations using graphic processing units. *Journal of computational chemistry*, 33(32):2581–2589, 2012.

[56] Clevin Handschin, Bálint Fülöp, Péter Makk, Sofya Blanter, Markus Weiss, Kenji Watanabe, Takashi Taniguchi, Szabolcs Csonka, and Christian Schönenberger. Point contacts in encapsulated graphene. *Applied Physics Letters*, 107(18):183108, 2015.

[57] Judith Harl, Laurids Schimka, and Georg Kresse. Assessing the quality of the random phase approximation for lattice constants and atomization energies of solids. *Phys. Rev. B*, 81:115126, Mar 2010.

[58] Y Hasegawa and Ph Avouris. Direct observation of standing wave formation at surface steps using scanning tunneling spectroscopy. *Physical Review Letters*, 71(7):1071, 1993.

[59] Jochen Heyd, Juan E Peralta, Gustavo E Scuseria, and Richard L Martin. Energy band gaps and lattice parameters evaluated with the heyd-scuseria-ernzerhof screened hybrid functional. *The Journal of chemical physics*, 123(17):174101, 2005.

[60] Jochen Heyd, Gustavo E Scuseria, and Matthias Ernzerhof. Hybrid functionals based on a screened coulomb potential. *The Journal of chemical physics*, 118(18):8207–8215, 2003.

[61] David T Hodul and Angelica M Stacy. Anomalies in the properties of hf (s2- xtex) 1-y and hf (se2- xtex) 1- y near the metal-insulator transition. *Journal of Solid State Chemistry*, 54(3):438–446, 1984.

[62] P. Hohenberg and W. Kohn. Inhomogeneous electron gas. *Phys. Rev.*, 136(3B):B864–B871, Nov 1964.

[63] Michel Houssa, Konstantina Iordanidou, Geoffrey Pourtois, Valery V Afanas' ev, and Andre Stesmans. Hole-doping induced ferromagnetism in monolayer SnO: A first-principles study. *ECS Transactions*, 80(1):339–345, 2017.

[64] Baoshan Hu, Hiroki Ago, Yoshito Ito, Kenji Kawahara, Masaharu Tsuji, Eisuke Magome, Kazushi Sumitani, Noriaki Mizuta, Ken-ichi Ikeda, and Seigi Mizuno. Epitaxial growth of large-area single-layer graphene over cu (111)/sapphire by atmospheric pressure cvd. *Carbon*, 50(1):57–65, 2012.

[65] PingAn Hu, Lifeng Wang, Mina Yoon, Jia Zhang, Wei Feng, Xiaona Wang, Zhenzhong Wen, Juan Carlos Idrobo, Yoshiyuki Miyamoto, David B Geohegan, and Kai

Xiao. Highly responsive ultrathin GaS nanosheet photodetectors on rigid and flexible substrates. *Nano Letters*, 13(4):1649–1654, 2013.

[66] Kerstin Hummer, Judith Harl, and Georg Kresse. Heyd-scuseria-ernzerhof hybrid functional for calculating the lattice dynamics of semiconductors. *Physical Review B*, 80(11):115205, 2009.

[67] Aftab M Hussain, Nimer Wehbe, and Muhammad M Hussain. Sisn diodes: Theoretical analysis and experimental verification. *Applied Physics Letters*, 107(8):082111, 2015.

[68] Mark S. Hybertsen and Steven G. Louie. First-principles theory of quasiparticles: Calculation of band gaps in semiconductors and insulators. *Phys. Rev. Lett.*, 55(13):1418–1421, Sep 1985.

[69] J Ihm, A Zunger, and M.L. Cohen. Momentum-space formalism for the total energy of solids. *Journal of Physics C: Solid State Physics*, 12(21):4409, 1979.

[70] Olexandr Isayev, Corey Oses, Cormac Toher, Eric Gossett, Stefano Curtarolo, and Alexander Tropsha. Universal fragment descriptors for predicting properties of inorganic crystals. *Nature Communications*, 8:15679 EP –, Jun 2017. Article.

[71] Yoshinobu Ishii, Jun-ichi Murakami, and Minoru Itoh. Optical spectra of excitons in lithium oxide. *Journal of the Physical Society of Japan*, 68(2):696–697, 1999.

[72] Ariel Ismach, Harry Chou, Domingo A Ferrer, Yaping Wu, Stephen McDonnell, Herman C Floresca, Alan Covacevich, Cody Pope, Richard Piner, Moon J Kim, et al. Toward the controlled synthesis of hexagonal boron nitride films. *Acs Nano*, 6(7):6378–6385, 2012.

[73] K Jackson, L Ramakrishnan, K Muriki, S Canon, S Cholia, J Shalf, H Wasserman, and N Wright. Performance analysis of high performance computing applications on the amazon web services cloud. *Proceedings of the IEEE Second International Conference on Cloud Computing Technology and Science (CloudCom 2010)*, pages 159–168, 2010.

[74] Anubhav Jain, Shyue Ping Ong, Geoffroy Hautier, Wei Chen, William Davidson Richards, Stephen Dacek, Shreyas Cholia, Dan Gunter, David Skinner, Gerbrand Ceder, et al. Commentary: The materials project: A materials genome approach to accelerating materials innovation. *Apl Materials*, 1(1):011002, 2013.

[75] Anderson Janotti and Chris G Van de Walle. Lda+ u and hybrid functional calculations for defects in zno, sno2, and tio2. *physica status solidi (b)*, 248(4):799–804, 2011.

[76] W Jauch and A Palmer. Anomalous zero-point motion in srtio 3: results from γ-ray diffraction. *Physical Review B*, 60(5):2961, 1999.

[77] F Jensen, Flemming Besenbacher, Erik Lægsgaard, and Ivan Stensgaard. Surface reconstruction of cu (110) induced by oxygen chemisorption. *Physical Review B*, 41(14):10233, 1990.

[78] Eric R Jette and Frank Foote. Precision determination of lattice constants. *The Journal of Chemical Physics*, 3(10):605–616, 1935.

[79] Steven G Johnson and John D Joannopoulos. Block-iterative frequency-domain methods for maxwells equations in a planewave basis. *Optics express*, 8(3):173–190, 2001.

[80] Isao Kagomiya, Kay Kohn, and Tomohiro Uchiyama. Structure and ferroelectricity of rmn 2 o 5. *Ferroelectrics*, 280(1):131–143, 2002.

[81] D Kecik, E Durgun, and S Ciraci. Stability of single-layer and multilayer arsenene and their mechanical and electronic properties. *Physical Review B*, 94(20):205409, 2016.

[82] R Keller, WB Holzapfel, and Heinz Schulz. Effect of pressure on the atom positions in se and te. *Physical Review B*, 16(10):4404, 1977.

[83] Gwangwoo Kim, A-Rang Jang, Hu Young Jeong, Zonghoon Lee, Dae Joon Kang, and Hyeon Suk Shin. Growth of high-crystalline, single-layer hexagonal boron nitride on recyclable platinum foil. *Nano letters*, 13(4):1834–1839, 2013.

[84] Ki Kang Kim, Allen Hsu, Xiaoting Jia, Soo Min Kim, Yumeng Shi, Mildred Dresselhaus, Tomas Palacios, and Jing Kong. Synthesis and characterization of hexagonal boron nitride film as a dielectric layer for graphene devices. *ACS nano*, 6(10):8583–8590, 2012.

[85] Ki Kang Kim, Allen Hsu, Xiaoting Jia, Soo Min Kim, Yumeng Shi, Mario Hofmann, Daniel Nezich, Joaquin F Rodriguez-Nieva, Mildred Dresselhaus, Tomas Palacios, et al. Synthesis of monolayer hexagonal boron nitride on cu foil using chemical vapor deposition. *Nano letters*, 12(1):161–166, 2011.

[86] Soo Min Kim, Allen Hsu, Min Ho Park, Sang Hoon Chae, Seok Joon Yun, Joo Song Lee, Dae-Hyun Cho, Wenjing Fang, Changgu Lee, Tomás Palacios, et al. Synthesis of large-area multilayer hexagonal boron nitride for high material performance. *Nature communications*, 6:8662, 2015.

[87] Charles Kittel, Paul McEuen, and Paul McEuen. *Introduction to solid state physics*, volume 8. Wiley New York, 1996.

[88] Wilhelm Klein, Klaus Armbruster, and Martin Jansen. Synthesis and crystal structure determination of sodium ozonide. *Chemical Communications*, (6):707–708, 1998.

[89] Gerhard Klimeck, Michael McLennan, Sean P Brophy, George B Adams III, and Mark S Lundstrom. nanohub. org: Advancing education and research in nanotechnology. *Computing in Science & Engineering*, 10(5):17–23, 2008.

[90] Walter Kohn and Lu Jeu Sham. Self-consistent equations including exchange and correlation effects. *Physical review*, 140(4A):A1133, 1965.

[91] Eugene B Kolomeisky and Joseph P Straley. Anomalous screening in two-dimensional materials with an extremum ring in the dispersion law. *Physical Review B*, 94(24):245150, 2016.

[92] G Kresse. Software vasp, vienna, 1999; g. kresse, j. furthmüller. *Phys. Rev. B*, 54(11):169, 1996.

[93] G. Kresse and J. Hafner. Ab initio molecular dynamics for liquid metals. *Phys. Rev. B*, 47(1):558–561, Jan 1993.

[94] G Kresse, M Marsman, LE Hintzsche, and E Flage-Larsen. Optical and electronic properties of si 3 n 4 and α-sio 2. *Physical Review B*, 85(4):045205, 2012.

[95] Georg Kresse and Jürgen Furthmüller. Efficient iterative schemes for ab initio total-energy calculations using a plane-wave basis set. *Physical review B*, 54(16):11169, 1996.

[96] Yoichi Kubota, Kenji Watanabe, Osamu Tsuda, and Takashi Taniguchi. Deep ultraviolet light-emitting hexagonal boron nitride synthesized at atmospheric pressure. *Science*, 317(5840):932–934, 2007.

[97] D Kucharczyk and T Niklewski. Accurate x-ray determination of the lattice parameters and the thermal expansion coefficients of vo2 near the transition temperature. *Journal of Applied Crystallography*, 12(4):370–373, 1979.

[98] Ph Lacorre, JB Torrance, JSAI Pannetier, AI Nazzal, PW Wang, and TC Huang. Synthesis, crystal structure, and properties of metallic prnio3: Comparison with metallic ndnio3 and semiconducting smnio3. *Journal of Solid State Chemistry*, 91(2):225–237, 1991.

[99] S Laref and A Laref. Comparative study on the performance of exchange and correlation in wide-gap semiconductors: the case of bes, bese, and bete. *Journal of Materials Science*, 48(16):5499–5508, 2013.

[100] Ask Hjorth Larsen, Jens Jørgen Mortensen, Jakob Blomqvist, Ivano E Castelli, Rune Christensen, Marcin Dułak, Jesper Friis, Michael N Groves, Bjørk Hammer, Cory Hargus, et al. The atomic simulation environmenta python library for working with atoms. *Journal of Physics: Condensed Matter*, 29(27):273002, 2017.

[101] Joohwi Lee, Atsuto Seko, Kazuki Shitara, Keita Nakayama, and Isao Tanaka. Prediction model of band gap for inorganic compounds by combination of density functional theory calculations and machine learning techniques. *Physical Review B*, 93(11):115104, 2016.

[102] Sidong Lei, Liehui Ge, Zheng Liu, Sina Najmaei, Gang Shi, Ge You, Jun Lou, Robert Vajtai, and Pulickel M Ajayan. Synthesis and photoresponse of large GaSe atomic layers. *Nano Letters*, 13(6):2777–2781, 2013.

[103] Sidong Lei, Liehui Ge, Sina Najmaei, Antony George, Rajesh Kappera, Jun Lou, Manish Chhowalla, Hisato Yamaguchi, Gautam Gupta, Robert Vajtai, et al. Evolution of the electronic band structure and efficient photo-detection in atomic layers of inse. *ACS nano*, 8(2):1263–1272, 2014.

[104] Kurt Lejaeghere, Gustav Bihlmayer, Torbjörn Björkman, Peter Blaha, Stefan Blügel, Volker Blum, Damien Caliste, Ivano E. Castelli, Stewart J. Clark, Andrea Dal Corso, Stefano de Gironcoli, Thierry Deutsch, John Kay Dewhurst, Igor Di Marco, Claudia Draxl, Marcin Dułak, Olle Eriksson, José A. Flores-Livas, Kevin F. Garrity, Luigi Genovese, Paolo Giannozzi, Matteo Giantomassi, Stefan Goedecker, Xavier Gonze, Oscar Grånäs, E. K. U. Gross, Andris Gulans, François Gygi, D. R. Hamann, Phil J. Hasnip, N. A. W. Holzwarth, Diana Iuşan, Dominik B. Jochym, François Jollet, Daniel Jones, Georg Kresse, Klaus Koepernik, Emine Küçükbenli, Yaroslav O. Kvashnin, Inka L. M. Locht, Sven Lubeck, Martijn Marsman, Nicola Marzari, Ulrike Nitzsche, Lars Nordström, Taisuke Ozaki, Lorenzo Paulatto, Chris J. Pickard, Ward Poelmans, Matt I. J. Probert, Keith Refson, Manuel Richter, Gian-Marco Rignanese, Santanu Saha, Matthias Scheffler, Martin Schlipf, Karlheinz Schwarz, Sangeeta Sharma, Francesca Tavazza, Patrik Thunström, Alexandre Tkatchenko, Marc Torrent, David Vanderbilt, Michiel J. van Setten, Veronique Van Speybroeck, John M. Wills, Jonathan R. Yates, Guo-Xu Zhang, and Stefaan Cottenier. Reproducibility in density functional theory calculations of solids. *Science*, 351(6280), 2016.

[105] Mark P Levendorf, Cheol-Joo Kim, Lola Brown, Pinshane Y Huang, Robin W Havener, David A Muller, and Jiwoong Park. Graphene and boron nitride lateral heterostructures for atomically thin circuitry. *Nature*, 488(7413):627, 2012.

[106] Xuesong Li, Weiwei Cai, Jinho An, Seyoung Kim, Junghyo Nah, Dongxing Yang, Richard Piner, Aruna Velamakanni, Inhwa Jung, Emanuel Tutuc, et al. Large-area synthesis of high-quality and uniform graphene films on copper foils. *Science*, 324(5932):1312–1314, 2009.

[107] Yuanchang Li. Gate-independent energy gap in noncovalently intercalated bilayer graphene on sic (0001). *Physical Review B*, 94(24):245144, 2016.

[108] Jianping Long, Lijun Yang, and Xuesong Wei. Lattice, elastic properties and debye temperatures of atio3 (a= ba, ca, pb, sr) from first-principles. *Journal of Alloys and Compounds*, 549:336–340, 2013.

[109] Huan Luo, Raymond G Greene, Kouros Ghandehari, Ting Li, and Arthur L Ruoff. Structural phase transformations and the equations of state of calcium chalcogenides at high pressure. *Physical review B*, 50(22):16232, 1994.

[110] Nan Ma and Debdeep Jena. Charge scattering and mobility in atomically thin semiconductors. *Physical Review X*, 4(1):011043, 2014.

[111] Jesse Maassen and Mark Lundstrom. A computational study of the thermoelectric performance of ultrathin Bi_2Te_3 films. *Applied Physics Letters*, 102(9):093103, 2013.

[112] Otfried Madelung. *Semiconductors: data handbook*. Springer Science & Business Media, 2012.

[113] Masoud Mahjouri-Samani, Mengkun Tian, Kai Wang, Abdelaziz Boulesbaa, Christopher M Rouleau, Alexander A Puretzky, Michael A McGuire, Bernadeta R Srijanto, Kai Xiao, Gyula Eres, et al. Digital transfer growth of patterned 2d metal chalcogenides by confined nanoparticle evaporation. *Acs Nano*, 8(11):11567–11575, 2014.

[114] Pierre F Maldague. Many-body corrections to the polarizability of the two-dimensional electron gas. *Surface Science*, 73:296–302, 1978.

[115] Gregory J McCarthy and Jean M Welton. X-ray diffraction data for sno 2. an illustration of the new powder data evaluation methods. *Powder Diffraction*, 4(3):156–159, 1989.

[116] Gregory J McCarthy, William B White, and Rustum Roy. Preparation and structure of the rare earth titanates. *Materials Research Bulletin*, 4(4):251–255, 1969.

[117] Leo Merrill. Behavior of the ab-type compounds at high pressures and high temperatures. *Journal of Physical and Chemical Reference Data*, 6(4):1205–1252, 1977.

[118] Hongki Min, Bhagawan Sahu, Sanjay K. Banerjee, and A. H. MacDonald. Ab initio theory of gate induced gaps in graphene bilayers. *Phys. Rev. B*, 75(15):155115, Apr 2007.

[119] Horst Mittendorf. Röntgenographische und optische untersuchungen aufgedampfter schichten aus erdalkalichalkogeniden. *Zeitschrift für Physik*, 183(2):113–129, 1965.

[120] Mohammad Mohammadi and Timur Bazhirov. Comparative benchmarking of cloud computing vendors with high performance linpack. In *Proceedings of the 2Nd International Conference on High Performance Compilation, Computing and Communications*, HP3C, pages 1–5, New York, NY, USA, 2018. ACM.

[121] Hajar Nejatipour and Mehrdad Dadsetani. Excitonic effects in the optical properties of alkaline earth chalcogenides from first-principles calculations. *Physica Scripta*, 90(8):085802, 2015.

[122] Shu Nie, Joseph M Wofford, Norman C Bartelt, Oscar D Dubon, and Kevin F McCarty. Origin of the mosaicity in graphene grown on cu (111). *Physical Review B*, 84(15):155425, 2011.

[123] Yaozhuang Nie, Mavlanjan Rahman, Pei Liu, Aihemaitijiang Sidike, Qinglin Xia, and Guang-hua Guo. Room-temperature half-metallicity in monolayer honeycomb structures of group-v binary compounds with carrier doping. *Physical Review B*, 96(7):075401, 2017.

[124] Yui Ogawa, Baoshan Hu, Carlo M Orofeo, Masaharu Tsuji, Ken-ichi Ikeda, Seigi Mizuno, Hiroki Hibino, and Hiroki Ago. Domain structure and boundary in single-layer graphene grown on cu (111) and cu (100) films. *The Journal of Physical Chemistry Letters*, 3(2):219–226, 2012.

[125] Shyue Ping Ong, William Davidson Richards, Anubhav Jain, Geoffroy Hautier, Michael Kocher, Shreyas Cholia, Dan Gunter, Vincent L Chevrier, Kristin A Persson, and Gerbrand Ceder. Python materials genomics (pymatgen): A robust, open-source python library for materials analysis. *Computational Materials Science*, 68:314–319, 2013.

[126] Zhun-Yong Ong and Massimo V. Fischetti. Mobility enhancement and temperature dependence in top-gated single–layer MoS_2. *Physical Review B*, 88(16):165316, 2013.

[127] John P. Perdew, Kieron Burke, and Matthias Ernzerhof. Generalized Gradient Approximation Made Simple. *Phys. Rev. Lett.*, 77:3865–3868, 1996.

[128] John P Perdew, Kieron Burke, and Matthias Ernzerhof. Generalized gradient approximation made simple. *Physical review letters*, 77(18):3865, 1996.

[129] Giovanni Pizzi, Andrea Cepellotti, Riccardo Sabatini, Nicola Marzari, and Boris Kozinsky. Aiida: automated interactive infrastructure and database for computational science. *Computational Materials Science*, 111:218–230, 2016.

[130] JJ Pluth, JV Smith, and J Faber Jr. Crystal structure of low cristobalite at 10, 293, and 473 k: Variation of framework geometry with temperature. *Journal of Applied Physics*, 57(4):1045–1049, 1985.

[131] RC Powell, N-E Lee, Y-W Kim, and JE Greene. Heteroepitaxial wurtzite and zinc-blende structure gan grown by reactive-ion molecular-beam epitaxy: Growth kinetics, microstructure, and properties. *Journal of applied physics*, 73(1):189–204, 1993.

[132] CT Prewitt and RD Shannon. Crystal structure of a high-pressure form of b2o3. *Acta Crystallographica Section B: Structural Crystallography and Crystal Chemistry*, 24(6):869–874, 1968.

[133] William Primak, Herman Kaufman, and Roland Ward. X-ray diffraction studies of systems involved in the preparation of alkaline earth sulfide and selenide phosphors1. *Journal of the American Chemical Society*, 70(6):2043–2046, 1948.

[134] AS Rao and RJ Kearney. Logarithmic derivative reflectance spectra of bao and sro. *physica status solidi (b)*, 95(1):243–250, 1979.

[135] Filip A Rasmussen and Kristian S Thygesen. Computational 2d materials database: electronic structure of transition-metal dichalcogenides and oxides. *The Journal of Physical Chemistry C*, 119(23):13169–13183, 2015.

[136] A Riefer, F Fuchs, C Rödl, A Schleife, F Bechstedt, and R Goldhahn. Interplay of excitonic effects and van hove singularities in optical spectra: Cao and aln polymorphs. *Physical Review B*, 84(7):075218, 2011.

[137] John Robertson. Band offsets of wide-band-gap oxides and implications for future electronic devices. *Journal of Vacuum Science & Technology B: Microelectronics and Nanometer Structures Processing, Measurement, and Phenomena*, 18(3):1785–1791, 2000.

[138] Andreas Rüegg, Chandrima Mitra, Alexander A Demkov, and Gregory A Fiete. Electronic structure of (lanio 3) 2/(laalo 3) n heterostructures grown along [111]. *Physical Review B*, 85(24):245131, 2012.

[139] James E Saal, Scott Kirklin, Muratahan Aykol, Bryce Meredig, and Christopher Wolverton. Materials design and discovery with high-throughput density functional theory: the open quantum materials database (oqmd). *Jom*, 65(11):1501–1509, 2013.

[140] Y Saeed, N Singh, and U Schwingenschlögl. Thickness and strain effects on the thermoelectric transport in nanostructured Bi_2Se_3. *Applied Physics Letters*, 104(3):033105, 2014.

[141] Bivas Saha, Timothy D Sands, and Umesh V Waghmare. Electronic structure, vibrational spectrum, and thermal properties of yttrium nitride: A first-principles study. *Journal of Applied Physics*, 109(7):073720, 2011.

[142] Satoshi SASAKI, Kiyoshi FUJINO, and Yoshio TAKÉUCHI. X-ray determination of electron-density distributions in oxides, mgo, mno, coo, and nio, and atomic scattering factors of their constituent atoms. *Proceedings of the Japan Academy, Series B*, 55(2):43–48, 1979.

[143] L Seixas, AS Rodin, A Carvalho, and AH Castro Neto. Multiferroic two-dimensional materials. *Physical review letters*, 116(20):206803, 2016.

[144] Hâldun Sevinçli. Quartic dispersion, strong singularity, magnetic instability, and unique thermoelectric properties in two-dimensional hexagonal lattices of group-va elements. *Nano Letters*, 17(4):2589–2595, 2017.

[145] Liwei Shi, Yun Qin, Jing Hu, Yifeng Duan, Licheng Qu, Ling Wu, and Gang Tang. Strain-assisted structural transformation and band gap tuning in beo, mgte, cds and 2h-sic: A hybrid density functional study. *EPL (Europhysics Letters)*, 106(5):57001, 2014.

[146] Yumeng Shi, Christoph Hamsen, Xiaoting Jia, Ki Kang Kim, Alfonso Reina, Mario Hofmann, Allen Long Hsu, Kai Zhang, Henan Li, Zhen-Yu Juang, et al. Synthesis of few-layer hexagonal boron nitride thin film by chemical vapor deposition. *Nano letters*, 10(10):4134–4139, 2010.

[147] M Shishkin and G Kresse. Self-consistent g w calculations for semiconductors and insulators. *Physical Review B*, 75(23):235102, 2007.

[148] M Shishkin, M Marsman, and G Kresse. Accurate quasiparticle spectra from self-consistent gw calculations with vertex corrections. *Physical review letters*, 99(24):246403, 2007.

[149] Jonathan H. Skone, Marco Govoni, and Giulia Galli. Self-consistent hybrid functional for condensed systems. *Phys. Rev. B*, 89:195112, May 2014.

[150] PM Smith, AJ Leadbetter, and AJ Apling. The structures of orthorhombic and vitreous arsenic. *Philosophical Magazine*, 31(1):57–64, 1975.

[151] VL Solozhenko, G Will, and F Elf. Isothermal compression of hexagonal graphite-like boron nitride up to 12 gpa. *Solid state communications*, 96(1):1–3, 1995.

[152] Christoph Sommer, Peter Krüger, and Johannes Pollmann. Quasiparticle band structure of alkali-metal fluorides, oxides, and nitrides. *Physical Review B*, 85(16):165119, 2012.

[153] RA Soref. Electro-optical and nonlinear optical coefficients of ordered group iv semiconductor alloys. *Journal of applied physics*, 72(2):626–630, 1992.

[154] Tobias Stauber, NMR Peres, Francisco Guinea, and AH Castro Neto. Fermi liquid theory of a fermi ring. *Physical Review B*, 75(11):115425, 2007.

[155] Shigemasa Suga, Christian Tusche, Yu-ichiro Matsushita, Martin Ellguth, Akinori Irizawa, and Jürgen Kirschner. Momentum microscopy of the layered semiconductor tis2 and ni intercalated ni1/3tis2. *New Journal of Physics*, 17(8):083010, 2015.

[156] Michael P. Surh, Ming-Fu Li, and Steven G. Louie. Spin-orbit splitting of gaas and insb bands near Γ. *Phys. Rev. B*, 43:4286–4294, Feb 1991.

[157] Roland Yingjie Tay, Mark H Griep, Govind Mallick, Siu Hon Tsang, Ram Sevak Singh, Travis Tumlin, Edwin Hang Tong Teo, and Shashi P Karna. Growth of large single-crystalline two-dimensional boron nitride hexagons on electropolished copper. *Nano letters*, 14(2):839–846, 2014.

[158] G Thornton, BC Tofield, and AW Hewat. A neutron diffraction study of lacoo3 in the temperature range 4.2¡ t¡ 1248 k. *Journal of Solid State Chemistry*, 61(3):301–307, 1986.

[159] Hao Tian, Alireza Khanaki, Protik Das, Renjing Zheng, Zhenjun Cui, Yanwei He, Wenhao Shi, Zhongguang Xu, Roger Lake, and Jianlin Liu. Role of carbon interstitials in transition metal substrates on controllable synthesis of high-quality large-area two-dimensional hexagonal boron nitride layers. *Nano letters*, 18(6):3352–3361, 2018.

[160] Maytal Caspary Toroker, Dalal K Kanan, Nima Alidoust, Leah Y Isseroff, Peilin Liao, and Emily A Carter. First principles scheme to evaluate band edge positions in potential transition metal oxide photocatalysts and photoelectrodes. *Physical Chemistry Chemical Physics*, 13(37):16644–16654, 2011.

[161] Fabien Tran and Peter Blaha. Accurate band gaps of semiconductors and insulators with a semilocal exchange-correlation potential. *Physical review letters*, 102(22):226401, 2009.

[162] Vy Tran, Ryan Soklaski, Yufeng Liang, and Li Yang. Layer-controlled band gap and anisotropic excitons in few-layer black phosphorus. *Physical Review B*, 89(23):235319, 2014.

[163] VG Tsirelson, AS Avilov, Yu A Abramov, EL Belokoneva, R Kitaneh, and D Feil. X-ray and electron diffraction study of mgo. *Acta Crystallographica Section B*, 54(1):8–17, 1998.

[164] St v. Náray-Szabó. Die strukturen von verbindungen abo 3 schwesterstrukturen. *Naturwissenschaften*, 31(39):466–466, 1943.

[165] K Van Benthem, C Elsässer, and RH French. Bulk electronic structure of srtio 3: experiment and theory. *Journal of applied physics*, 90(12):6156–6164, 2001.

[166] Mark van Schilfgaarde, Takao Kotani, and Sergey V Faleev. Adequacy of approximations in gw theory. *Physical Review B*, 74(24):245125, 2006.

[167] Anastasia Varlet, Dominik Bischoff, Pauline Simonet, Kenji Watanabe, Takashi Taniguchi, Thomas Ihn, Klaus Ensslin, Marcin Mucha-Kruczyński, and Vladimir I. Fal'ko. Anomalous sequence of quantum hall liquids revealing a tunable lifshitz transition in bilayer graphene. *Phys. Rev. Lett.*, 113:116602, Sep 2014.

[168] JB Varley, Anderson Janotti, Cesare Franchini, and Chris G Van de Walle. Role of self-trapping in luminescence and p-type conductivity of wide-band-gap oxides. *Physical Review B*, 85(8):081109, 2012.

[169] Pierre Villars, M Berndt, K Brandenburg, K Cenzual, J Daams, F Hulliger, T Massalski, H Okamoto, K Osaki, A Prince, et al. The pauling file. *Journal of Alloys and Compounds*, 367(1-2):293–297, 2004.

[170] Joel I-Jan Wang, Yafang Yang, Yu-An Chen, Kenji Watanabe, Takashi Taniguchi, Hugh OH Churchill, and Pablo Jarillo-Herrero. Electronic transport of encapsulated graphene and wse2 devices fabricated by pick-up of prepatterned hbn. *Nano letters*, 15(3):1898–1903, 2015.

[171] Logan Ward, Ankit Agrawal, Alok Choudhary, and Christopher Wolverton. A general-purpose machine learning framework for predicting properties of inorganic materials. *Npj Computational Materials*, 2:16028 EP –, Aug 2016. Article.

[172] Kenji Watanabe, Takashi Taniguchi, and Hisao Kanda. Direct-bandgap properties and evidence for ultraviolet lasing of hexagonal boron nitride single crystal. *Nature materials*, 3(6):404, 2004.

[173] Kenji Watanabe, Takashi Taniguchi, Takahiro Niiyama, Kenta Miya, and Masateru Taniguchi. Far-ultraviolet plane-emission handheld device based on hexagonal boron nitride. *Nature photonics*, 3(10):591–594, 2009.

[174] ZA Weinberg, GW Rubloff, and E Bassous. Transmission, photoconductivity, and the experimental band gap of thermally grown si o 2 films. *Physical Review B*, 19(6):3107, 1979.

[175] Darshana Wickramaratne, Ferdows Zahid, and Roger K Lake. Electronic and thermoelectric properties of few-layer transition metal dichalcogenides. *The Journal of chemical physics*, 140(12):124710, 2014.

[176] Darshana Wickramaratne, Ferdows Zahid, and Roger K Lake. Electronic and thermoelectric properties of van der waals materials with ring-shaped valence bands. *Journal of Applied Physics*, 118(7):075101, 2015.

[177] GA Wiegers and A Meerschaut. Structures of misfit layer compounds (ms) nts2 (mx sn, pb, bi, rare earth metals; ti nb, ta, ti, v, cr; 1.08¡ n¡ 1.23). *Journal of alloys and compounds*, 178(1-2):351–368, 1992.

[178] Sianxin Wu, Xia Dai, Hongyi Yu, Heng Fan, Jiangping Hu, and Wang Yao. Magnetisms in *p*-type monolayer gallium chalcogenides (GaSe, GaS). *arXiv preprint arXiv:1409.4733*, 2014.

[179] Xiaoyu Yang, Zongguo Wang, Xushan Zhao, Jianlong Song, Mingming Zhang, and Haidong Liu. Matcloud: A high-throughput computational infrastructure for integrated management of materials simulation, data and resources. *Computational Materials Science*, 146:319–333, 2018.

[180] Seho Yi, Zhili Zhu, Xiaolin Cai, Yu Jia, and Jun-Hyung Cho. The nature of bonding in bulk tellurium composed of one-dimensional helical chains. *Inorganic chemistry*, 57(9):5083–5088, 2018.

[181] Seho Yi, Zhili Zhu, Xiaolin Cai, Yu Jia, and Jun-Hyung Cho. The nature of bonding in bulk tellurium composed of one-dimensional helical chains. *Inorganic chemistry*, 57(9):5083–5088, 2018.

[182] WH Zachariasen. Crystal chemical studies of the 5f-series of elements. xii. new compounds representing known structure types. *Acta Crystallographica*, 2(6):388–390, 1949.

[183] Ferdows Zahid and Roger Lake. Thermoelectric properties of Bi_2Te_3 atomic quintuple thin films. *Applied Physics Letters*, 97(21):212102, 2010.

[184] Xiang-bo Zhang, Fu Gang, and Hui-lin Wan. Density functional theory study on spin states of lacoo3 at room temperature. *Chinese Journal of Chemical Physics*, 27(3):274–278, 2014.

[185] Renjing Zheng, Alireza Khanaki, Hao Tian, Yanwei He, Yongtao Cui, Zhongguang Xu, and Jianlin Liu. Precipitation growth of graphene under exfoliated hexagonal boron nitride to form heterostructures on cobalt substrate by molecular beam epitaxy. *Applied Physics Letters*, 111(1):011903, 2017.

[186] Houlong L Zhuang and Richard G Hennig. Single-layer group-III monochalcogenide photocatalysts for water splitting. *Chemistry of Materials*, 25(15):3232–3238, 2013.

[187] E Zintl, A Harder, and B Dauth. Gitterstruktur der oxyde, sulfide, selenide und telluride des lithiums, natriums und kaliums. *Zeitschrift für Elektrochemie und angewandte physikalische Chemie*, 40(8):588–593, 1934.

[188] V. Zolyomi, N. D. Drummond, and V. I. Fal'ko. Electrons and phonons in single layers of hexagonal indium chalcogenides from ab initio calculations. *Phys. Rev. B*, 89:205416, May 2014.

[189] Viktor Zolyomi, ND Drummond, and VI Fal'ko. Band structure and optical transitions in atomic layers of hexagonal gallium chalcogenides. *Physical Review B*, 87(19):195403, 2013.

Appendix A

Visualization and parameter extraction from density functional theory calculations

A.1 Introduction

Density Functional Theory (DFT) is a well-known method to investigate intrinsic material properties at 0K. To identify potential applications for any new material, the first step is to employ DFT calculations. Most of the DFT tools are written for systems running Linux environment. As a result, output data generated by these tools are written in plain ASCII text format. There is no agreed upon convention for writing the data. Each of the DFT tools has its own format for outputting data. This makes the visualization and parameter extraction a cumbersome process. This also slows down the throughput

of the research as one needs to develop a separate tool to visualize the data. Due to the improvement in the high-performance computing, the computation time is improved drastically within last few years. But due to the ambiguity involved to the output data for each of the tools, the visualization of the data and decision making from the data is not trivial.

The library is a visualization and parameter extraction tool for DFT calculations. This code closes the gap between the output data and the decision-making process. The first version of the code can plot band structure, plot ionic and orbital composition of the electronic band structure, various features of density of states (DOS), and can extract effective mass from the band structure. The tool is modularized and object oriented. As a result, this code can be extended to any DFT tool. At this point, the code is capable of visualization and parameter extraction of VASP calculations.

A.2 Input parameters

A DFT calculation involves several input parameters. For example, description of the material along with parameters that incorporate physics in the calculation. For VASP, the input parameters are divided into separate files. A summary of the input files for VASP is shown in Table A.1.

The INCAR file contains the keywords that are needed for a calculation. The POSCAR file contains the description of unit cell and the position of the atoms of a material. The POTCAR file contains the pseudopotentials for the elements of the material. The VASP official website contains a library of pseudopotentials for all the elements. The user needs

File name	Description
INCAR	Input parameters for the simulation
POSCAR	Structure information of the material
POTCAR	Pseudopotentials for the material
KPOINTS	K-points scheme for the calculation

Table A.1: Input files for a VASP simulation.

to create a pseudopotential file from the library of pseudopotentials. The sequence of the pseudopotentials needs to be same as the sequence of the POSCAR file. The KPOINTS file contains the grid of k-points for which the integration is done.

A.3 Data collection

For any calculation, VASP outputs its data in two formats. In one case the different data is outputted in separate text files. For example, the band structure, orbital contribution, and the density of states are written into files named EIGENVAL, PROCAR and DOSCAR files, respectively. Parameters like Fermi level is written into file named OUTCAR. Secondly, all the data for a calculation is also written to a xml file named vasprun.xml.

The primary language for development of the tool was Matlab. For calculations involving large structure, Matlab can run into memory problems due to the limitation of memory within the virtual Java system on which Matlab runs. To circumvent this problem,

a separate XML reader written in python has been developed. Matlab can be used to call a python script from its own environment. The library calls the appropriate python functions to read the data. The python script has dependency of numpy and scipy. If calling the python library fails, the code falls back to XML reader written using Matlab. In terms of performance, the Matlab reader is slower compared to its python counterpart, but it enables graceful execution of the code when python fails. The data that is read using code is stored in a predefined dimension.

The code uses a caching algorithm to store data. When an XML file is read for the first time, the read data is stored in a data file. For the consequent execution of the code for data processing, this mat file is used. As reading a mat file is much faster compared to reading an XML file, the processing of the data is much faster after the mat file is created. The library recognizes if there is a newer XML file compared to the mat data file and reads the XML file from scratch and finally creates a new mat data file. This caching can be manually controlled from the menu. The features of can be categorized into two parts: visualization and parameter extraction. The visualization part of the code can be used to generate and export publication quality figures of different properties available within DFT codes. The parameter extraction part of the code can calculate effective mass for both homogeneous and heterogeneous materials within different level of fidelity.

A.4 Installation

The installation of the library is trivial. The user needs to extract the package in a convenient directory and then add the directory to the Matlab path. Version

specific instruction for adding a directory to Matlab path can be found here: `https://www.mathworks.com/help/matlab/ref/addpath.html`. Adding the folder to the path makes sure that top level script along with other required scripts are accessible to Matlab.

For visualization purpose, user needs to change the current directory to the directory where the XML file is and run the top level script. Running the top level script executes a text based menu. During the execution of the text based menu, user is asked various question to determine the visualization or parameter extraction.

A.5 Visualization

The visualization part of the library can plot electronic band structure, orbital and ionic contribution of the atoms to the band structure, total, ionic and orbital contribution of density of states. We will be discussing each of the feature separately.

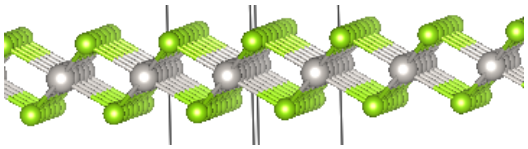

Figure A.1: Atomic structure of a $PtSe_2$ monolayer.

A.5.1 Band structure

Electronic band structure

Plotting of band structure is a basic visualization for DFT based calculation data. While the plotting seems trivial, the data can be in quite different formats based on the

theory applied during the calculation. To read the data properly, one needs to identify the level of theory used to generate the data. To read the data properly several cases to be considered. These cases can be:

- Band structure without any spin degeneracy or spin orbit coupling (SOC).
- Band structure with spin degeneracy.
- Band structure with SOC
- Band structure with HSE correction applied.

The library tries to determine the use case from the input tags which are provided in the XML file and read the data accordingly. For example, for the spin degeneracy case, the spin up and spin down cases are plotted side by side. For band structures calculated using HSE, the k-points of the irreducible Brillouin zone (IBZ) are also included in the calculation. To plot the data according to the path, the k-points of the IBZ needs to be removed. The library removes these k-points and the associated bands from the data and finally plots the band structure. Figure A.2 shows band structure of a monolayer $PtSe_2$ with SOC.

Atom projected band structure

Electronic band structure calculated using DFT can be projected into atoms or orbitals from where information about atomic or orbital contribution can be retrieved. This data can be an important tool for analyzing the material properties. VASP writes the atomic and orbital projected data in both PROCAR and vasprun.xml file. Depending on the level

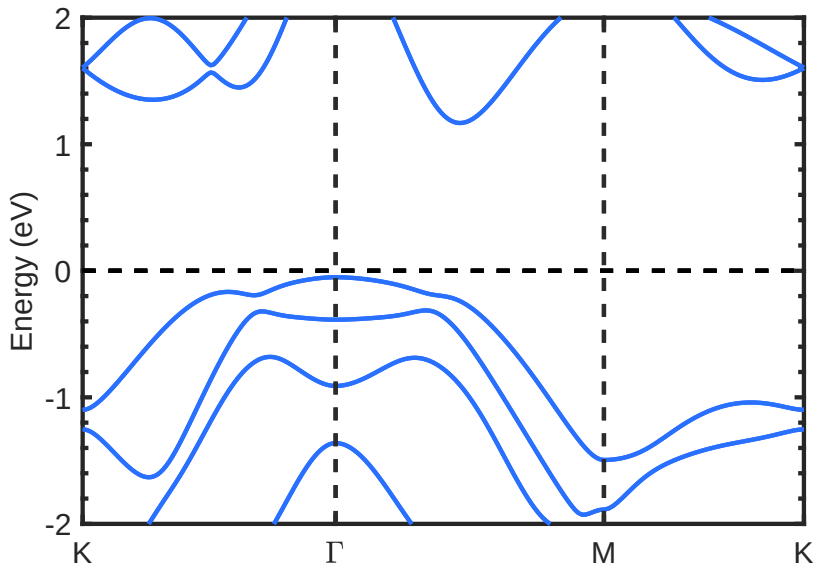

Figure A.2: Band structure of monolayer $PtSe_2$ plotted using the library.

of physics that is included, the dimension of the data can be different. Also, with number of atoms, the size of the data is increased linearly. The library identifies the dimension of the data from the input tags and reads the data from XML file. For the atom projected band structure, for each k-points of each band, the library calculates the contribution between different elements and assigns a color to the maximally contributing element of the material. Figure A.3 shows atom projected band structure of a monolayer $PtSe_2$ with SOC.

Orbital projected band structure

The orbital projected band structure is calculated and plotted using the same methodology as atom projected band structure. In this case the sum is done over the orbitals. There are couple other options that can be used for the visualization. The orbital projected band structure can be visualized as contribution from s, p and d orbitals. Also, the

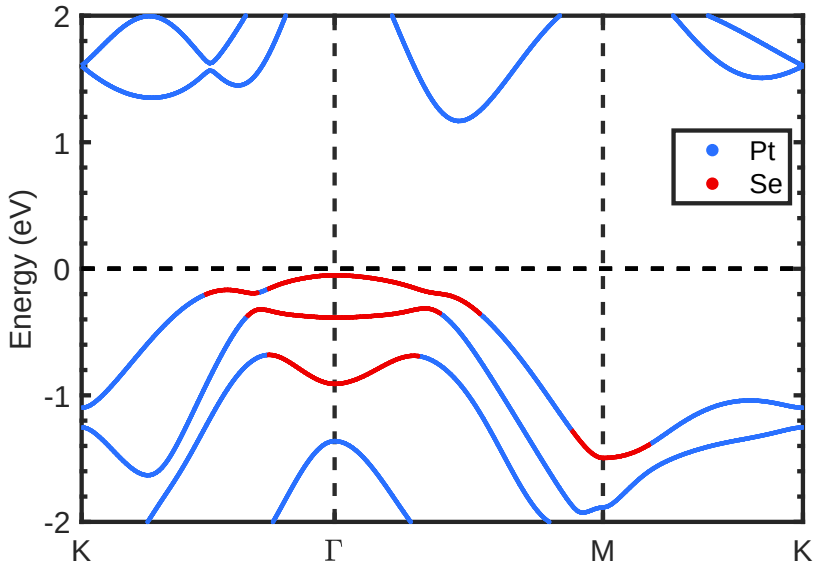

Figure A.3: Atom projected band structure of monolayer $PtSe_2$ using the library. The figure shows major contribution from a element at each k-point of the band structure.

library can breakdown contribution from p and d orbitals and visualize the data separately. For p-orbital the contribution of p_x and p_y orbitals or σ-bonds are plotted in one color and contribution from p_z or π-bonds are plotted in another color. For d-orbital the t_{2g} and e_g states are plotted in different colors. Figure A.4 shows atom projected band structure of a monolayer $PtSe_2$ with SOC.

A.5.2 Density of states (DOS)

Total density of states

The library can visualize total density of states as shown in Figure A.5. From the inputs, it can identify the physics included in the calculation and read the data accordingly. For example, if the calculation is spin-polarized, the library can plot the spin-up and spin-down differently. Usually DOS calculations are done separately from a band structure

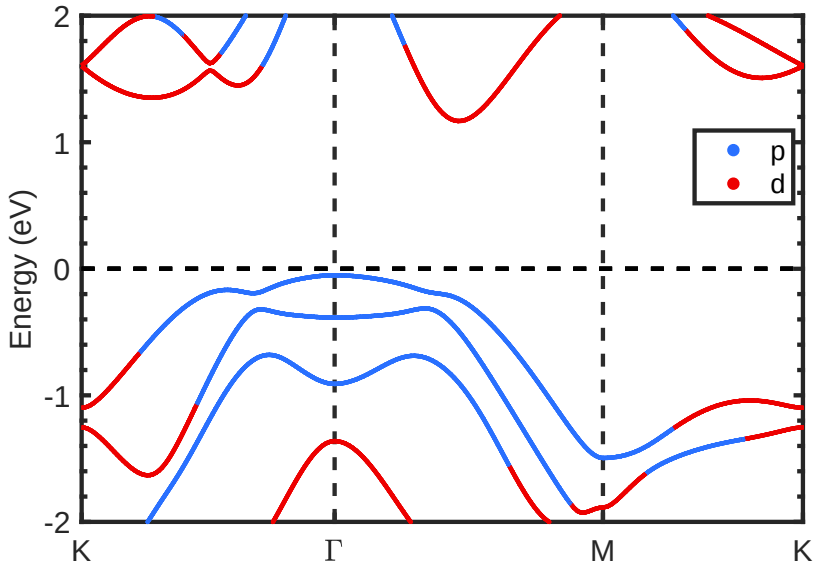

Figure A.4: Orbital projected band structure of monolayer $PtSe_2$ using the library. Like the atomic projection, orbital projection shows major contribution from an orbital at each k-point of the band structure.

calculation. For DOS, the calculation needs to be done on the whole Brillouin zone and the convergence as a function of k-points needs to be checked carefully.

Atom projected density of states

The library can also visualize atom projected DOS. An example plot is shown in Figure A.6. Compared to atom projected band structure, atom projected DOS contains more insight as the calculation is done on the whole Brillouin zone rather than a path along Brillouin zone.

Orbital projected density of states

The library can be used to visualize orbital projected DOS as shown in Figure A.7. For now, the orbital projected DOS separates contribution of the $s-$, $p-$ and $d-$ orbitals

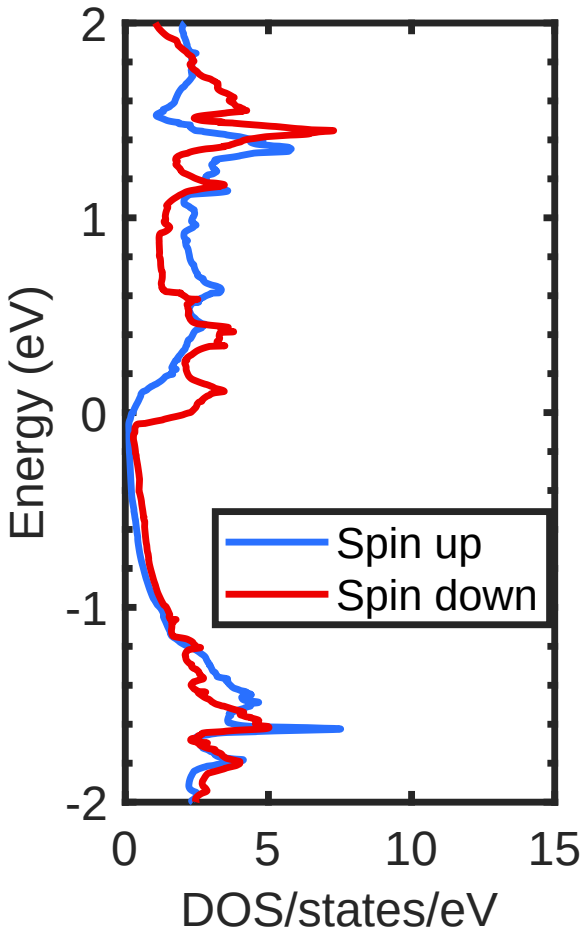

Figure A.5: Total DOS of an antiferromagnetic CrSb plotted by the library. The spin up and down components of the DOS are plotted with different colors.

separately. The library has another mode where the contribution of different d-orbital is plotted.

A.6 Effective mass calculation

Effective mass (m*) is an intrinsic property of a material that defines slope of the conduction or valance band minima. Electronic transport within a material is strongly dependent on the effective mass of a material. Effective mass can be determined from the

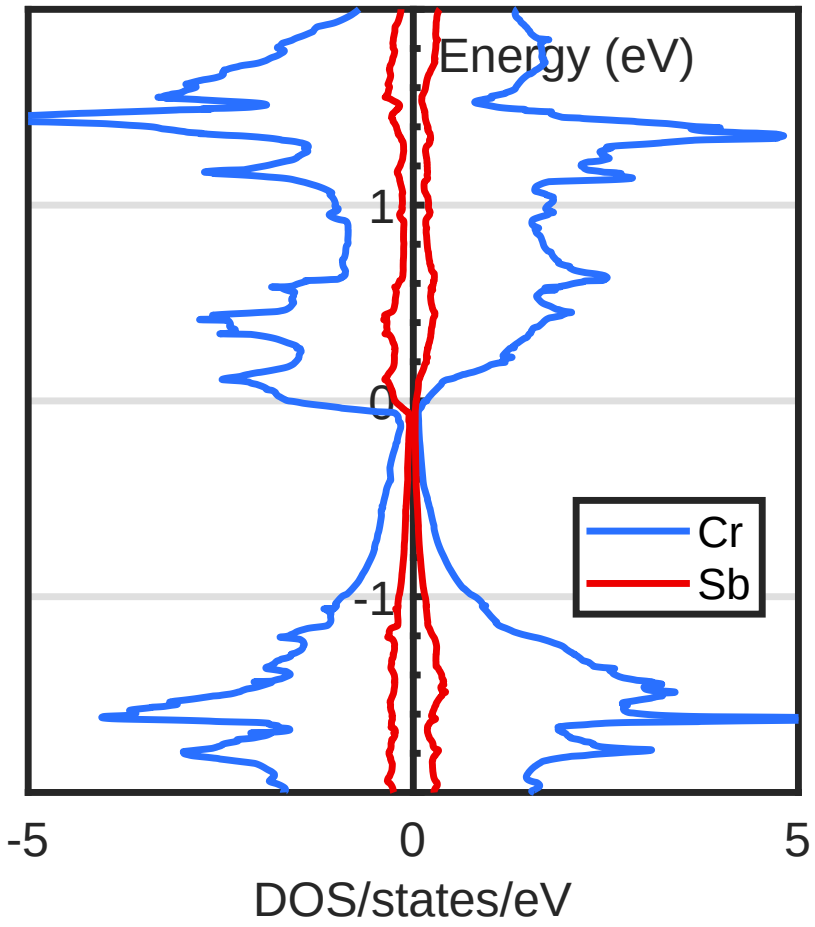

Figure A.6: Atom projected DOS of an antiferromagnetic CrSb is plotted by the library. The contribution of each atom to the DOS as a function of energy is shown separately.

band structure. The band edge of a semiconducting material is usually parabolic. This parabolic dispersion can be fitted to a second order polynomial to extract the effective mass. Effectively the effective mass can be defined as: $\frac{1}{m*} = \frac{1}{\hbar^2}\frac{\partial^2 E}{\partial k^2}$. To verify the order of the fitted polynomial, the dispersion can be fitted to 4^{th} or 6^{th} order polynomial. If the residuals are close to zero, then the dispersion is parabolic.

Effective mass is a tensor for a material. Also in a band minima, the effective mass is calculated in longitudinal and transverse direction. Usually the longitudinal direction is along k_x and the transverse direction is perpendicular to the k_x. If the mass along

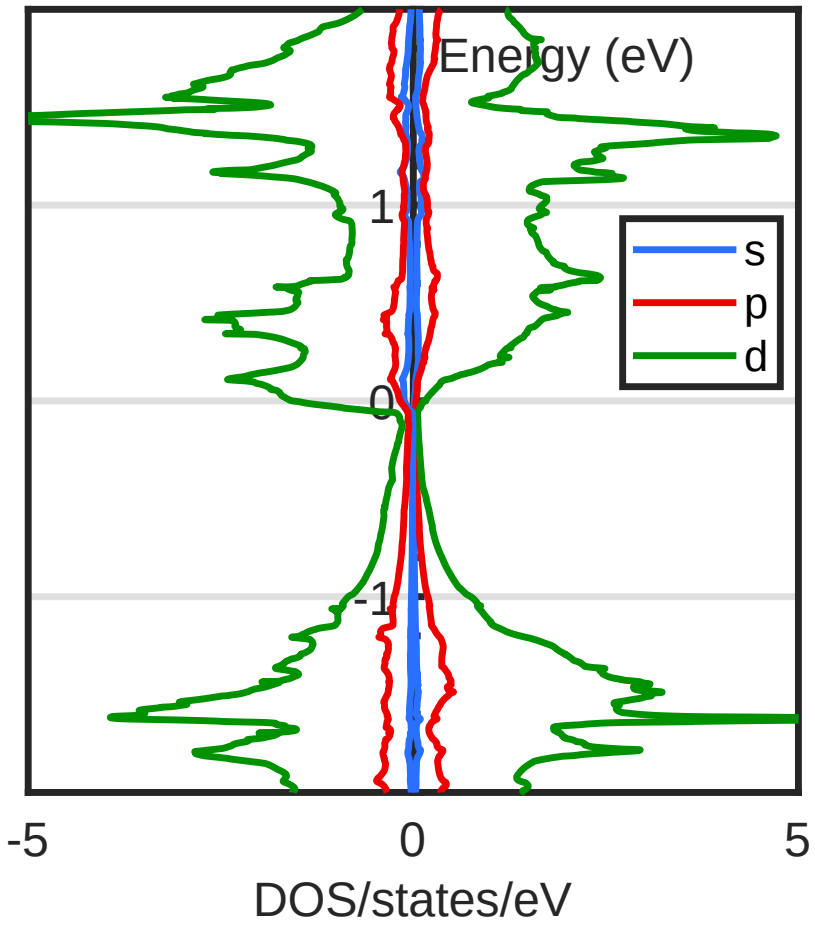

Figure A.7: Orbital projected DOS of antiferromagnetic CrSb. The contribution of $s-$, $p-$, and $d-$ orbital to the DOS as a function of energy is shown with separate colors.

longitudinal and transverse direction for conduction or valance band is same, the mass for that band is called isotropic. For an isotropic material the transport along either direction is same. If the masses are not same along the longitudinal and transverse direction, then the material is anisotropic and the transport along the directions will be different.

The effective mass can be calculated in two ways. One is to directly calculate from band structure. Another is to do a dense E-k calculation along the longitudinal and transverse direction.

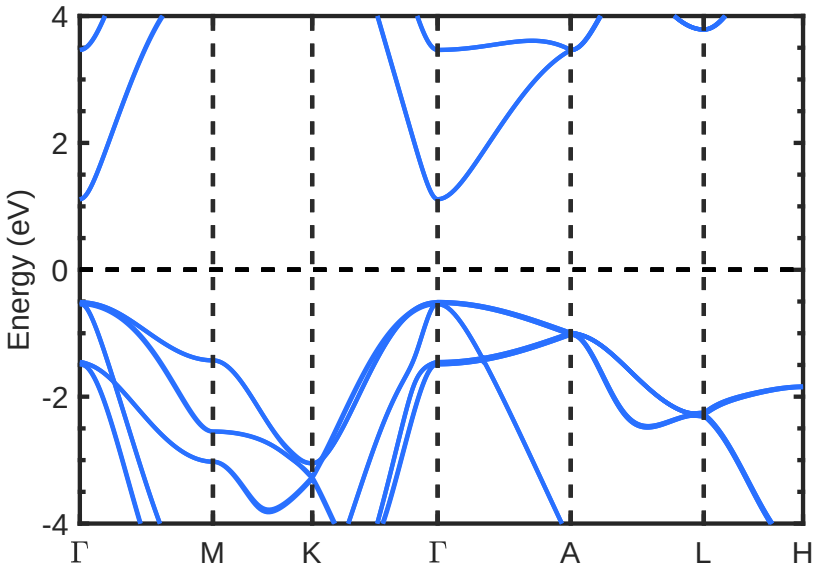

Figure A.8: Calculated band structure of bulk GaN.

```
Energy difference from VBM: 79.7meV

Effective mass of VB along kx direction :
   Using polynomial of order 2: 1.9612
   Using polynomial of order 4: 2.0249
   Using polynomial of order 6: 1.8550


Energy difference from VBM: 69.1meV

Effective mass of VB along ky direction :
   Using polynomial of order 2: 2.2635
   Using polynomial of order 4: 2.1163
   Using polynomial of order 6: 1.8718


Energy difference from CBM: 89.8meV

Effective mass of CB along kx direction :
   Using polynomial of order 2: 0.1580
   Using polynomial of order 4: 0.1506
   Using polynomial of order 6: 0.1506


Energy difference from CBM: 89.8meV

Effective mass of CB along ky direction :
   Using polynomial of order 2: 0.1580
   Using polynomial of order 4: 0.1506
   Using polynomial of order 6: 0.1506
```

Figure A.9: A screenshot of the output of calculated in-plane effective mass.

A.6.1 Generic effective mass

The generic effective mass is calculated from a band structure calculation. For the generic calculation of effective mass, three inputs are required. One is the threshold to

```
Energy difference from VBM: 67.0meV

Effective mass of VB along kz direction :
   Using polynomial of order 2: 2.2421
   Using polynomial of order 4: 2.1895
   Using polynomial of order 6: 2.1985


Energy difference from CBM: 724.5meV

Effective mass of CB along kz direction :
   Using polynomial of order 2: 0.2045
   Using polynomial of order 4: 0.1531
   Using polynomial of order 6: 0.1406
```

Figure A.10: A screenshot of out of plane effective mass calculation.

cut-off the band. Usually it's in order of kT, 35meV. The band minima will be fitted to 2^{nd}, 4^{th} and 6^{th} order polynomial to make sure there are no residues for higher order fits. For some cases the band minima or maxima are split due to spin orbit coupling (SOC) effect. If the splitting is higher than a given threshold value, then the library calculates effective mass for both bands.

A.6.2 Accurate effective mass calculation

Generate k-points

For an accurate effective mass calculation, a separate band structure calculation is needed. The library can be used to generate the line of k-points. In this mode, the library identifies the band minima and generates k-points along the longitudinal and transverse

direction. For this mode, a threshold cut-off can be given. The library fits the dispersion up to the threshold energy. The library can write the k-point path in two formats. The default format is to write the file as KPOINTS file as required for vasp calculations. Another is to write as a mat file.

Calculate effective mass

In this mode, the library reads the calculation output done with KPOINTS provided by the earlier mode and calculates the effective mass. The functionality of this mode is similar to the generic calculation. As the dispersion path is along the longitudinal and transverse direction with dense k-points along the direction, the calculation output is more accurate in this case. An example output for the in-plane and out-of-plane effective mass calculation is shown in Figure A.9 and Figure A.10. Figure A.8 shows the band structure of bulk GaN.

A.6.3 Effective mass of semiconducting material of a heterostructure

A heterostructure is formed when two materials are stacked. In a FET, a metallic material is stacked over a semiconducting material to form a contact. This can be done in DFT to observe changes in the material properties. The curvature of the VBM or CBM of a semiconducting material can be affected when stacked with a metallic layered material. This can be quantified by calculating the effective mass of the pristine material and the mass of the semiconducting material in a heterostructure.

Generate k-points

In this mode, the library identifies the minima and maxima contributed from the material which is provided by user. From the minima or maxima, the library generates k-points along the longitudinal and transverse direction within the threshold provided by user.

Calculate effective mass

In this mode, the library reads the calculation output done using KPOINTS provided by the earlier mode and calculates the effective mass. The functionality of this mode is similar to the accurate calculation. In this case the library calculates the effective mass for the band contributed by the material provided by user. Figure A.11 shows atom projected band structure of a $MoTe_2$-$TaSe_2$ heterostructure. Here $TaSe_2$ is a metallic material, while $MoTe_2$ is semiconducting. The library is used to calculate effective mass of the valance and conduction band contributed by Mo. The calculated effective masses are tabulated in Table A.2.

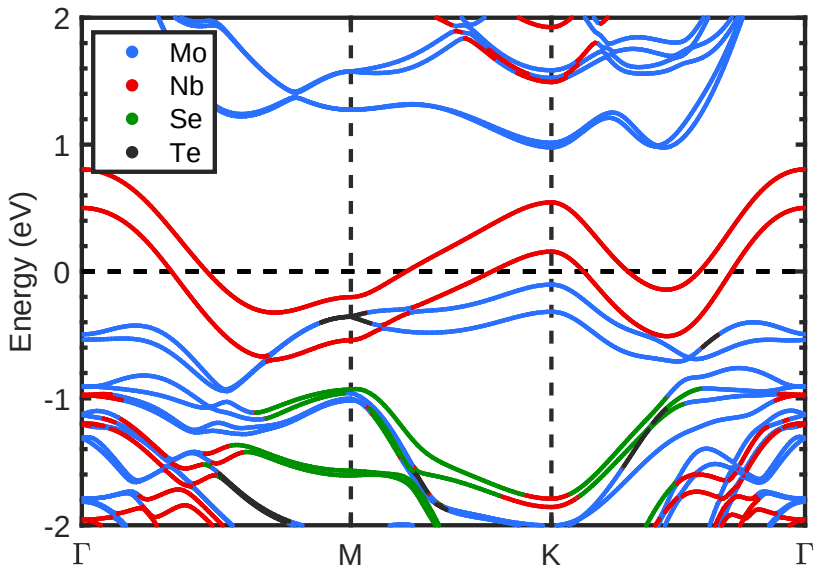

Figure A.11: Atom projected band structure of a $MoTe_2$-$TaSe_2$ heterostructure.

Material	Valance band		Conduction band	
	m_l^*	m_t^*	m_l^*	m_t^*
$MoTe_2$	0.6333	0.6332	0.5394	0.5381
$NbSe_2$-$MoTe_2$	0.6670	0.6661	0.8484	0.6989
% change	5.32	5.19	57.29	29.88

Table A.2: Effective masses of an isolated monolayer $MoTe_2$ and that of a $NbSe_2$-$MoTe_2$ heterostructure.

Appendix B

Python for streamlining structure creation and ab-initio calculations

Python can be a powerful tool to streamline structure creation and manipulation. Also DFT calculations can be managed using python. Two libraries Atomic Simulation Environment (ASE) and `pymatgen` can be used for this purpose. Due to low barrier and ease of use, ASE will be discussed further on.

ASE can be installed using default package manager of python, pip. The command for installing pip is,

```
pip install ase
```

B.1 Configuration

For using ASE to run VASP calculation, some configuration is needed. Two environment variables are need to be set for this. One is `VASP_COMMAND` which is the VASP

command to use in a supercomputer environment. Another is the `VASP_PP_PATH`, which points to a directory containing the pseudopotential files.

Usually the directory containing the pseudopotential files are not modified often and can be added to the `.bashrc` file. This can be done using,

```
export VASP_PP_PATH=$HOME/vasp.pps
```

On the contrary, depending on the calculation, different VASP executable can be used. For example, in a calculation where spin-orbit coupling (SOC) is incorporated, the executable `vasp_ncl` is used. Whereas for calculation without SOC, `vasp` is used. Hence the best place to set the variable `VASP_COMMAND` is in the job script. In an environment where slurm job scheduler is used, an example job script can be,

Listing B.1: Slurm job script

```
#!/bin/bash
#SBATCH --nodes=1
#SBATCH --tasks-per-node=24
#SBATCH -t 47:55:00
#SBATCH -o output.log
#SBATCH -e error.log
#SBATCH --job-name="job name"
#SBATCH -p compute

source activate ase

processors=$(( $SLURM_NNODES * $SLURM_NTASKS_PER_NODE ))

```

```
exe=`which com_vasp_std`
export VASP_COMMAND="mpirun -np $processors -genv I_MPI_FABRICS shm:ofa $exe"

echo "Starting job $SLURM_JOBID with $processors processors..."

python <script_name>
```

B.2 Structure manipulation

A cubic bulk structure of Co with lattice constant of 3.6 Å can be created using,

```
from ase.build import bulk
a1 = bulk('Co', 'fcc', a=3.6)
```

Also common surfaces can be created. For example a [111] surface of Co 4×4 surface with 4 atomic layers with a lattice constant of 3.6 Å can be created using,

```
from ase.build import fcc111
slab = fcc111('Co', size=(4,4,4), a=3.6, vacuum=10.0)
```

This command also adds 10 Å vacuum on both side of the surface. ASE can read VASP POSCAR files too. A POSCAR file can be read using,

```
import ase.io.vasp as vp
bulk = vp.read_vasp('PtSe2_bulk.vasp')
```

The POSCAR file reads,

Listing B.2: PtSe2_bulk.vasp

```
PtSe2_bulk
```

```
1.00000000000000
3.7670446069920076 -0.0000000000000013 -0.0000000000000001
-1.8835223034960036 3.2623563265822813 0.0000000000000010
0.0000000000000010 0.0000000000000003 4.6503534076770716
Pt Se
1 2
Direct
-0.0000000000000000 -0.0000000000000000 -0.0000000000000000
0.6666669999999968 0.3333330000000032 0.2750269337488745
0.3333330000000032 0.6666669999999968 0.7249730662511233

0.00000000E+00 0.00000000E+00 0.00000000E+00
0.00000000E+00 0.00000000E+00 0.00000000E+00
0.00000000E+00 0.00000000E+00 0.00000000E+00
```

The structure is read as an atoms object of ASE. and can be further manipulated. For example a 1T bulk $PtSe_2$ is read in the earlier example. Creating a monolayer from a bulk material is straightforward. Within ASE vacuum can be added to a bulk structure. Adding vacuum to the bulk structure creates a monolayer of the bulk material. This can be done by the following,

```
monolayer = bulk.copy()
monolayer.center(vacuum=10, axis=2)
vp.write_vasp('PtSe2_1L.vasp', monolayer, vasp5=True)
```

In the example above the bulk atoms object is copied into an object called moonolayer. Then a vacuum of 10 Åis added to the third axis of the c direction of the object. Finally the object is written as a POSCAR file in VASP5 format.

All the parameters of an atoms object like the unit cell or the coordinates of the atoms are available within the python environment. All these properties can be manipulated for specific purpose. For example, a 2H bulk structure has two atomic layers. Creating a monolayer requires removal of one atomic layer and then adding a vacuum. In the following example a 2H bulk MoS_2 POSCAR file will be read and a monolayer structure will be created.

```
import ase.io.vasp as vp
mos2_2h = vp.read_vasp('MoS2_2H.vasp')

positions = mos2_2h.get_positions()

# get mid point of the structure
half_z = ((max(positions[:,2]) - min(positions[:,2]))/2) + min(positions[:,2])

monolayer=mos2_2h.copy()

# delete atoms which has height less than half
del monolayer[[atom.index for atom in monolayer if atom.position[2]>=half_z]]

# add vacuum
monolayer.center(vacuum=10, axis=2)

vp.write_vasp('MoS2_1L.vasp', monolayer, vasp5=True)
```

The POSCAR file for the 2H MoS_2 is,

Listing B.3: MoS2_2H.vasp

```
MoS2_bulk
1.00000000000000
3.1885103817542433 -0.0000000009369568 -0.0000000000000000
-1.5942546919715344 2.7613301284994134 0.0000000000000000
0.0000000000000000 0.0000000000000000 12.4030213073455648
Mo S
2 4
Direct
0.6666669999999968 0.3333330000000032 0.2500000000000000
0.3333330000000032 0.6666669999999968 0.7500000000000000
0.3333330000000032 0.6666669999999968 0.1243982082183498
0.6666669999999968 0.3333330000000032 0.6243982082183500
0.3333330000000032 0.6666669999999968 0.3756017917816504
0.6666669999999968 0.3333330000000032 0.8756017917816500

0.00000000E+00 0.00000000E+00 0.00000000E+00
0.00000000E+00 0.00000000E+00 0.00000000E+00
0.00000000E+00 0.00000000E+00 0.00000000E+00
0.00000000E+00 0.00000000E+00 0.00000000E+00
0.00000000E+00 0.00000000E+00 0.00000000E+00
0.00000000E+00 0.00000000E+00 0.00000000E+00
```

B.3 DFT calculation using python

As discussed earlier, any DFT calculation within VASP involves several input files. Python can be used to streamline the simulations. In the following examples, usage of ASE for VASP calculation will be shown.

B.3.1 Convergence and relaxation

First step for DFT calculation of a new material involves the convergence check of the k-points and the energy cut-off of the plane waves.

K-points convergence of a material is done by doing a ground state energy calculation of a material with increasing number of k-points. In the following example, a bulk structure is read and a ground state energy calculation is done for a list of k-points. The final corresponding energy along with the k-points are tabulated in an output file. The convergence of the k-points can be decided from the output file. The following example shows use of ASE for k-points convergence of a material,

Listing B.4: k-points convergence

```
''' This script checks k-point convergence using vasp.
This script reads an input structure as the variable ins_poscar,
runs k-point convergence for each of the
k-point given in the kps list and tabulates them
in a file name given by variable out_summary.
'''

import numpy
import ase.io.vasp as vp
from ase.calculators.vasp import Vasp
from os import path, rename, remove
from shutil import *

ins_poscar='NbSe2_bulk_2H.vasp'
```

```
ins= vp.read_vasp(ins_poscar)
out_summary='summary_kpts.txt'

if path.isfile(out_summary):
    op=open(out_summary, 'a')
else:
    op=open(out_summary, 'w')
    op.write('kpoints summary created using ase\n')
    op.write('kpoint \t energy \n')

# list of k-points
kps = [4, 6, 8, 10, 12,14,16]

# VASP input parameters
calc = Vasp(prec = 'Accurate',
        pp = 'pbe',
        istart=0,
        ismear=1,
        sigma=0.05,
        lcharg=False,
        lwave=False,
        lreal = False,
        encut = 400.0,
        algo='Normal',
        nelm=200,
        ncore=11,
        ediff=1e-6,
```

```
42        ibrion=-1,
43        nsw=0,
44        nelmin=4,
45        ediffg=-0.01,
46        gamma=True)
47
48 print("Calculation output")
49 print("------------------")
50 print('kpoint energy ')
51
52
53 # Generate cell configurations
54 for kp in kps:
55
56   in2 = ins.copy()
57   calc.set(kpts = [kp,kp,kp/2])
58   in2.set_calculator(calc)
59   energ=in2.get_potential_energy()
60   op.write(' {:5d} {:8.4f} \n'.format(kp,energ))
61   print(' {:8d} {:8.2f} '.format(kp,energ))
62   fpath3 = 'vasp.kp.{:d}.out'.format(kp)
63
64   if path.isfile(fpath3):
65     remove(fpath3)
66
67   copyfile('vasp.out', fpath3)
68
```

```
69
70 op.close()
71 calc.clean()
72 print('\n\n Done')
```

Convergence of the energy cut-off for the plane waves is done in a similar way like k-points convergence. The only difference is that the energy cut-off is modified for each ground state energy calculations. The code for energy cut-off convergence reads,

Listing B.5: Energy cut-off convergence

```
1 ''' This script checks energy convergence using vasp.
2 This script reads an input structure as the variable ins_poscar,
3 runs energy convergence for each of the
4 encut given in the encuts list and tabulates them
5 in a file name given by variable out_summary.
6 '''
7
8 import numpy as np
9 import ase.io.vasp as vp
10 from ase.calculators.vasp import Vasp
11 from os import path, rename, remove
12 from shutil import *
13
14 ins_poscar='NbSe2_bulk_2H.vasp'
15 ins= vp.read_vasp(ins_poscar)
16 out_summary='summary_cutoff2.txt'
17
```

```
if path.isfile(out_summary):
    op=open(out_summary, 'a')
else:
    op=open(out_summary, 'w')
    op.write('encut file created using ase\n')
    op.write('encut \t energy \n')

# converged k-points
conv_kpt=[8, 8, 4]

# list of energies
encuts = [200, 250,300, 350, 400, 450, 500]


calc = Vasp(prec = 'Accurate',
       pp = 'pbe',
       istart=0,
       ismear=1,
       sigma=0.1,
       lcharg=False,
       lwave=False,
       lreal = False,
       algo='Normal',
       nelm=200,
       #ncore=12,
       ediff=1e-6,
       ibrion=-1,
```

```
45        nsw=0,
46        nelmin=4,
47        ediffg=-0.01,
48        kpts = conv_kpt,
49        gamma=True)
50
51 print("Calculation output")
52 print("------------------")
53 print('encut energy ')
54
55 # loop over list of energies
56 for e in encuts:
57
58   in2 = ins.copy()
59   calc.set(encut = e)
60   in2.set_calculator(calc)
61   energ=in2.get_potential_energy()
62   op.write(' {:5d} {:5.6f} \n'.format(e,energ))
63   print(' {:5d} {:5.4f} '.format(e,energ))
64   fpath3 = 'vasp.encut.{:d}.out'.format(e)
65
66   if path.isfile(fpath3):
67     remove(fpath3)
68
69   copyfile('vasp.out', fpath3)
70
71 op.close()
```

```
copyfile('POTCAR','potcar')

calc.clean()
```

After converged k-points and energy cut-off are found, the next step is to relax the structure. At this step, both the cell dimensions and the atomic coordinates are optimized to minimize the force between the atoms. Alternatively this step is also called volume relaxation of a structure. For this step VASP will be used as a force calculator and the BFGS optimized within ASE will be used to minimize the forces. The appropriate constraints are needed to be added to the atoms object. In this case both the unit cell and the atomic coordinates are modified to minimize forces. The `UnitCellFilter` within ASE imposes such constraints to the atoms object. The code below does volume relaxation on a 2H bulk $NbSe_2$ structure.

Listing B.6: Volume relaxation

```
''' This script does volume relaxation using vasp.
Reads an input structure from the given file name
and then based on the input parameters, runs
volume relaxation.

The force cutoff for stopping the relaxation
is provided by fmax parameter.

Snapshots of the relaxation is stored in file,
traj_<symbol>_vol_relaxed.traj which can be
viewed in ase-gui.
```

```
12
13 The relaxed structure is named as,
14 ase_<symbol>_vol_relaxed.vasp
15 '''
16
17 import numpy as np
18 import ase.io.vasp as vp
19 from ase.io import *
20 from ase.calculators.vasp import Vasp
21 from os import path, remove
22 from ase.optimize import BFGS as bfgs
23 from ase.constraints import UnitCellFilter as ucf
24 from ase.io.trajectory import Trajectory
25
26 np.set_printoptions(precision=2)
27
28 # name of input structure
29 ins_poscar='NbSe2_bulk_2H.vasp'
30
31
32 # force threshold on atoms
33 fmax = 1E-6
34
35 # maximum number of steps for the minimizer
36 steps = 150
37
38 # converged kpoints for the structure
```

```
kpt=8

# minimizer log file
logfile = 'relax.log'

# vasp parameters
calc = Vasp(prec = 'Accurate',
       pp = 'pbe',
       istart=0,
       ismear=0,
       sigma=0.1,
       lcharg=False,
       lwave=False,
       lreal = False,
       lorbit=11,
       encut = 400,
       algo='Normal',
       nelm=200,
       ivdw=1,
       ediff=1e-6,
       ibrion=-1,
       nsw=0,
       nelmin=4,
       ediffg=-0.01,
       kpts = [kpt,kpt,kpt/2],
       gamma=True)

```

```
66
67 print("Volume Relaxation using ASE")
68 print("----------------------------")
69
70 ins= vp.read_vasp(ins_poscar)
71
72 initial_pos = ins.get_positions()
73 initial_vol = ins.get_volume()
74 formula = ins.get_chemical_formula()
75
76 print('\n Initial volume: {:3.2f} A^3'.format(initial_vol))
77 print(' Initial Positions: ')
78
79 for p in initial_pos:
80     print(' \t\t{}'.format(p))
81
82 traj_str = 'traj_{}_vol_relax.traj'.format(formula)
83
84 if path.isfile(logfile):
85     remove(logfile)
86     print('\n Cleared logfile ({}).'.format(logfile))
87
88
89 # Generate cell configurations
90 in2 = ins.copy()
91
92 in2.set_calculator(calc)
```

```
93
94  sf = ucf(in2)
95
96  bfgs = bfgs(sf, logfile=logfile)
97
98  traj = Trajectory(traj_str, 'w', in2)
99
100 bfgs.attach(traj)
101
102 print('\n Running optimizer...')
103
104 bfgs.run(fmax=fmax, steps=steps)
105
106 print('\n Optimizations done.')
107
108 label_str = 'volume relaxed {}'.format(formula)
109 poscar_name = 'ase_{}_vol_relaxed.vasp'.format(formula)
110
111 vp.write_vasp(poscar_name, in2, label=label_str,
112             direct=False, sort=True, vasp5=True)
113
114 final_pos = in2.get_positions()
115 final_vol = in2.get_volume()
116
117 print('\n Final volume: {:3.2f} A^3'.format(final_vol))
118 print(' Final Positions: ')
119
```

```
for p in final_pos:
    print(' \t\t{}'.format(p))

diff_pos = final_pos - initial_pos

print('\n Change in volume: {:3.2f} A^3'.format(final_vol-initial_vol))
print(' Change in position: ')

for p in diff_pos:
    print(' \t\t{}'.format(p))

print('\n Stress on atoms in the final structure: ')

final_stress = calc.read_stress()

print('\t\t', end='')
for s in final_stress:
    print(' {:2.2E}'.format(s), end='')

calc.clean()

print('\n\n \t----- Done -----\n')
```

The code above assumes the material is a bulk layered 2D material. For materials that need incorporation of LDA+U parameters, the input parameters of the `Vasp` object needs to be modified accordingly.

B.3.2 Electronic structure calculation within PBE

After convergence and relaxation of a structure is to do electronic structure calculation using the relaxed structure and the converged parameters. For that, the first step is to calculate the charge density with the converged parameters. For the following codes, it is assumed that the relaxed structure is in `0.isif` directory and the file is named CONTCAR. The following code uses ASE to calculate the charge density of the structure. After the calculation, the charge density file, CHGCAR is copied to `1.scf` directory. The code reads,

Listing B.7: SCF calculation

```
''' This script does SCF calculation for a given
structure.

Reads an input structure from the directory name
given as variable isif_dir
and then based on the input parameters, does SCF
calculation.

When the calculation is done, the output files
are stored in a directory name given as
scf_dir variable.

The files stored in the scf_dir are:
CHGCAR, OSZICAR, OUTCAR and vasp.out
'''


```

```
import ase.io.vasp as vp
from ase.calculators.vasp import Vasp
from os import path, makedirs, rename, remove
from shutil import *
import subprocess

conv_kpt=[8,8,4]

scf_dir='1.scf'

isif_dir='0.isif'

calc = Vasp(prec = 'Accurate',
       pp = 'pbe',
       istart=0,
       ismear=0,
       sigma=0.1,
       lwave=False,
       lreal = False,
       encut = 400,
       algo='Normal',
       nelm=100,
       ediff=1e-8,
       ibrion=-1,
       nsw=0,
       nelmin=4,
       ediffg=-0.01,
```

```
45        kpts = conv_kpt,
46        gamma=True)
47
48 print("\n-----------------------------------------")
49 print("SCF calculation of Heterostructure using ASE")
50 print("-----------------------------------------")
51
52 poscar_path=path.join(isif_dir,'CONTCAR')
53 l_scf_dir= path.join(scf_dir)
54
55 if not path.exists(l_scf_dir):
56     makedirs(l_scf_dir)
57
58 b=vp.read_vasp(poscar_path)
59 in2 = b.copy()
60 in2.set_calculator(calc)
61
62 energy = in2.get_potential_energy()
63
64 fpath1 = '{}/vasp.out'.format(l_scf_dir)
65 copyfile('vasp.out',fpath1)
66
67 fpath3 ='{}/OSZICAR'.format(l_scf_dir)
68 rename('OSZICAR',fpath3)
69
70 fpath4 ='{}/OUTCAR'.format(l_scf_dir)
71 rename('OUTCAR',fpath4)
```

```
72
73 fpath5 ='{}/CHGCAR'.format(l_scf_dir)
74 rename('CHGCAR',fpath5)
75
76 print('\n\n \t----- SCF Done -----\n')
```

In a band structure calculation, the charge density is read from the SCF step and the eigenvalues between high symmetry points. In the following code the charge density file `CHGCAR` is copied from `1.scrf` directory and used for band structure calculation. The relaxed structure is read from `0.isif` directory. For materials with commonly known Brillouing zone, a string for the band structure calculation path and number of points for the calculation is given. Alternatively a list of high symmetry points can also be given. After the calculation, necessary files are copied in `2.ek` directory.

Listing B.8: Band structure calculation

```
1  ''' This script calculates band structure for
2  a given structure. Uses converged charge density
3  from the SCF step for the calculation.
4
5  Reads an input structure from the directory name
6  given as variable isif_dir,
7  creates symlink of the CHGCAR file from ‘soc_scf_dir‘
8  and based on the input parameters, does band structure
9  calculation.
10
11
```

```
The path for the band structure calculation
is given by ‘bs_str‘ assuming the Brillouin
zone is hexagonal. k-points per line is given
by ‘kp_per_line‘. The path for the band structure
is created accordingly.

When the calculation is done, the output files
are stored in a directory name given in ‘soc_ek_dir‘.

The files stored in the soc_ek_dir are:
vasprun.xml, OUTCAR and vasp.out.
'''

import ase.io.vasp as vp
from ase.calculators.vasp import Vasp
from os import path, makedirs, rename, remove,symlink
from ase.dft.kpoints import get_special_points, bandpath
import numpy as np
from shutil import *

kp_per_line=51 # points between two high symmetry points
bs_str = 'GMKG' # band structure calculation path
soc_ek_dir='2.ek'
soc_scf_dir='1.scf'
isif_dir='0.isif'

calc = Vasp(prec = 'Accurate',
```

```
        pp = 'pbe',
        istart=0,
        ismear=1,
        sigma=0.1,
        lwave=False,
        lcharg=False,
        lreal = False,
        icharg=11,
        lorbit=11,
        encut = 550,
        algo='Normal',
        nelm=100,
        ediff=1e-6,
        ibrion=-1,
        nsw=0,
        nelmin=4,
        ediffg=-0.01,
        reciprocal=True,
        )

print("\n-----------------------------------------")
print("E-k calculation of Heterostructure using ASE")
print("-----------------------------------------")


poscar_path=path.join(isif_dir,'CONTCAR')
l_scf_dir= path.join(soc_scf_dir,'CHGCAR')
```

```
l_ek_dir=path.join(soc_ek_dir)

if path.islink('CHGCAR') or path.isfile('CHGCAR'):
    remove('CHGCAR')

symlink(l_scf_dir,'CHGCAR')

if not path.exists(l_ek_dir):
    makedirs(l_ek_dir)

b=vp.read_vasp(poscar_path)

in2 = b.copy()

points = get_special_points('hexagonal', in2.cell)
GMK = [points[k] for k in bs_str]

no_kpts=kp_per_line*(len(GMK)-1)

temp_kpts, x, X = bandpath(GMK, in2.cell, no_kpts)

del x
del X

final_shape = temp_kpts.shape

kpts=np.zeros((final_shape[0],4))
```

```
93
94  wt = np.ones((no_kpts,1), dtype=np.float64)
95
96  kpts[:,:-1]=temp_kpts
97  kpts[:,-1:] = wt
98
99  del temp_kpts
100 del wt
101
102 calc.set(kpts=kpts,
103     )
104
105 in2.set_calculator(calc)
106
107 energy = in2.get_potential_energy()
108
109 fpath2 ='{}/vasprun.xml'.format(l_ek_dir)
110 rename('vasprun.xml',fpath2)
111
112 fpath1 = '{}/vasp.out'.format(l_ek_dir)
113 copyfile('vasp.out',fpath1)
114
115 fpath4 ='{}/OUTCAR'.format(l_ek_dir)
116 rename('OUTCAR',fpath4)
117
118 calc.clean()
119
```

```
120 print('\n\n \t----- E-k Done -----\n')
```

The density of states (DOS) calculation follow similar logic as band structure calculation. The relaxed structure and charge density is read from `0.isif` and `1.scf` directory, respectively. Only that in a DOS calculation, the calculation is done in a denser grid of k-points. For this denser grid, the charge density is interpolated from the converged charge density of the SCF calculation. Around the Fermi energy, the DOS is calculated within a resolution of 1 meV. The energy window for the DOS calculation can be given by the user. The DOS calculation needs careful verification of convergence for a number of k-points grid. For each of the calculation, the script creates a directory name in the form `dos`< `number of kpoints in one direction`>. For example, for a k-points grid of 24×24×24, the directory name will be `dos24`.

Listing B.9: Density of States calculation

```
1  ''' This script calculates DOS with LDA+U for
2  a given structure. Uses converged charge density
3  from the SCF step with SOC for the calculation.
4
5  Reads an input structure from the directory name
6  given as variable isif_dir,
7  creates symlink of the CHGCAR file from ‘sp_scf_dir‘
8  and based on the input parameters, does DOS
9  calculation.
10
11 When the calculation is done, the output files
12 are stored in a directory dos<number_of_kpoints>.
```

```
13
14 The script read the Fermi level from
15 the OUTCAR of SCF directory which is
16 given as ‘soc_scf_dir‘. The DOS calculation is done
17 from ‘below_fermi‘ to ‘over_fermi‘ with the ‘resolution‘
18 given in meV.
19
20 The files stored in the dos<number_of_kpionts> are:
21 vasprun.xml, OUTCAR and vasp.out.
22 '''
23
24 import ase.io.vasp as vp
25 from ase.calculators.vasp import Vasp
26 from os import path, makedirs, rename, remove,symlink
27 import numpy as np
28 from shutil import *
29
30 # no of kpoints
31 kpoints=18
32
33 # value of dos minimum and maximum energy in eV.
34 below_fermi=3.5
35 over_fermi=2.5
36
37 # resolution of the DOS in meV
38 resolution = 1
39
```

```
dos_kpt=[kpoints, kpoints, kpoints]

soc_scf_dir='1.sp.scf'

isif_dir='0.isif'

calc = Vasp(prec = 'Accurate',
       pp = 'pbe',
       istart=0,
       ismear=-5,
       lwave=False,
       lcharg=False,
       lreal = False,
       icharg=11,
       lorbit=11,
       ncore = 11,
       encut = 400,
       algo='Normal',
       nelm=100,
       ediff=1e-6,
       ibrion=-1,
       nsw=0,
       nelmin=2,
       ediffg=-0.01,
       reciprocal=True,
       kpts = dos_kpt,
       gamma=True,
```

```
67        )
68
69 print("\n------------------------")
70 print("DOS calculation using ASE")
71 print("------------------------")
72
73 E_f=None
74 for line in open(path.join(soc_scf_dir,'OUTCAR'),'r'):
75     if line.rfind('E-fermi') > -1:
76         E_f = float(line.split()[2])
77
78 if E_f is None:
79     raise ValueError('Fermi value not found')
80 else:
81     print('\nFermi level is at {:2.2f}eV.'.format(E_f))
82
83
84 emin = E_f - below_fermi
85 emax = E_f + over_fermi
86 resolution = resolution/1000
87
88 nedos = int( ((emax-emin)/resolution) + 1)
89
90 print('Running on {} points from {:2.2f}eV to {:2.2f}eV.'.format(nedos,emin,emax))
91
92 poscar_path=path.join(isif_dir,'CONTCAR')
93
```

```
l_scf_dir= path.join(soc_scf_dir,'CHGCAR')

if path.islink('CHGCAR') or path.isfile('CHGCAR'):
    remove('CHGCAR')

symlink(l_scf_dir,'CHGCAR')

l_ek_dir='dos{}'.format(kpoints)

if not path.exists(l_ek_dir):
    makedirs(l_ek_dir)

b=vp.read_vasp(poscar_path)

in2 = b.copy()



calc.set(emin=emin,
         emax=emax,
         nedos=nedos,
    )

in2.set_calculator(calc)

energy = in2.get_potential_energy()

fpath2 ='{}/vasprun.xml'.format(l_ek_dir)
```

```
121 rename('vasprun.xml',fpath2)
122
123 fpath1 = '{}/vasp.out'.format(l_ek_dir)
124 copyfile('vasp.out',fpath1)
125
126 fpath4 ='{}/OUTCAR'.format(l_ek_dir)
127 rename('OUTCAR',fpath4)
128
129 fpath4 ='{}/POTCAR'.format(l_ek_dir)
130 rename('POTCAR',fpath4)
131
132 calc.clean()
133
134 print('\n\n \t----- DOS Done -----\n')
```

B.3.3 Electronic structure calculations with HSE

A HSE calculation is usually done using wavefunctions of a SCF step. The following code shows how python is used to do a HSE SCF calculation using wavefunctions of an SCF calculation. Also the script stores the k-points of the irreducible Brillouin zone (IBZ) in a text file that will be used for band structure calculation with HSE. The code reads,

Listing B.10: HSE SCF calculation

```
1 ''' This script does SCF calculation with SOC and
2 HSE for a given structure. Reads the wavefunctions
3 from the SCF calculation with SOC.
4
```

```
Reads an input structure from the directory name
given as variable ‘isif_dir‘,
copies ‘WAVECAR‘ file from directory name given
as ‘soc_scf_dir‘ variable
and based on the input parameters, does SCF
calculation.

When the calculation is done, the output files
are stored in a directory name given as
‘hse_scf_dir‘ variable. Also stores ‘k-points‘ and ‘weights‘
of the irreducible Brillouin zone in
‘ibzkp.txt‘ and ‘ibzkp_wt.txt‘ files, respectively.
This is used later for band structure calculation with HSE.

Optionally it can process the ‘LOCPOT‘ file
to generate data for local potential plot.

The files stored in the ‘hse_scf_dir‘ are:
‘CHGCAR‘, ‘OUTCAR‘, ‘vasp.out‘ and ‘WAVECAR‘
file which is required for HSE band structure
calculations.
'''

import ase.io.vasp as vp
from ase.calculators.vasp import Vasp
from os import path, makedirs, rename, remove
import subprocess
```

```
import numpy as np
from shutil import copyfile

# initial moment
mom=1

conv_kpt=[6,6,1]

hse_scf_dir='5.hse.scf'

soc_scf_dir='3.soc.scf'

isif_dir='0.isif'


calc = Vasp(prec = 'Accurate',
       xc = 'hse06',
       istart=1,
       ismear=1,
       sigma=0.1,
       lcharg=False,
       lreal = False,
       encut = 400,
       kpar=2,
       nelm=150,
       isym=0,
       ediff=1e-6,
```

```
59        ibrion=-1,
60        nsw=0,
61        nelmin=4,
62        ediffg=-0.01,
63        lhfcalc=True,
64        lsorbit=True,
65        hfscreen=0.2,
66        ialgo=53,
67        algo='DAMPED',
68        time=0.4,
69        precfock='Normal',
70        aexx=0.25,
71        lmaxmix=4,
72        nsim=4,
73        kpts = conv_kpt,
74        gamma=True)
75
76 print("\n---------------------------------------------")
77 print("HSE-SCF calculation of Heterostructure using ASE")
78 print("---------------------------------------------")
79
80
81 hse_scf_dir_adr=path.join(hse_scf_dir)
82 relax_dir_adr=path.join(isif_dir)
83 scf_dir_adr=path.join(soc_scf_dir,'WAVECAR')
84 poscar_path=path.join(isif_dir,'CONTCAR')
85 het = vp.read_vasp(poscar_path)
```

```
copyfile(scf_dir_adr,'WAVECAR')
in2 = het.copy()
magmom=np.ones(len(in2)*3)*mom
calc.set(magmom=magmom)
in2.set_calculator(calc)
energy = in2.get_potential_energy()

ibzkp_wts=calc.get_k_point_weights()
ibzkp=calc.get_ibz_kpoints()

if not path.exists(hse_scf_dir_adr):
    makedirs(hse_scf_dir_adr)

ibzkp_str=path.join(hse_scf_dir_adr,'ibzkp.txt')
ibzkp_wt_str=path.join(hse_scf_dir_adr,'ibzkp_wt.txt')
np.savetxt(ibzkp_str,ibzkp)
np.savetxt(ibzkp_wt_str,ibzkp_wts)

fpath1 = '{}/vasp.out'.format(hse_scf_dir_adr)
rename('vasp.out',fpath1)

fpath4 ='{}/OUTCAR'.format(hse_scf_dir_adr)
rename('OUTCAR',fpath4)

fpath4 ='{}/WAVECAR'.format(hse_scf_dir_adr)
rename('WAVECAR',fpath4)

```

```
calc.clean()

print('\n\n \t----- Done -----\n')
```

The band structure calculation with HSE is done using the wavefunctions for the HSE SCF calculation. For this calculation the k-points needs to have the IBZ k-points first and the k-points of along the high-symmetry points appended after that. The script reads the IBZ k-points of the HSE SCF calculation and adds the high symmetry points as discussed in the band structure calculation earlier.

Listing B.11: HSE band structure calculation

```
''' This script calculates band structure with SOC and HSE for
a given structure. Uses converged charge density
from the SCF step with SOC for the calculation.

Reads an input structure from the directory name
given as variable `isif_dir`,
creates symlink of the `WAVECAR` file from `hse_scf_name`,
and based on the input parameters, does band structure
calculation.

The `k-points` for the irreducible Brillouin zone (IBZ)
is read from `hse_scf_name` directory and added
to the `KPOINTS` file.

The path for the band structure calculation
is given by `bs_str` assuming the Brillouin
```

```
zone is hexagonal. ‘k-points‘ per line is given
by ‘kp_per_line‘. These ‘k-points‘ are appended
after the ‘k-points‘ of the IBZ.

When the calculation is done, the output files
are stored in a directory name given in ‘soc_ek_dir‘.

The files stored in the ‘soc_ek_dir‘ are:
‘vasprun.xml‘, ‘OUTCAR‘ and ‘vasp.out‘.
'''

import ase.io.vasp as vp
from ase.calculators.vasp import Vasp
from os import path, makedirs, rename, remove, symlink
from ase.dft.kpoints import get_special_points, bandpath
import subprocess
import numpy as np
from shutil import copyfile

kp_per_line=51
bs_str = 'GMKG'

# initial moment
mom=1

hse_ek_name='6.hse.ek'
hse_scf_name='5.hse.scf'
```

```
relax_name='0.isif'


calc = Vasp(prec = 'Accurate',
       xc = 'hse06',
       istart=1,
       ismear=0,
       sigma=0.1,
       lcharg=False,
       lwave=False,
       lreal = False,
       lorbit=11,
       algo='All',
       kpar=4,
       nelm=150,
       ncore=24,
       nbands=50,
       isym=0,
       ediff=1e-6,
       ibrion=-1,
       nsw=0,
       nelmin=4,
       ediffg=-0.01,
       lsorbit=True,
       lhfcalc=True,
       hfscreen=0.2,
       time=0.4,
       precfock='Normal',
```

```
71        aexx=0.25,
72        lmaxmix=4,
73        nsim=4,
74        reciprocal=True)
75
76 print("\n-----------------------------------------------")
77 print("HSE-Ek calculation of Heterostructure using ASE")
78 print("-----------------------------------------------")
79
80 hse_ek_dir=path.join(hse_ek_name)
81 hse_scf_dir=path.join(hse_scf_name)
82 relax_dir_adr=path.join(relax_name)
83 poscar_str= path.join(relax_dir_adr,'CONTCAR')
84 het = vp.read_vasp(poscar_str)
85 in2 = het.copy()
86 ibzkp_str=path.join(hse_scf_dir,'ibzkp.txt')
87 ibzkp_wt_str=path.join(hse_scf_dir,'ibzkp_wt.txt')
88 ibzkp=np.loadtxt(ibzkp_str)
89 ibzkp_wt=np.loadtxt(ibzkp_wt_str)
90 kpts1=np.zeros((len(ibzkp),4))
91 kpts1[:,:-1] = ibzkp
92 kpts1[:,-1:] = ibzkp_wt.reshape(len(ibzkp_wt),1)
93
94 del ibzkp
95 del ibzkp_wt
96
97 points = get_special_points('hexagonal', in2.cell)
```

```
GMK = [points[k] for k in bs_str]
no_kpts=kp_per_line*len(GMK)
temp_kpts, x, X = bandpath(GMK, in2.cell, no_kpts)

del x
del X

temp_shape = temp_kpts.shape
kpts2=np.zeros((temp_shape[0],4))
wt = np.zeros((no_kpts,1), dtype=np.float64)
kpts2[:,:-1]=temp_kpts
kpts2[:,-1:] = wt
kpts=np.vstack((kpts1,kpts2))

del kpts2
del temp_kpts
del wt

magmom=np.ones(len(in2)*3)*mom
calc.set(kpts=kpts,
       magmom=magmom,
       )

wcar_dir=path.join(hse_scf_dir,'WAVECAR')

if path.islink('WAVECAR'):
   remove('WAVECAR')
```

```
125
126 symlink(wcar_dir,'WAVECAR')
127 in2.set_calculator(calc)
128 energy = in2.get_potential_energy()
129
130 if not path.exists(hse_ek_dir):
131     makedirs(hse_ek_dir)
132
133 fpath1 = '{}/vasp.out'.format(hse_ek_dir)
134 rename('vasp.out',fpath1)
135
136 fpath4 ='{}/OUTCAR'.format(hse_ek_dir)
137 rename('OUTCAR',fpath4)
138
139 fpath4 ='{}/vasprun.xml'.format(hse_ek_dir)
140 rename('vasprun.xml',fpath4)
141
142 calc.clean()
143
144 print('\n\n \t----- Done -----\n')
```

B.3.4 Nudged elastic band (NEB) calculations

The nudged elastic band (NEB) calculation using VASP requires an initial and final structure. The calculation needs an initial and final structure structure. A script provided by Henkelman group can be used to create images in between the initial and final structure. Each of these images need to be put in a different directory. These steps need

to be done before the calculation is started. The script below can do all the steps before the calculation given the name of the initial and final structure and the number of images to create in between. This script assumes that the scripts provided by Henkelman group is added to the `PATH` variable.

Listing B.12: Nudged elastic band calculation

```
''' This script does nudged elastic band (NEB) calculation.

Reads the initial and final structure from 'initial' and
'final', creates 'nimages' number of intermediate images
using 'nebmake.pl' provided by VTST package and runs
NEB calculation from the given input parameters.

Uses the default NEB module of vasp.

Also creates some dummy files to avoid errors.
'''

from ase.calculators.vasp import Vasp
import ase.io.vasp as vp
from ase.io import *
import subprocess
from shutil import *
from os import path

# dummy structure ot run vasp
dummy = vp.read_vasp('start.vasp')
```

```
22
23 # converged kpoints for the structure
24 conv_kpt=[2, 2, 1]
25
26 # number of images
27 nimages=7
28
29 # initial and final POSCAR name
30 initial='start.vasp'
31 final='end.vasp'
32
33 # summary file name
34 neb_summary_str='summary_neb.txt'
35
36 # vasp parameters
37 calc1 = Vasp(prec = 'Accurate',
38        pp = 'pbe',
39        istart=0,
40        ismear=1,
41        sigma=0.1,
42        lcharg=False,
43        lwave=False,
44        lreal = 'Auto',
45        lorbit=0,
46        images=nimages,
47        lclimb=True,
48        spring=-5,
```

```
        encut = 450,
        algo='Normal',
        nelm=80,
        ediff=1e-6,
        ibrion=3,
        potim=0,
        iopt=1,
        nsw=150,
        nelmin=4,
        ediffg=-0.05,
        kpts = conv_kpt,
        gamma=True)

print("\n------------------------")
print("NEB calculation using ASE")
print("------------------------")

fl=open(neb_summary_str,'w')
fl.write('{:10s} {:12s} {:15s}\n'.format('Image', 'Energy (eV)','Barrier (eV)'))

cmd1=['nebmake.pl', initial, final, str(nimages)]
print('\n\n')

subprocess.call(cmd1)

copyfile(initial,'CONTCAR')
copyfile('outcar.start', 'OUTCAR')
```

```
76
77 fpath1 = path.join('00','OUTCAR')
78 copyfile('outcar.start',fpath1)
79
80 fpath2 = path.join('{:02d}'.format(nimages+1),'OUTCAR')
81 copyfile('outcar.end',fpath2)
82
83 dummy.set_calculator(calc1)
84 dummy.get_potential_energy()
85
86 for i in range(nimages+1):
87
88     outcar_path = path.join('{:02d}'.format(i), 'OUTCAR')
89     pot_en = read(outcar_path).get_potential_energy()
90
91     if i == 0:
92         pot_0 = pot_en
93
94     fl.write(' {:3d} {:15.4f} {:12.3f}\n'.format(i, pot_en, pot_en-pot_0))
95
96 calc1.clean()
97 fl.close()
98
99 print('---- NEB DONE ----')
```

In rare cases, an NEB calculation needs to be restarted. The following script automates the process of restarting an NEB calculation.

```
''' This script restarts nudged elastic band (NEB) calculation.

In case the NEB calculation is not converged,
this script restarts the calculation.

The ‘nimages‘ needs to be the same as the initial
NEB calculation.

Also creates some dummy files to avoid errors.
'''

from ase.calculators.vasp import Vasp
import ase.io.vasp as vp
from ase.io import *
import subprocess
from shutil import *
from os import path

# dummy structure of run vasp
dummy = vp.read_vasp('start.vasp')

# converged kpoints for the structure
conv_kpt=[2, 2, 1]

# number of images
nimages=6

```

```
# summary file name
neb_summary_str='summary_neb.txt'

# vasp parameters
calc1 = Vasp(prec = 'Accurate',
       pp = 'pbe',
       istart=0,
       ismear=1,
       sigma=0.01,
       lcharg=False,
       lwave=False,
       lreal = 'Auto',
       lorbit=0,
       images=nimages,
       lclimb=True,
       spring=-5,
       encut = 550,
       algo='Normal',
       nelm=80,
       ediff=1e-6,
       ibrion=3,
       potim=0,
       iopt=7,
       nsw=350,
       nelmin=4,
       ediffg=-0.01,
       kpts = conv_kpt,
```

```
55          gamma=True)
56
57  print("\n-------------------------")
58  print("NEB calculation using ASE")
59  print("-------------------------")
60
61  for i in range(1,nimages):
62
63      this_dir='{:02d}'.format(i)
64
65      contcar_str=path.join(this_dir, 'CONTCAR')
66      poscar_str=path.join(this_dir, 'POSCAR')
67
68      copyfile(contcar_str, poscar_str)
69      copyfile(contcar_str, 'contcar.{}'.format(i))
70
71
72  fl=open(neb_summary_str,'w')
73  fl.write('{:10s} {:12s} {:15s}\n'.format('Image', 'Energy (eV)','Barrier (eV)'))
74
75  fpath1 = path.join('00','OUTCAR')
76  copyfile('outcar.start',fpath1)
77
78  fpath2 = path.join('{:02d}'.format(nimages+1),'OUTCAR')
79  copyfile('outcar.end',fpath2)
80
81  vp.write_vasp('CONTCAR',dummy, vasp5=True)
```

```
copyfile('outcar.start', 'OUTCAR')

dummy.set_calculator(calc1)
dummy.get_potential_energy()


for i in range(nimages+1):

    outcar_path = path.join('{:02d}'.format(i), 'OUTCAR')
    pot_en = read(outcar_path).get_potential_energy()

    if i == 0:
        pot_0 = pot_en

    fl.write(' {:3d} {:15.4f} {:12.3f}\n'.format(i, pot_en, pot_en-pot_0))

calc1.clean()
fl.close()

print('---- NEB (restart) DONE ----')
```

B.3.5 Adsorption energy calculations

Adsorption energy calculations involve ground state energy calculation for initial and final state. The following script calculates adsorption energy of B in different adsorption sites of a Ni [111] surface. The ground state energy of each structure is tabulated in a summary file. This summary file can be read and used to calculate the adsorption energy.

Listing B.13: Adsorption energy of boron on Ni 111 surface.

```
''' This script does surface relaxation of B/N atom
on different sites of a metal 111 surface (i.e. Cu/Co/Ni)

This script puts an interstitial C atom on the octahedral site close to
the 111 surface then relaxes the B/N atom on different sites.

The ‘sup_size‘ variable defines the supercell size and the
‘z_layers‘ defines the number of layers. For example ‘sup_size‘
and ‘z_layers‘ as 4 and 4 denotes a surface supercell of
size 4x4x4.

‘int_dist‘ is the distance between the adsorotion atom
and the top of the surface.

‘int_c‘ is a boolean flag to define whether the interstitial
C atom will be there or not.

‘add_bn‘ defines the symbol of the adsorption atom.

‘run_flag‘ defines calculation for which site is to be run.

‘sites‘ list defines the adsorption sites of a 111 surface.

The final energies are tabulated in a file defined by
‘out_summary‘. Functions ‘check_convergence‘, ‘calc_binding_energy‘
and ‘get_distance‘ found in ‘utility_functions.py‘ can be used
```

```
27 to extract binding energy of the sites.
28
29 All the relaxed structure along with vasp.out and OUTCAR
30 files are copied into ‘data-dir‘ with file name
31 <site_name>.<file_name>
32
33 '''
34
35 from ase.build import fcc111,add_adsorbate
36 from ase import Atoms as at
37 import ase.io.vasp as vp
38 from ase.constraints import FixAtoms, FixedPlane, FixedLine
39 import numpy as np
40 from os import path, makedirs, rename, remove, getcwd
41 from ase.calculators.vasp import Vasp
42 from shutil import *
43 from os import path, remove, rename
44
45
46 # input: how many layers of the surface in the z direction?
47 sup_size=4
48 z_layers=4
49 relax_n_layers=2 # how many layers to fix
50 m_ind=0 # index of the adsorbate atom to set
51 int_dist=1.5
52 int_c=False
53 add_bn='B'
```

```
54 sp_a = 3.5204 # lattice constant in Angstrom
55 conv_kpt=[6, 6, 1]
56 run_flag=[1, 1, 1, 1]
57 sites=['ni-surf','fcc','hcp','ontop']
58 out_summary='bn_summary.txt'
59 data_dir='data'
60
61
62 print('\n-----------------------------------------------------')
63 print(' Calculation of interlayer distance for binding energy')
64 print(' Written by: Protik Das ')
65 print('-----------------------------------------------------\n\n')
66
67 print(' Sites {}'.format(sites))
68 print(' Run flag {}'.format(run_flag))
69
70 if not path.exists(data_dir):
71     makedirs(data_dir)
72
73 if not path.isfile(out_summary):
74     fl=open(out_summary,'w')
75     fl.write('{:10s} {:10s}\n'.format('Config', 'Energy (eV)'))
76 else:
77     fl=open(out_summary,'a')
78
79 bot_111 = fcc111('Ni', size=(sup_size,sup_size,z_layers), a=sp_a, vacuum=15.0) # create
      surface with a n X n X n supercell
```

```
80
81  bot_111.wrap()
82
83  cell = bot_111.get_cell()
84
85  for id,site in enumerate(sites):
86
87      if run_flag[id]==1:
88
89          print('\n\n Running for \'{}\' site.\n'.format(site))
90
91          calc = Vasp(prec = 'Accurate',
92              pp = 'pbe',
93              istart=0,
94              ismear=1,
95              sigma=0.05,
96              lcharg=False,
97              lwave=False,
98              lreal = 'Auto',
99              encut = 550,
100             algo='Normal',
101             ediff=1e-6,
102             ibrion=1,
103             nsw=350,
104             nelmin=4,
105             nelm=80,
106             ediffg=-0.01,
```

```
107         isif=2,
108         kpts = conv_kpt,
109         gamma=True)
110 
111     interface = bot_111.copy()
112 
113     if site != 'ni-surf' :
114         add_adsorbate(interface, add_bn, height=int_dist, position=site)
115 
116 
117     if int_c:
118         add_adsorbate(interface, 'C', -1.05, position='fcc')
119 
120     mask = [atom.tag > relax_n_layers for atom in interface]
121     fixlayers = FixAtoms(mask=mask)
122     interface.set_constraint(fixlayers)
123 
124     vp.write_vasp('temp1.vasp', interface, label='Ni (111) surface', direct=True, sort=
            True, vasp5=True)
125     in2 = vp.read_vasp('temp1.vasp')
126 
127     in2.set_calculator(calc)
128 
129     energ1 = in2.get_potential_energy()
130 
131     fpath1 = path.join(data_dir,'{}.vasp.out'.format(site))
132     fpath2 = path.join(data_dir, '{}.OUTCAR'.format(site))
```

```
133         fpath3 = path.join(data_dir, '{}.CONTCAR.vasp'.format(site))
134 
135         copyfile('vasp.out', fpath1)
136         rename('OUTCAR', fpath2)
137         rename('CONTCAR',fpath3)
138 
139         fl.write(' {:9} {:9.4f}\n'.format(site, energ1))
140         print(' {:9} {:9.2f}eV'.format(site,energ1))
141 
142         fl.flush()
143 
144         print('\n Finished running for {} site.'.format(site))
145 
146 fl.close()
147 
148 calc.clean()
149 
150 print(' done.')
```

Appendix C

LATTE lab infrastructure administration

LATTE lab has a state of the art compute server, which is named Excelso. The user data is stored in a file server named Calypso. Along with the user data, the file server also hosts cluster monitoring service ganglia and LDAP server that is used to manage user accounts.

C.1 Servers

C.1.1 Calypso

Calypso is the file server that hosts user data. The operating system of Calypso is FreeBSD which is in a 400 GB SSD. Externally url of calypso is `http://calypso.engr.ucr.edu/` and internal url is *calypso.lan*. The file system of Calypso is ZFS. Within this file system, the whole hard disk space is considered to be in a pool. The pool that stores all

data is named `data`. The ZFS file system pulls drive space as needed. The ZFS storage is configured by a tool named `zpool`. To check the status of `zpool`, the following command can be used.

```
# zpool status
```

For listing basic ZFS information the command `zfs list` can be used. In ZFS partitions are called data set. This command list all available data set with snapshots. A hidden directory name *.zfs* stores all the snapshots. The configuration file of ZFS screenshot is *zfs-snapshot-mgmt.conf* in directory `/usr/local/etc`. This configuration file can be used to configure the screenshots. To create a new partition with ZFS the following command can be used,

```
$ zfs create data/test
```

To delete an existing partion,

```
$ zfs destroy data/test
```

Checking of a ZFS file system for data integrity is called data scrubbing. The pool is needed to scrub once in a while which is done by doing,

```
$ zpool scrub <pool name>
```

There are two scripts named `zp_checkpool` and `zp_scrub_data` in the `cluster-scripts` directory. The first one checks if all the pools are healthy for each 6 hours through a cron-job. If not, it sends an email to admins. The second script *scrubs* the pool every Sunday at 12AM through another cronjob. Currently it's done once every week. The scrubbing process reduces the performance of zpool. Hence running it during a job which is doing heavy reading and writing may add additional delay for reading and writing operations

at the file server. For the redundancy at a lower level, the file system is configured with RAID-Z2 which doubles the parity structure to achieve results similar to RAID 6.

C.1.2 Excelso

The compute cluster of LATTE lab, Excelso is equipped with 12 worker nodes. Each of these worker nodes contains two AMD Opteron 6320 8-Core CPU processor on a Tyan S8230GM4NR EATX Opteron Server mainboard. Each processor has clock speed of 2.8GHz with L3 cache memory of 16 MB. These 12 nodes are connected together through a smart Gigabit switch with CAT-6 cables. Each worker node has its own 128GB Solid State Drive (SSD) storage for scratch space. The head node is equipped with the same AMD Opteron processor with 1TB of SSD with 4TB of HDD storage.

Excelso is mounted using a program named `autofs`. It is used for automatically mounting directories on an as-needed basis. Auto-mounts are mounted only as they are accessed, and are unmounted after a period of inactivity. The program `automount` is used to configure a mount point for `autofs`. When `autofs` is started, an `automount` daemon is spawned for each map. Auto-mount or auto-mounting refers to the process of automatically mounting filesystems. `autofs` is the program which controls the operation of the `automount` daemons. The file `auto.master` at `/etc` is the master configuration file for *autofs*. Also the files `auto.home` and `auto.software` contains configurations for mounting respectively the home directory and the softwares directory.

The `softwares` directory contains the necessary softwares are located. For example, the directory `/clusters/armadillo` contains Armadillo C++ linear algebra library. The `IDEs` folder contains *netbeans* IDE. The folder boost contains *boost* v1.53 which is a

collection of libraries. It also has several libraries for MPI and mathematics like mkl and acml. Also `amd` folder contains `open 64` which is a compiler system for high performance, production quality code generation tool designed for high performance parallel computing workloads in servers that has AMD processors.

The directory `cluster-scripts` contains customized scripts. These scripts can be used for various administrative purposes. For example, `nodesup` can be used to get a list of working nodes, `nodesdown` for the opposite, `nreboot` for rebooting the nodes, `nshutdown` for shutting down all the nodes, `ncp` for copying file to all nodes.

C.2 Services

C.2.1 Ganglia

Ganglia (`http://ganglia.info/`) is the monitoring tool used for the clusters. It has three components: web, `gmetad` & `gmond`. The `gmetad` service is on *Calypso* that waits for information to be sent to it from the nodes. The `gmond` service is in head node of Excelso. It collects information running on all of the nodes along with the head node itself. The configuration file for `gmetad.conf` is located in `/usr/local/etc/gmetad.conf` directory of Calypso. Also configuration file for nodes is in `/etc/ganglia/gmond.conf`. In order to restart Ganglia *gmond* service on head nodes must be restarted first using the following command

```
1 $ service gmond restart
```

Then each nodes of Excelso using the script `nrestartGanglia`.

C.2.2 SLURM

Slurm (`https://computing.llnl.gov/linux/slurm/`) is the utility used in Excelso for job processing and control. Slurm restricts access to the compute nodes to only those users who have a job allocated to that node. This is controlled by a pam module called *pam_slurm.so* and is used in `/etc/pam.d/system-auth` on the compute nodes.

General Maintenance

The most common tasks for administering slurm are "draining" a node so that maintenance may be performed on it. This usually means changing a node's state to `DOWN`. To "drain" a node, an utility named `scontrol` is used. For unresponsive nodes, the command `nodesup` can be used to the node is up or not. Then the command below configurations accessible for each node to the slurm service.

```
$ scontrol show nodes
```

Most important thing of the output is the state. The states may be `IDLE/allocated/mixed/down/`
If there is any error, debugging can be started from here. After troubleshooting the state of the node, the state of the node needs to be updated manually. It can be done by:

```
$ scontrol update node=e4 state=IDLE
```

If the above command doesn't work, the slurm service in all nodes need to be restarted. To restart slurm in slave nodes the script `nrestartSlurm` can be used. For restarting slurm in the head node, the following command can be used.

```
$ service slurm restart
```

To see a listing of currently running jobs, command `squeue` can be used, To see slurm queue for a particular user, `squeue -u username` is used, to cancel a job `scancel JOBID` can be used. To know detail about running jobs or a particular job not behaving properly, `scontrol show jobs` is useful. To debug slurm, `slurm.conf` file at `/etc/slurm` at Excelso can be updated. Editing `slurmdDebug` line in the configuration file increases verbosity of the slurm log. For example, `slurmdDebug = 2` ouputs more information to the log file. The slurm configuration file needs to be same in all worker nodes along with the head node. After any modification, the configuration file can be copied to all worker nodes by,

```
$ ncp /etc/slurm/slurm.conf /etc/slurm/slurm.conf
```

After copying the configuration files, the slurm service needs to be restarted.

```
$ service slurm restart
```

To cancel bulk jobs, for example, to cancel all jobs by any particular user with particular state (RUNNING/PENDING) the following command is used.

```
$ scancel --state=<state> --user=<username>
```

C.3 Maintenance

C.4 User Accounts

User accounts are managed by an Lightweight Directory Access Protocol (LDAP) server using OpenLDAP (`http://www.openldap.org/`). It is managed via a web interface provided by LDAP Account Manager (LAM, `http://www.ldap-account-manager.org/`).

This interface may be accessed via `https://calypso.engr.ucr.edu/lam/`. Configuration files for LDAP is located at `/usr/local/etc/openldap /ldap.conf` in Calypso.

C.4.1 Adding a user account

For a new user, an user account needs to be created. The first step is to login into the LAM webpage. The security exception warning can be ignored. As the SSL certificate is generated locally, hence the warning. To add a new user, click on `New user`. On the Personal tab put First name and Last name. Then in the Unix tab put new user in "latte" primary group. And then to allow him to do ssh, click on edit groups and add him to "sshAllowed" group. For a new system administrator, add him to "wheel" group. Then click on the `Set password` button. Allow him to provide his password and new users part is done.

After creating a user, some files are needed to be put into users account manually. For this, log into calypso as root. Some common cluster files are located at: `/usr/local/cluster-scripts/`. Run the script `createHomeDir` followed by the username. It will copy all the necessary files & set the Home directory quota. Example of running the script is:

```
$ ./createHomeDir username
```

C.4.2 Editing a User Account

Editing a user is similar to creating a new one, except that the account already exists. After logging into the LAM webpage, click the edit icon (icon with sheet of paper with a pencil) next to their account on the users account page. Then make the changes

required and save the account.

C.4.3 Deleting a User Account

Deleting an account is usually a bad idea. If one must, simply delete icon next to the user's account can be used. A better idea, however, is to simply lock the account. This may be done in two ways: disallow SSH access and lock the password. Disallowing SSH access is done by removing the user from the `sshAllowed` group). To lock the password, edit the user account and click the "Lock password" button. Re-enabling a user's account is as simple as re-adding them to the *sshAllowed* group, or unlocking their password if the password was locked.

C.5 Website Administration

The LATTE webpage is hosted on server Supremo. The webpage is managed by a wordpress installation.

C.5.1 CMS Administration

The CMS for the website is wordpress. The theme used for the website is named *Graphene*. Themes and plugins all are customized for better performance.

C.5.2 Backup before Updating CMS

A copy should be made before updating wordpress. Copying the latte folder of *www* folder inside apache installation will do.

C.5.3 Server Administration

The web server is hosted at Supremo. It's boot partition are four way mirrored. All of them have mirrors. So if three of them are down, still it can be booted without loosing any information. Root also have four hard drives. Each hard drive have it's own root partition. Each partition has `root`, `boot` and `swap`. Each `boot` and `root` are mirrored and each has `swap` partitons. The file systems table configuration file is located at `/etc/fstab`. The webserver is run by FreeBSD operating system. The Apache and MySQL server are running inside two separate jails. Even root access into a particular jail cannot give access to the core operating system. It only gives access to allowed partition. The server has its own firewall (pf) as well. Jail named `LATTEWEB` runs the `apache` server and the jail `LATTEDATABASE` runs the `mysql` database. There are some other jails which can be used for development purpose. To see a list of running jails use `ezjail-admin list` can be used. The command `ezjail-admin` is the tool used for jail administration. These jails physically resides in `/usr/jails` directory. For logging in to any jail the following command can be used.

```
1 $ ezjail-admin console jailname
```

Server configuration file for apache is named `httpd.conf` which is located at `/usr/local/etc/`. For testing purpose virtual host can be configured. Virtual host can be configured from `/usr/local/etc/apache22/extra/httpd.vhost.conf`. Also the word-press configuration file `wp-config.php` is in directory `/srv/http/latte`. For new users a jail can be made. To access database for the site, `ezjail-admin console LATTEDATABASE` can be used. The `mysql` installation accepts connection only from the jail system. To access

`mysql` `mysql -u root -p` can be used.

Backing up Jails

The jails should be backed up time to time. Previous backups are in the directory `/backup/jails`. This is the default directory for backup. For backing up a jail, first the jail is needs to be stopped. It can be done using the following command,

```
$ ezjail-admin stop LATTEWEB/LATTEDATABASE
```

Then the command below archives the jail.

```
$ ezjail-admin archive LATTEWEB/LATTEDATABASE
```

After archiving, a jail can be started using,

```
$ ezjail-admin start LATTEWEB/LATTEDATABASE
```

An archived jail can be restored using the following command,

```
$ ezjail-admin restore LATTEWEB/LATTEDATABASE
```